University of Stavanger

FACULTY OF SCIENCE AND TECHNOLOGY

MASTER THESIS

Study programme/specialisation: Petroleum Geosciences Engineering	Spring semester, 2020 Open
Author: Adrian Pindel	…… (signature of author)
Programme coordinator: Nestor Cardozo Supervisor(s): Nestor Cardozo, University of Stavanger Lothar Schulte, Schlumberger SIS	
Title of Master thesis: Comparison of facies models based on stochastic versus deterministic AVO inversion	
Credits: 30	
Keywords: Stochastic AVO inversion Deterministic AVO inversion Sandstone volume Facies modeling Oseberg Sør	Number of pages: 87 Stavanger, June 15, 2020

Comparison of facies models based on stochastic versus deterministic AVO inversion

by

Adrian Pindel

MSc Thesis

Presented to the Faculty of Science and Technology

The University of Stavanger

The University of Stavanger

June 2020

Acknowledgements

This Master thesis is submitted in completion of the MSc in Petroleum Geosciences Engineering at the University of Stavanger.

I would like to thank my supervisors Lothar Schulte and Nestor Cardozo for the best possible guidance throughout this thesis and for their constant positive attitude.

I would like to thank Equinor ASA and the Oseberg Sør license for providing the dataset and Schlumberger for providing an academic license of the Petrel software.

Disclaimer

The views expressed in this paper are the views of the author and do not necessarily reflect the views of Equinor and the Oseberg Sør license.

Comparison of facies models based on stochastic versus deterministic AVO inversion

Adrian Pindel

The University of Stavanger, 2020

Supervisors: Nestor Cardozo, Lothar Schulte

Abstract

This thesis compares facies models based on deterministic AVO inversion – which is a standard approach in the industry, and stochastic AVO inversion – which is a newer, less popular approach, but according to literature, better for volumetric calculations. The thesis aims to understand the value of stochastic AVO inversion for facies modeling and showcase its superiority over deterministic AVO inversion. These two methods can lead to substantial differences in the estimated Gross Rock Volume of sandstone in a reservoir, which is critical for calculating hydrocarbon reserves.

The study is applied to a dataset provided by Equinor ASA, covering the J-structure of the Oseberg Sør field in the northern North Sea. The reservoir is the Middle Jurassic Brent Group at an approximate depth of 2200-2800 m and consisting of sandstone, shale, and limestone. These are the main lithofacies modeled in the thesis.

The deterministic AVO inversion allows to retrieve elastic properties such as P-impedance and Vp/Vs ratio from the seismic angle stacks. The vertical resolution of the deterministic AVO inversion is limited by the seismic bandwidth, therefore its result is smooth. The stochastic AVO inversion, on the other hand, uses the variogram model to simulate the thin layers below seismic resolution and allows catching the uncertainty of the inverse problem by generating multiple equiprobable realizations of the elastic parameters.

The Bayesian classification algorithm is applied to the well log data to obtain the litho-classification model, which is used to derive sandstone, shale, and carbonate probabilities from the deterministic AVO inversion. Then, facies probabilities are used to guide the sequential indicator simulation (SIS) to get many equiprobable facies models. The deterministic AVO inversion and the well logs are used to obtain the variogram model needed for the stochastic AVO inversion. The litho-classification model is directly applied to multiple realizations of the stochastic AVO inversion to obtain facies models.

The workflow based on the stochastic AVO inversion results in less sandstone in the reservoir Brent-Drake zone than the workflow based on the deterministic AVO inversion. However, the stochastic AVO inversion workflow with a smaller lateral variogram range shifts the sandstone volume towards the results of the deterministic AVO inversion. A lower lateral variogram range introduces a larger variability in the sandstone probability which delivers a similar effect to SIS. Consequently, the lateral variogram range is of critical importance for facies modeling using stochastic AVO inversion, though it has a small impact on the P50 volume obtained from the

deterministic AVO inversion. A decrease of the variogram range decreases the spread of the volume distribution for both types of facies modeling.

Since both workflows can be parametrized to deliver similar results by changing a highly uncertain lateral variogram range, the value of the stochastic AVO inversion for facies modeling is not yet fully understood and requires further research.

Table of Contents

List of tables

List of figures

1. Introduction

1.1. Geomodel conditioning using seismic data

The conditioning of the reservoir model to high-quality 3D seismic data is a data-driven approach to the geological model design (Ringrose and Bentley, 2015). Conditioning utilizes the fact that seismic amplitudes contain information about the geological properties of the reservoir (Russell, 2016). Seismic inversion aims to retrieve the elastic properties of the geological layers contained in the seismic amplitudes. Elastic properties such as acoustic impedance, P-wave to S-wave velocity ratio, or density can be linked to reservoir properties such as facies, porosity and saturation using rock physics analysis. Incorporating seismic data into the modeling workflow is an alternative to the modeling based only on well data. The seismic-driven approach can potentially lead to a gain of information about reservoir properties between the well data such as porosity and permeability distribution, hydrocarbon volume or connectivity (Russel, 2016), and thus it can result in better decision making.

Soft conditioning is an approach where information from seismic data can be used as a guide for probabilistic algorithms used in geomodelling (Ringrose and Bentley, 2015). The model from Figure 1-1 presents this approach. The Vp/Vs ratio retrieved from seismic data via seismic AVO inversion is resampled into the model cells (left-hand side image) and used to guide facies distribution (right-hand side image: facies model). High Vp/Vs ratio is attributed to shales, while lower Vp/Vs ratio is attributed to sandstones. A rock physics study was incorporated as the basis of this correlation.

There are two general types of inversion, deterministic and stochastic. Deterministic inversion results in a unique optimal and smoothed solution of the elastic properties due to the band-limitation of the seismic data, whereas stochastic inversion generates multiple realizations of the elastic parameters, all honoring the seismic data and allowing capturing the uncertainty related to the inversion process (Simm and Bacon, 2014). Inversion methods can be divided into post-stack and pre-stack methods. Post-stack methods invert full-stack seismic data, resulting in acoustic P-impedance. Pre-stack inversion, also called AVO inversion, uses multiple angle stacks to obtain P-impedance, shear-impedance, Vp/Vs ratio, density, and other elastic parameters (Doyen, 2007). It is based on the fact that the seismic amplitude depends on the reflection angle and the elastic properties of the reflector (Buland and Omre, 2003).

The focus of this thesis is to understand the gain in information and predictability when using stochastic AVO inversion in the modeling of the main facies, here understood as the main lithologies, constituting the reservoir.

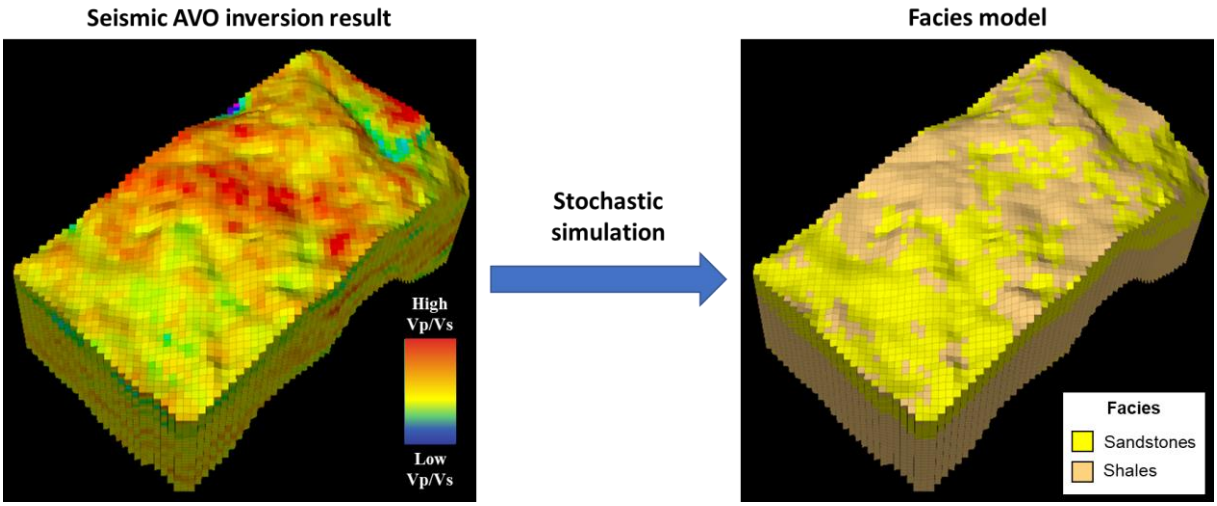

Figure 1-1. The concept of soft conditioning of a reservoir model using seismic data. Left-hand side image: Vp/Vs ratio obtained from seismic AVO inversion resampled into the model cells. Right-hand side image: facies model guided by Vp/Vs ratio. The high Vp/Vs ratio (red) is attributed to shales and lower Vp/Vs ratio (yellow, green) is attributed to sandstones

1.2. Study objectives and motivations

This thesis aims to compare the value of facies modeling guided by deterministic versus stochastic AVO inversion. Incorporating AVO inversion into the modeling workflow is supposed to give a better delineation of the facies and therefore a more precise estimation of the Gross Rock Volume, which is one of the most important parameters when calculating hydrocarbon reserves. In comparison to the deterministic AVO inversion, the stochastic AVO inversion captures the uncertainty in the facies volumes estimations and potentially better characterizes thin, sub-seismic layers due to the incorporation of information from well logs into the inversion while honoring the seismic data. The goal of this thesis is to provide a reliable estimation of the sandstone volume of the studied reservoir and showcase the superiority of stochastic AVO inversion over the deterministic AVO inversion in guiding facies models. In addition, the thesis provides a comprehensive workflow for stochastic AVO inversion and its application to facies simulation and facies uncertainty estimation.

1.3. Study area

This study addresses the Middle Jurassic Brent Group reservoir level of the J-structure in the Oseberg Sør field, North Sea. The reservoir zone lies approximately between 2200 to 2800 m

depth. The field is located on the eastern flank of the Viking Graben in the northern North Sea. The location of the field is shown in Figure 1-2.

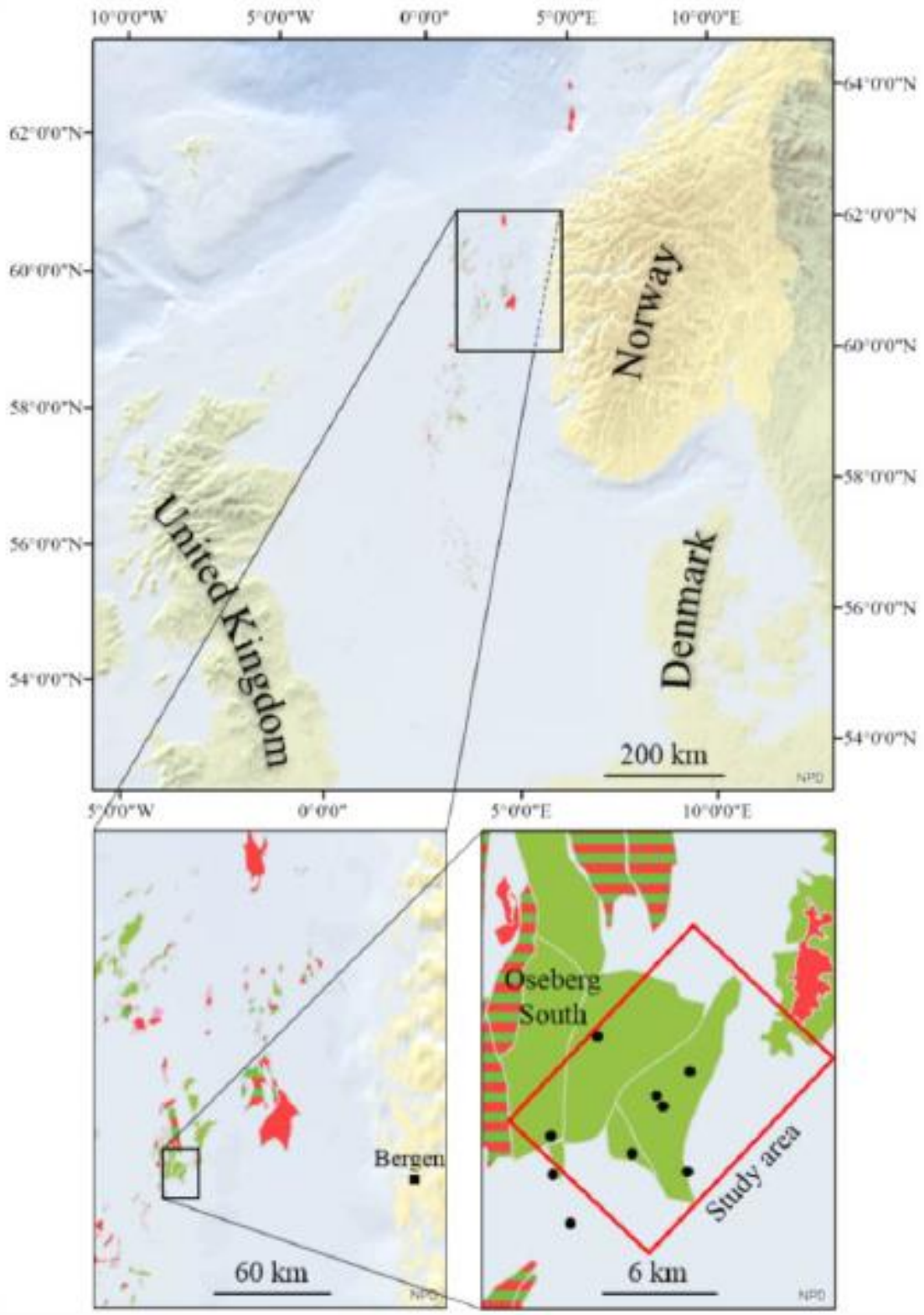

Figure 1-2. Location of the Oseberg Sør field. Study area (red square), available wells (black dots) and nearby fields (oil fields are in green and gas fields are in red). From Frette (2018)

1.4. Previous work

Published work related to the modeling and the seismic inversion of the Oseberg Sør field includes three master theses at the University of Stavanger: Rotar (2019), Tayyaba (2018), and Frette (2018).

Rotar (2019) compared the results of poststack deterministic and stochastic seismic inversion for facies modeling of the reservoir unit of the Oseberg Sør field J-structure. He used acoustic impedance values from well logs to differentiate between carbonates and siliciclastic facies, constructed a geological model for the reservoir zone, and populated it with facies predicted from the inverted acoustic impedance cube. He concluded that the poststack stochastic inversion is superior to the deterministic inversion since it captures the uncertainties of estimated elastic parameters and provides better delineation of thin, sub-seismic layers. In the case of thick (relatively to seismic resolution) layers, the poststack stochastic inversion superiority is related to capturing the non-uniqueness of the inverse problem.

Tayyaba (2018) performed joint PP and PS deterministic AVO inversion, and derived seismic lithology maps for the reservoir zone in the Oseberg Sør field. She concluded that the joint AVO inversion of compressional PP and converted PS waves leads to a more precise estimation of elastic parameters than the AVO inversion of PP waves alone. The lithology maps derived in this work give a probabilistic estimation of encountering certain facies in the reservoir zone.

Frette (2018) performed deterministic joint PP and PS AVO inversion to study the value of using converted waves in the seismic interpretation of the Oseberg Sør field. He derived rock physics cross-plots to differentiate between facies and suggested the use of acoustic impedance to predict facies distributions.

No published works incorporate stochastic and deterministic AVO inversions into the facies modeling workflow of the Oseberg Sør field. This thesis uses stochastic AVO inversion for the first time in the Oseberg Sør field, which potentially can lead to a better estimation of the sandstone volume and showcase the superiority of stochastic over deterministic AVO inversion in guiding facies models. There are however studies from other fields discussing the results from stochastic and deterministic seismic AVO inversions.

Francis (2006b) calculated the volumes of shale and high-impedance sandstone for the Stratton field, USA, using deterministic and stochastic poststack seismic inversion for acoustic impedance. He concluded that the deterministic poststack inversion leads to a significant underestimation of sand volume, and because of its smoothness, it is generally unsuited for constraining reservoir models used for volumetric calculations. The deterministic poststack inversion might be suitable for modeling of a reservoir comprised of relatively thick layers in comparison to seismic resolution. Multiple realizations from a stochastic poststack inversion allowed a more accurate estimation of the reservoir volume and its uncertainty.

Russel (2016) showcased the use of deterministic and stochastic AVO inversion to estimate the sandstone volume for a channel sand play from West Africa. He discriminated sandstones from shales using Vp/Vs ratio cutoffs. The sandstone volume distribution resulting from his stochastic AVO inversion was much higher than the volume estimated using the deterministic AVO inversion as shown in Figure 1-3.

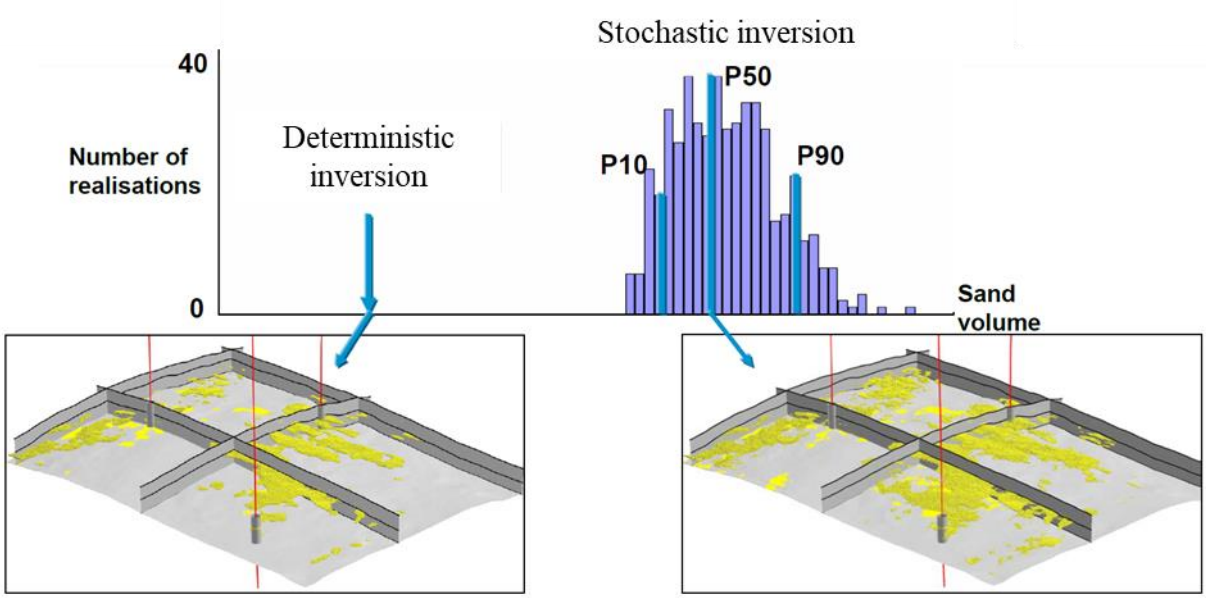

Figure 1-3. Sandstone volumes estimated using deterministic and stochastic AVO inversion. The histograms of sand volume (upper picture) show large differences in the outcome of the two methods. The deterministic AVO inversion produces one best estimate volume, whereas the stochastic AVO inversion produces a suite of equiprobable volumes. The sandstone volume obtained with the deterministic AVO inversion is underestimated. The lower part of the picture shows the sandstone volume from the deterministic AVO inversion (left-hand side) and the volume from one realization of the stochastic AVO inversion (right-hand side). Visual inspection allows evaluating which sandstone geobodies are connected to wells or with each other. Modified from Russel (2016)

Sams et al. (2011) conducted a facies modeling study on a field in the Nam Con Son Basin in Vietnam using stochastic AVO inversion. Sandstones and shales in this field have similar P-impedance values but differentiation between them was possible using the Vp/Vs ratio. These

authors emphasize that there must be a good separation between facies in the elastic domain to be able to perform proper seismic conditioning of the reservoir.

2. Geology of the area

The Oseberg-Brage area is on the western margin of the Horda platform and the eastern flank of the Viking Graben. The Horda platform is an area of significant hydrocarbon accumulations including the giant Oseberg and Troll fields and several smaller fields such as Brage and Oseberg Sør (Johnsen et al., 1995; Løseth et al., 2009; Ravnås and Bondevik, 1997).

The Viking Graben and adjacent platforms evolved as a result of at least two episodes of rifting during the Permian-Triassic and the Middle Jurassic to earliest Cretaceous. The second phase of rifting formed the present-day fault block structures separating the moderately faulted Horda platform to the east from the deeply subsided graben axis to the west. The main structural elements consist of N-S and NE-SW trending normal faults as shown in Figure 2-1 (Løseth et al., 2009; Ravnås and Bondevik, 1997).

According to Faerseth and Ravnås (1998), the Permo-Triassic graben axis is situated below the western part of the Horda Platform and is now the footwall of the Jurassic Viking Graben as shown in Figure 2-2a. The Oseberg block decoupled from the Horda Platform along the Brage fault during the main rift stage in the Middle Jurassic.

The lithostratigraphic chart of the area is shown in Figure 2-3. The Permo-Triassic syn-rift sequence in the Oseberg field was deposited on top of the metamorphic basement. Triassic interbedded sandstones, claystones and shales of the Hegre Group are overlain by massive, clean sandstones of the Upper Triassic to Early Jurassic Statfjord Group. The Early to Middle Jurassic Dunlin Group composed of siltstones, claystones, shales and sandstones is present above, followed by the Middle Jurassic Brent Group (Husmo et al., 2002; NPD, 2020a).

The Brent Group contains substantial hydrocarbon reserves and is subdivided into the Broom, Rannoch, Etive, Ness and Tarbert formations along with the Oseberg Formation, which is equivalent to the Broom Formation in the Oseberg field area (Fig. 2.3, Norwegian quadrants 30 and 31). The thickness of the Brent Group on and around the Horda Platform ranges from 78 to 159 m. The Brent Group consists of sandstones, siltstones, shales, and conglomerates deposited in a deltaic setting and is also commonly defined as the top of the pre-rift sequence (NPD, 2020c; Faerseth and Ravnas, 1998; Loseth et al., 2009).

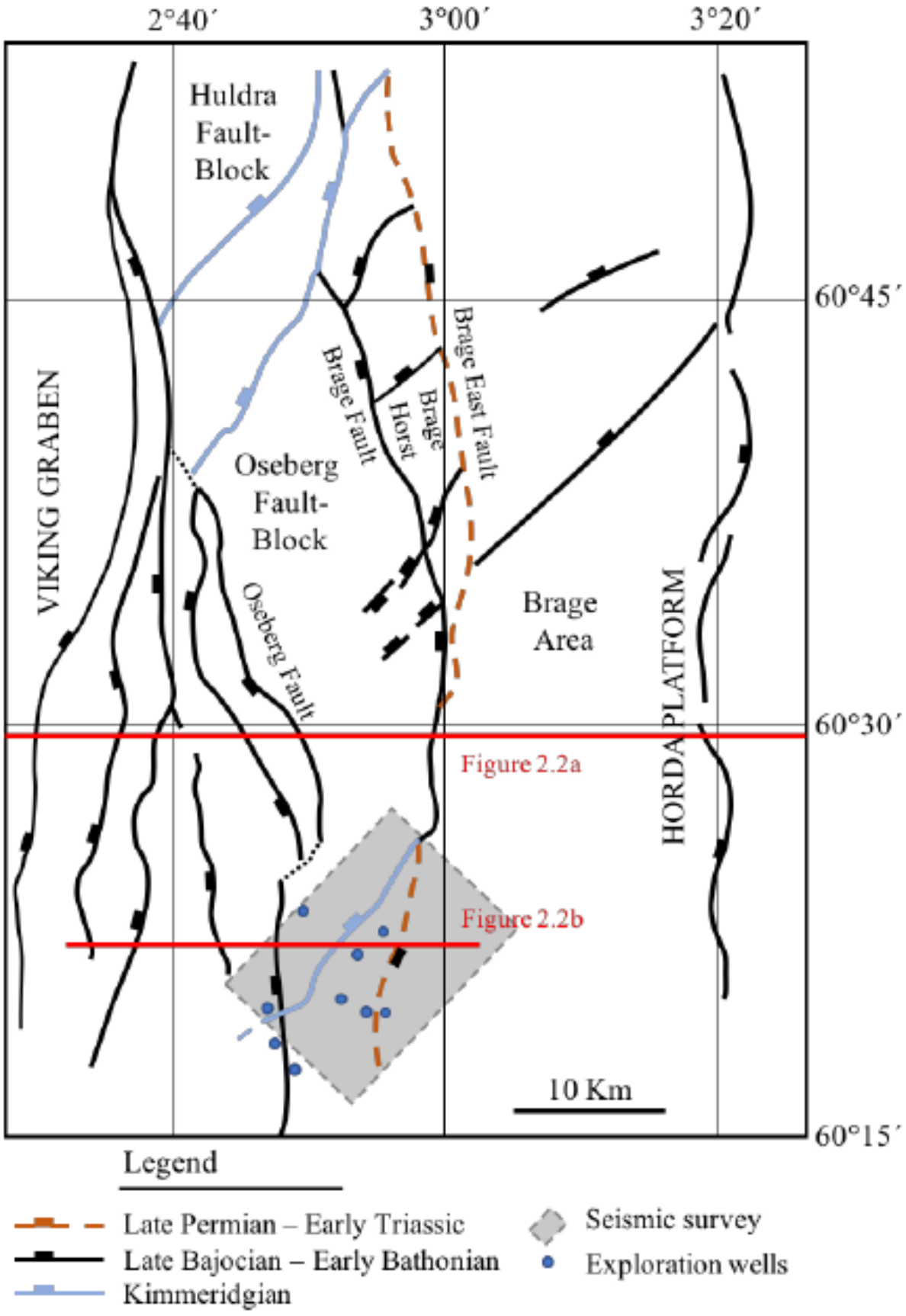

Figure 2-1. Structural map of the Oseberg-Brage area. The study zone is indicated by the gray rectangle along with the wells. From Frette (2018. Modified after Ravnås and Bondevik, 1997; Færseth and Ravnås, 1998).

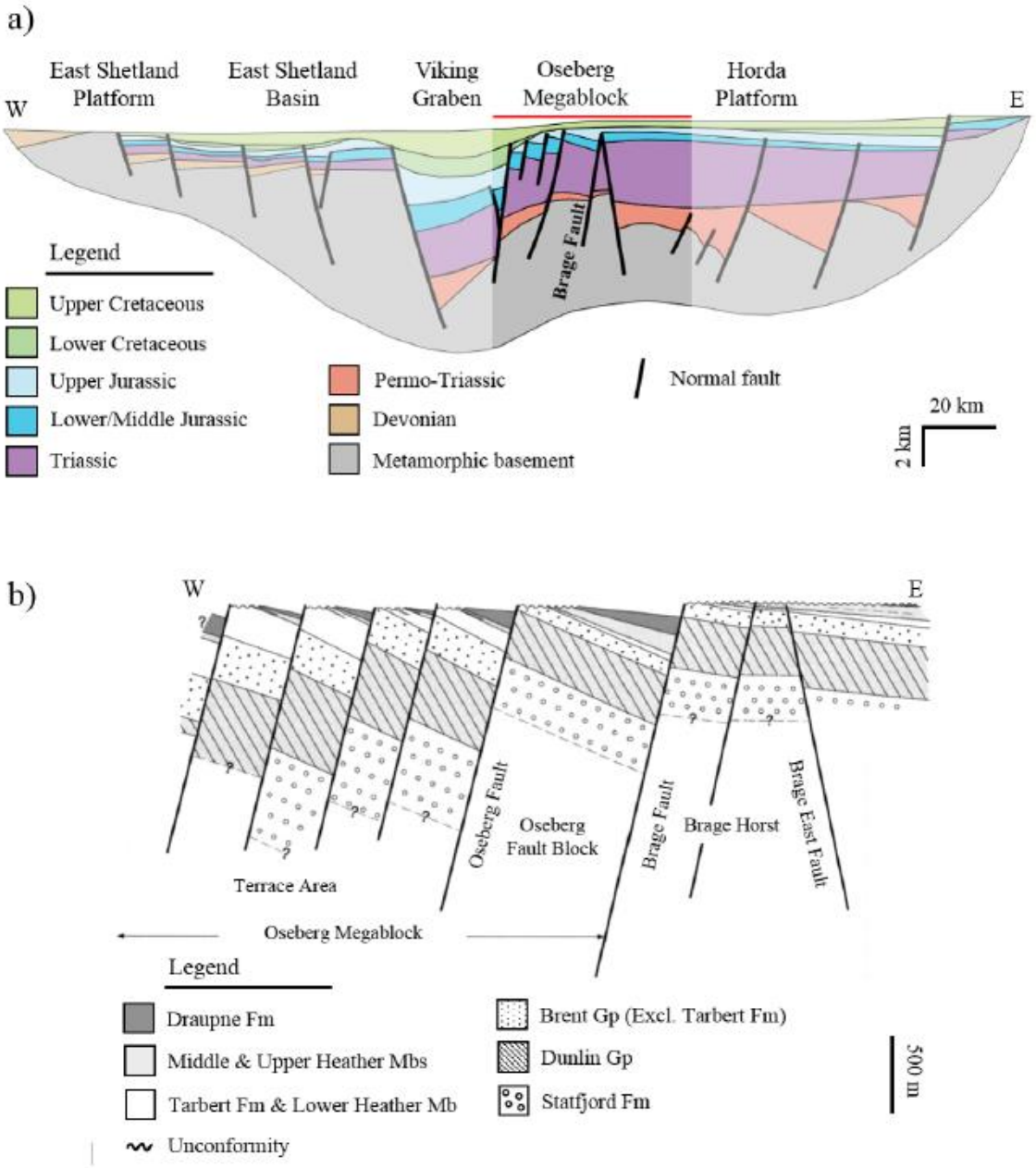

Figure 2-2. a) Cross-section showing Jurassic and Permo-Triassic major fault-blocks with related faults across the central segment of the northern North Sea at the end of the Cretaceous (Frette, 2018 after Færseth, 1996). The red line (and the area beneath it) represents the study area within the structural map in Figure 2-1. The axis of the older Permo-Triassic rift is shifted eastwards relative to the younger Jurassic Viking Graben b) Schematic cross-section showing the strata deposited during the Jurassic. The Brage horst forms the J-structure of the Oseberg Sør field (Frette, 2018 after Færseth and Ravnås, 1998). See Figure 2-1 for the location of the cross-sections

The Brent Group is overlain by marine mudstones, shales, and sandstones of the Middle Jurassic to Lower Cretaceous Viking Group followed by the post-rift predominantly mudstone sequence of the Cretaceous Cromer Knoll Group. The Shetland Group above consist of limestones, marls, shales, and mudstones deposited in an open marine environment (Fig. 2.3; NPD, 2020c).

The Oseberg Sør field is located just south of the Oseberg field. The main reservoir units are in the Tarbert and Heather formations, but hydrocarbons are also found in the Cook and Ness formations (Fig. 2.3). The reservoir lies at an approximate depth of 2200-2800 m (NPD, 2020b). The J-structure of the Oseberg Sør field, which is the subject of this thesis, is a horst bounded by the Brage and Brage East faults. A cross-section through the structure is shown in Figure 2-2b.

High amplitudes and irregular seismic anomalies in Oligocene strata (Fig. 2.3) can be identified in the Oseberg area. These anomalies are recognized as carbonate-cemented sand injectites. Due to their abnormally high seismic velocity and reflection coefficients, sand injectites cause a variety of problems for seismic imaging and the amplitude analysis of the reservoir below. Consequently, the area below the injectites shows a lower S/N (Signal/Noise ratio) which increases the uncertainty of the seismic amplitude analysis (Frette, 2018).

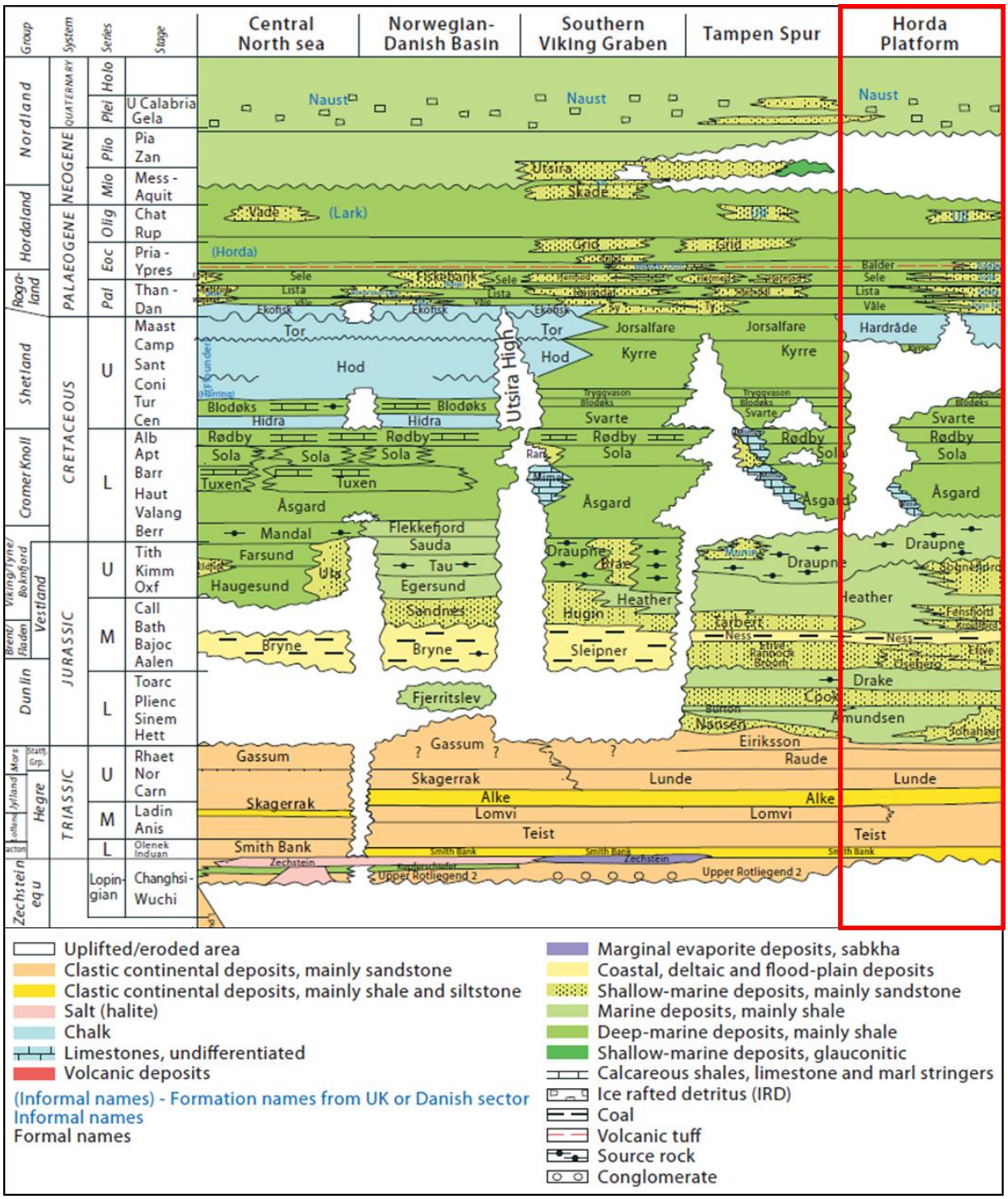

Figure 2-3. The lithostratigraphic column from the northern North Sea. The stratigraphy of the study region is highlighted by the red box. Modified from NPD (2014)

3. Theory

3.1. Rock physics for facies prediction

Understanding seismic-to-rock-property relations is the focus of the rock physics study. The elastic properties of an isotropic medium can be described using three types of information: P-wave velocity (Vp), S-wave velocity (Vs), and density. These parameters can be measured in the laboratory on a core, obtained using well logging or seismic AVO inversion. One of the most powerful uses of rock physics is the extrapolation of the information gained at the well location into the seismic volume. Rock physics analysis allows understanding how changes in lithology, porosity, or fluid saturation, especially away from the well, impact the seismic data (Avseth et al., 2005; Buland, 2019).

Vp, Vs, and density completely define the seismic wave propagation and reflection amplitudes in an isotropic linear elastic medium. The combination of these parameters results in rock moduli, e.g. the Lamé elastic constants, Young, bulk, and shear modulus. The rock physics study for a facies modeling workflow often starts with cross-plotting the different elastic properties derived from well data to separate facies clusters. These clusters, defined by characteristic sedimentological and rock physics properties, are referred to as seismic lithofacies (Avseth et al., 2005; Buland, 2019).

Acoustic impedance (abbreviated as AI or AIMP) is the product of P-wave velocity and density. It can be used to distinguish between lithofacies if their P-impedances do not overlap significantly. Francis (2006b) discriminated sandstones from shales using a simple cutoff after analyzing the histograms of acoustic impedance as shown in Figure 3-1.

The use of the Vp/Vs ratio allows differentiating between facies when they have similar acoustic P-impedance but different S-impedance. An example based on log data is shown in Figure 3-2 (Sams et al., 2011). Higher Vp/Vs ratio in shales than sands is expected since the shear strength in shales is relatively low due to the platy shape of clay particles (Avseth et al., 2005). Table 3-1 summarizes the ranges of selected rock physics parameters for common lithologies.

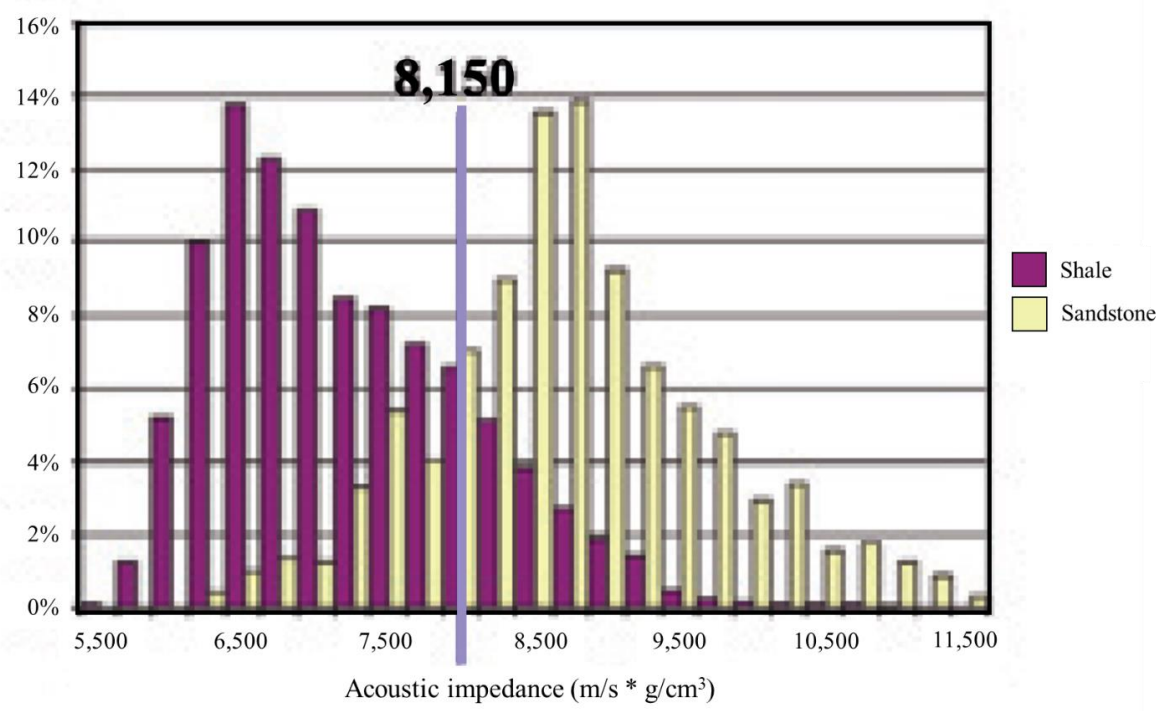

Figure 3-1. Histograms of acoustic impedance for sandstones and shales in the Stratton field with simple impedance cutoff to identify sandstones. The facies overlap for moderate acoustic impedance values, hence lithological classification using this cutoff predictor is biased. Modified from Francis (2006b)

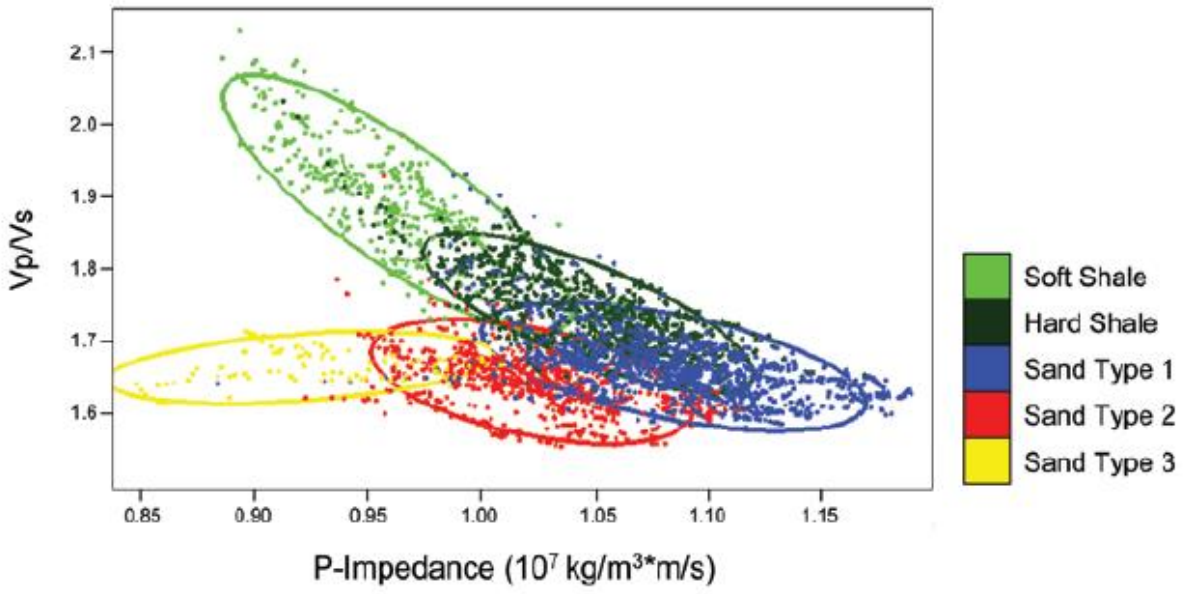

Figure 3-2. Crossplot of elastic properties color-coded by facies. Sandstones and shales have overlapping acoustic impedance but they can be distinguished using the Vp/Vs ratio (Sams et al., 2011)

Table 3-1. Compilation of selected rock physics parameters values for some common lithologies based on Ellis and Singer (2007), Jarzyna et al. (1999), Rider (2006), and Serra (1984).

	Acoustic impedance [kPa*s/m]	Vp/Vs ratio	Density [kg/m^3]
Sandstone	5700 – 16000	1.51 – 1.92	1900 – 2650
Limestone	8600 – 19000	1.84 – 1.95	2200 – 2700
Dolomite	10500 – 23000	1.76 – 2.00	2300 – 2870
Shale	3200 – 16000	1.61 – 1.93	1800 – 2750

3.2. Wavelet extraction

The wavelet is a seismic signal of limited, short duration. It is convolved with the reflectivity from the inversion results to obtain a synthetic seismic trace that is checked against the measured seismic. Simm and Bacon (2014) emphasize the importance of the wavelet for the inversion. In AVO inversion, a wavelet is needed for each angle stack. The wavelet is extracted from the seismic data using the reflectivity information from the well logs. It is recommended to use the deterministic extraction method for seismic inversion purposes as it correctly estimates the amplitude and the phase spectrum of the wavelet, so the synthetic seismic is properly scaled to the measured seismic. The wavelet predictability is derived from the cross correlation between the reflectivity and the seismic trace used for the wavelet extraction. This parameter allows to select the best wavelet derived from traces in the vicinity of the well (Schlumberger, 2019; Simm and Bacon, 2014).

The so-called ISIS frequency wavelet is the recommended type of wavelet for seismic AVO inversion. This wavelet extraction method minimizes the misfit between the seismic trace and the synthetic trace obtained as a convolution of the well log reflectivity and the wavelet. The optimum wavelet length is found by minimizing the Akaike's final prediction error for a suite of lengths and initial delays. The resulting wavelet models the highest possible amount of coherent signal (Schlumberger, 2019).

3.3. Seismic inversion

Seismic inversion can be defined as finding the cause of a seismic observation. There are different types of seismic inversion methods such as travel time tomography utilizing ray

tracing or full waveform inversion where the information about amplitudes, phase, and attenuation is incorporated (Jones, 2018). A broad group of methods is based on an amplitude inversion, which requires true amplitude processed data, where the amplitudes represent the subsurface reflection coefficients migrated to their correct positions (Buland, 2019). The following paragraphs describe the amplitude inversion.

Conventional seismic inversion is often referred to as deterministic or best estimate inversion. Typically, it results in a relatively smooth solution within the limits imposed by the bandwidth of the seismic data. In areas where the geology is layered on a scale below seismic resolution, the deterministic seismic inversion is generally unsuited for constraining geomodels for volumetric calculation or connectivity estimation. The stochastic or geostatistical seismic inversion generates multiple solutions (realizations) at the reservoir model scale. Each realization honors the seismic data. The set of realizations allows capturing the uncertainty or non-uniqueness of the seismic inversion process. The deterministic seismic inversion solution is the average of all possible realizations of the stochastic seismic inversion (Francis, 2006a; Simm and Bacon, 2014).

3.3.1. Deterministic AVO inversion

The seismic power spectrum is bandlimited, i.e. seismic data lacks both low and high frequencies. This imposes limitations to the seismic inversion process because the seismic data do not contain enough information to find the true model parameters. The lack of high frequencies makes difficult to record and resolve thin layers. The lack of low frequencies makes impossible to obtain the absolute value of a resolved parameter directly from the seismic data (Schlumberger, 2015a). The influence of a bandlimited seismic is shown in Figure 3-3.

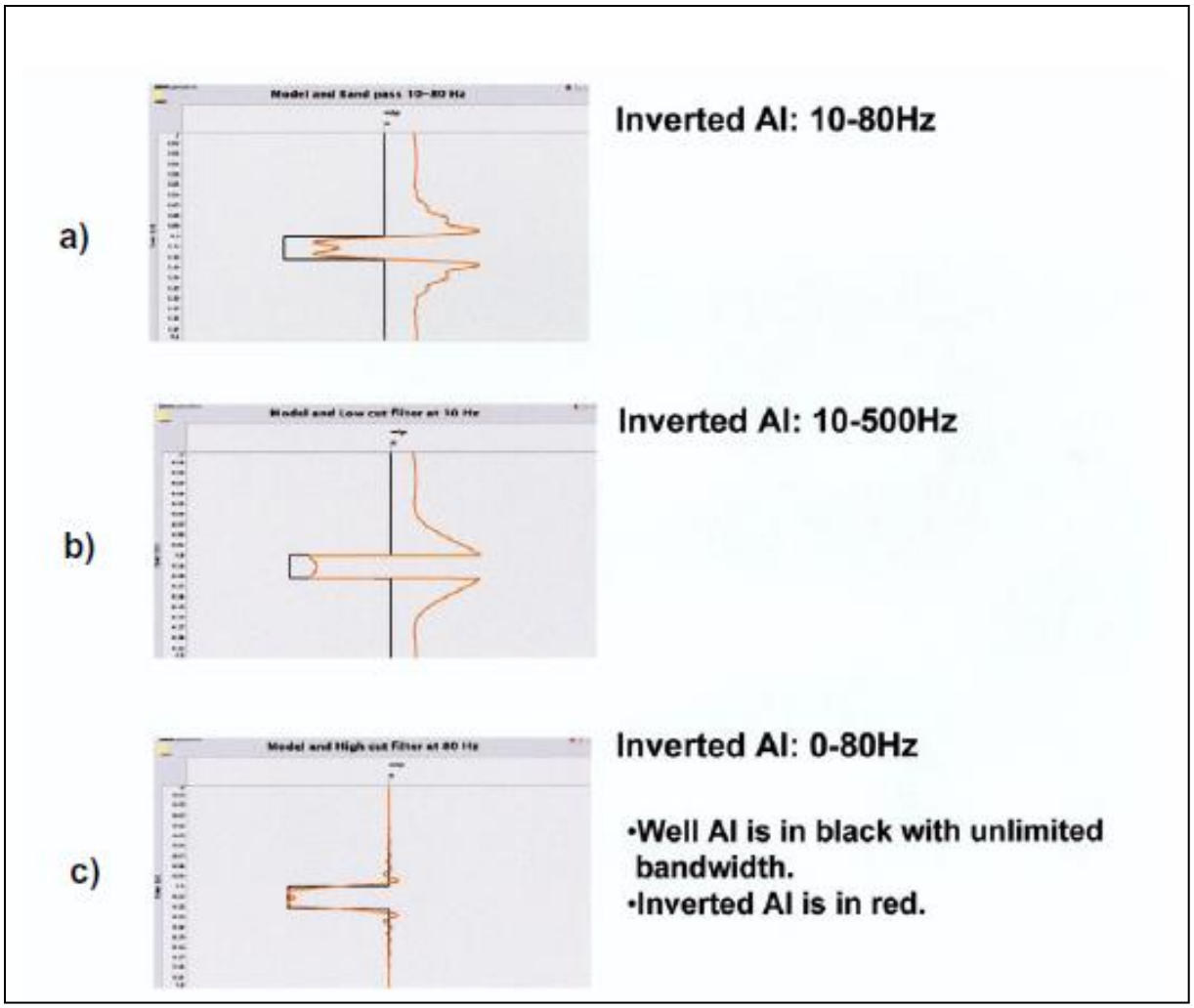

Figure 3-3. The problem of bandlimited seismic data in the inversion process. The black curve represents the true acoustic impedance values. The red curve simulates the results of the inversion of seismic data with different frequency content. A) Seismic data lack both low and high frequencies – the inversion does not resolve the true value of the acoustic impedance of the layer and the resolved thickness of the layer is slightly biased; b) Seismic data are missing low frequencies – the true value of acoustic impedance is not fully recovered but the boundaries of the layer are properly mapped; c) The inclusion of low frequencies into the seismic data allows recovering the true value of acoustic impedance and the boundaries of the layer are reasonably well mapped (Schlumberger, 2015a).

To obtain absolute values of the elastic property from seismic inversion, the missing low-frequency part of the seismic power spectrum is often introduced. It can be obtained by interpolation of the acoustic impedance logs, possibly guided by the interpreted seismic horizons (Simm and Bacon, 2014). A general flow-chart for a model-based seismic inversion is shown in Figure 3-4. The starting point of a model-based inversion are the individual traces of the low-frequency model. Each trace is perturbed and checked against the corresponding seismic trace until the misfit is minimized. The misfit is calculated between the observed seismic trace and the synthetic seismic trace obtained by convolving the reflectivity derived

from the perturbed trace with a seismic wavelet. The starting model is often called a low-frequency model (LFM) or a trend.

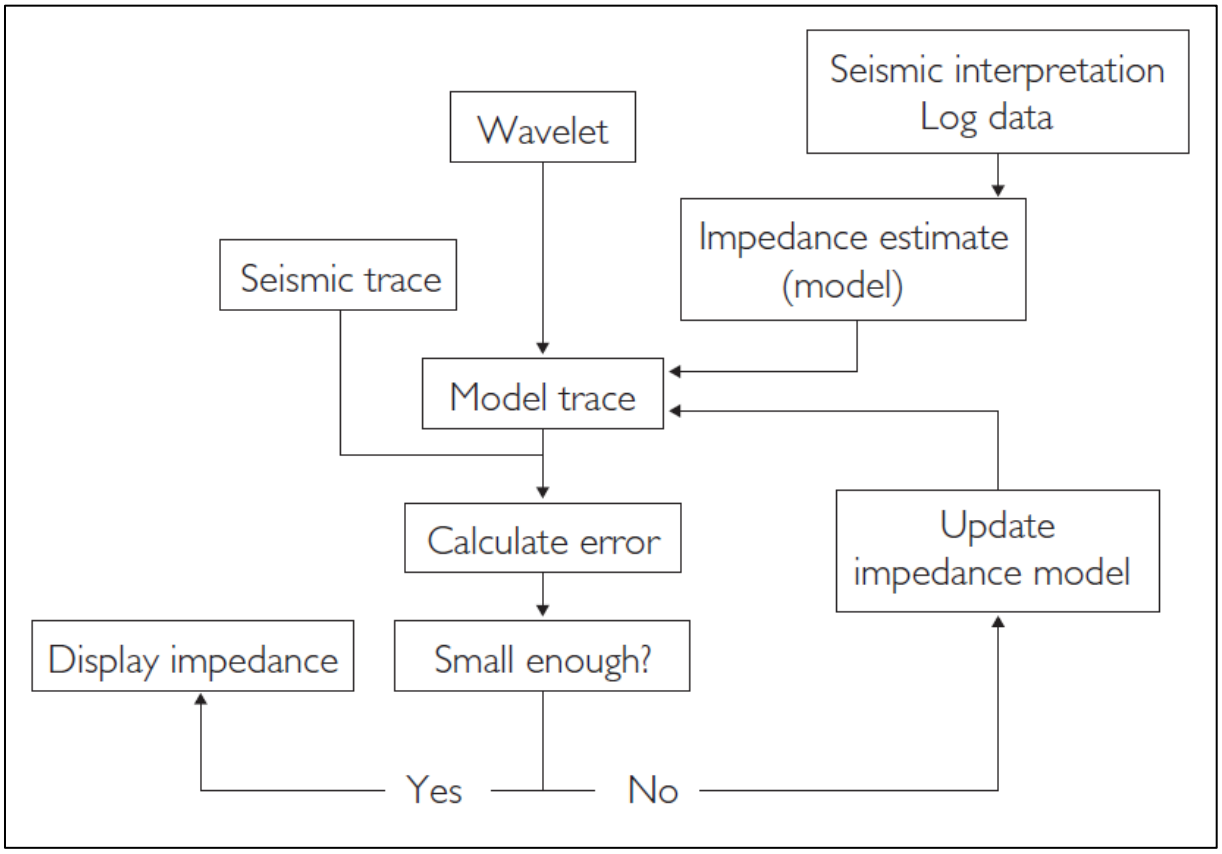

Figure 3-4. Generalized flow-chart for a model-based inversion. Well log data and seismic horizons are used to derive the low-frequency impedance model. Each model trace is converted to reflectivity and convolved with a wavelet to calculate the synthetic seismic trace. The synthetic trace is checked against the seismic trace and if the misfit is too large, the impedance model is updated in the next iteration until the misfit reaches a tolerable error level (Simm and Bacon, 2014)

The amplitude of a seismic reflection depends on the angle of incidence of the seismic ray with the reflector and the elastic property contrasts at the reflector. This dependence is known as amplitude versus offset (AVO) or amplitude versus angle (AVA) effect since the offset can be transformed into an incidence angle and vice versa. AVO effects can be incorporated into the seismic inversion to learn more about the elastic properties of the subsurface. Figure 3-5 conceptually shows the AVO/AVA effect for one seismic event. For non-zero angles, the P-wave energy is split into the reflected P-wave, the reflected S-wave, the refracted (transmitted) P-wave, and the refracted (transmitted) S-wave. At the critical angle, the amplitude of the reflection changes dramatically and the refracted wave travels parallel to the boundary. The angle-dependent amplitude changes are described by the Zoeppritz equations. Because these equations are complicated and unintuitive, several authors derived approximations for pre-

critical angles (Simm and Bacon, 2014). The popular three-terms approximation of the reflection coefficient R as a function of the incidence angle θ was developed by Aki and Richards (1980) and rearranged by Shuey (1985) into the form: $R(\theta) \approx A + B\,sin^2\theta + C\,sin^2\theta\,tan^2\theta$, where A is the intercept, B the gradient, and C the curvature term of the equation (Buland, 2019). The intercept is the zero-angle reflection coefficient dependent on the contrast of acoustic impedance. The gradient introduces the effects of shear velocity at non-zero angles, and the curvature determines the reflection coefficient near the critical angle. The A, B, and C terms can be expressed as functions of Vp, Vs, and density (Simm and Bacon, 2014). Other popular names for these three terms are given in Figure 3-5b. AVO effects can be included in the interpretation by calculating angle stacks. The available incident angle range is often divided into three or more equal parts, resulting in e.g. near, mid, and far angle stacks or near, mid, far, and ultra-far angle stacks. The angle stacks allow maintaining proper signal-to-noise ratio while making AVO interpretation possible (Simm and Bacon, 2014).

Before the 1990s it was common to assume that the full-stack seismic data represents the normal incidence reflections and can be simply inverted to acoustic impedance with AVO effects ignored. This type of inversion was called post-stack inversion. Inversion of the data representing the zero-incidence reflection such as a near partial stack or AVO intercept results in acoustic impedance. Inversion of non-zero incidence data results in modified impedance. Pre-stack seismic inversion utilizes the fact that the reflection strength from a subsurface interface depends on the reflection angle and on the material properties where the reflection takes place. AVO inversion is a pre-stack inversion technique for estimating the elastic parameters of the subsurface (Buland, 2019; Buland and Omre, 2003; Simm and Bacon, 2014).

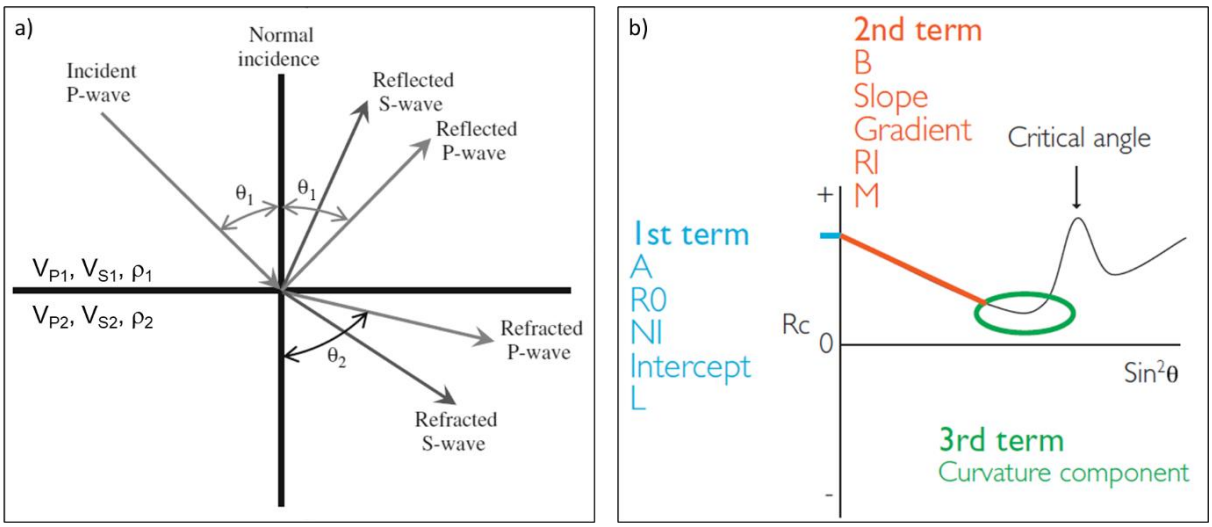

Figure 3-5. Effect of the angle-dependent amplitude of the reflected seismic P-wave. A) Seismic waves generated by the P-wave hitting the reflector. The amplitude of the reflection depends on the incidence angle and elastic properties of the layers (modified from Bjorlykke, 2010) b) The amplitude of the reflected P-wave for angles lower than the critical angle can be described by approximations of the Zoeppritz equations that incorporate three terms: the intercept, the gradient, and the curvature (Simm and Bacon, 2014)

Simultaneous AVO inversion is a model-based inversion method that uses all seismic inputs (e.g. all angle stacks) at the same time – therefore its name. The input angle stacks are usually aligned before inversion. Seismic trace alignment is a data processing step, which adjusts for small residual mismatches between the stacks to optimize the data for the inversion workflow. The output of the inversion are the volumes of Vp, Vs, and density, which could be further used to create other elastic properties such as Vp/Vs ratio, Young and shear moduli (Schlumberger, 2015a; Simm and Bacon 2014). The flow-chart of a simultaneous AVO inversion is shown in Figure 3-6. Each trace of the low-frequency models of Vp, Vs, and density is modified to include a high-frequency component. Then, using the Zoeppritz equations (or their approximations) it is transformed into an angle-dependent reflectivity, and by convolution with the wavelet derived for each angle stack, the synthetic seismic trace for each angle stack is obtained. All synthetic traces are checked against the corresponding measured seismic traces and if the difference is too large the low-frequency models are updated and checked until the error is minimized.

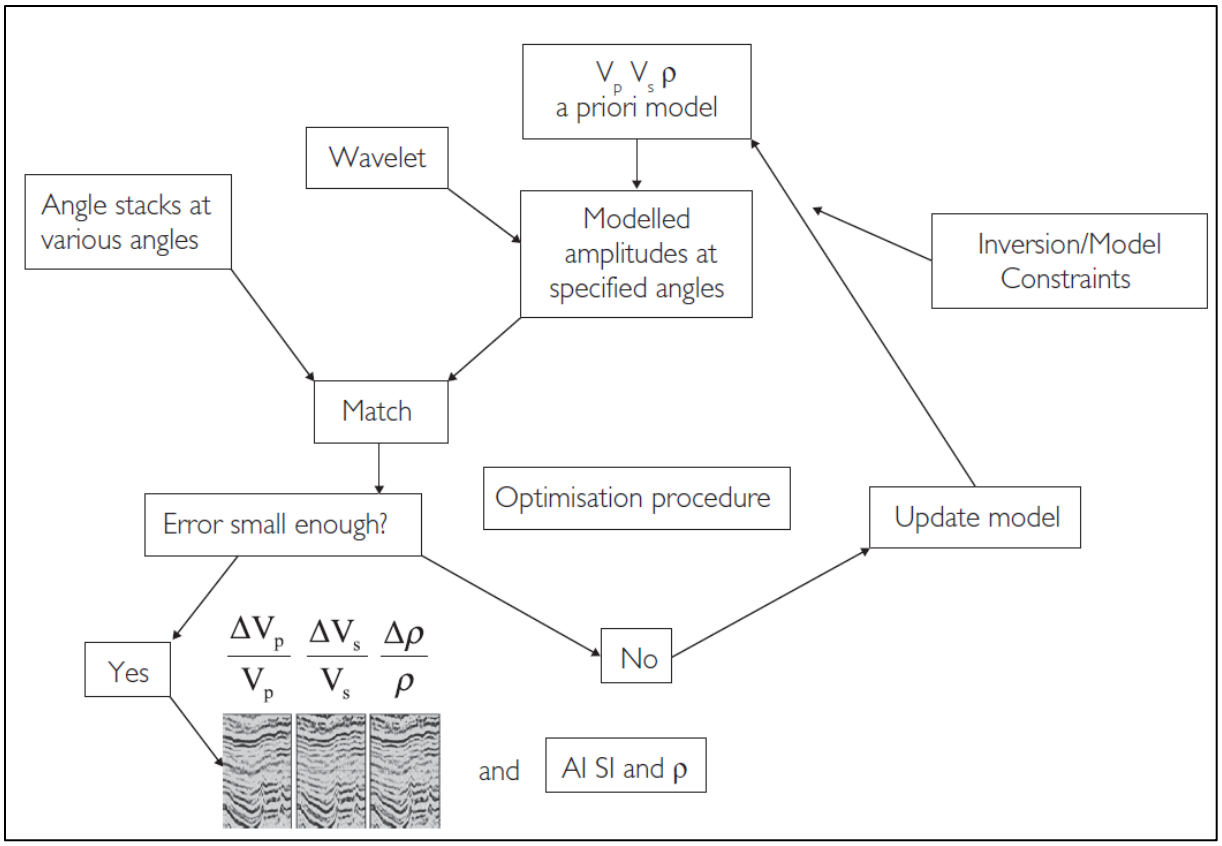

Figure 3-6. Flow-chart of simultaneous AVO inversion. Low-frequency models (here a priori models) are transformed into angle-dependent reflectivity traces, convolved with a wavelet, and checked against traces in the angle stacks. If the misfit between synthetic and observed traces is too big, the model is updated until the misfit is minimized (Simm and Bacon, 2014)

3.3.2. Stochastic (geostatistical) AVO inversion

Due to the non-unique character of seismic inversion, there is always uncertainty associated with an estimated elastic property. This uncertainty should be propagated through the inversion workflow and included in the inversion solution. A probabilistic setting is a natural choice to account for the non-uniqueness of the inversion. There are two main approaches to seismic inversion in a probabilistic framework: Bayesian inference, and iterative stochastic sequential simulations (Azevedo et al., 2018; Buland and Omre, 2003). The latter one is used in this thesis.

The geostatistical inversion honors the seismic and the low-frequency component (LFM) – similarly to the deterministic inversion – but additionally it uses a variogram model to include high-frequency information into the solution as conceptually shown in Figure 3-7. The variogram model introduces high frequencies into the inversion solution, but it does not increase the seismic resolution, which is limited by the bandwidth of the seismic data. High frequencies are not inverted from seismic but simulated using a variogram model (Doyen, 2007).

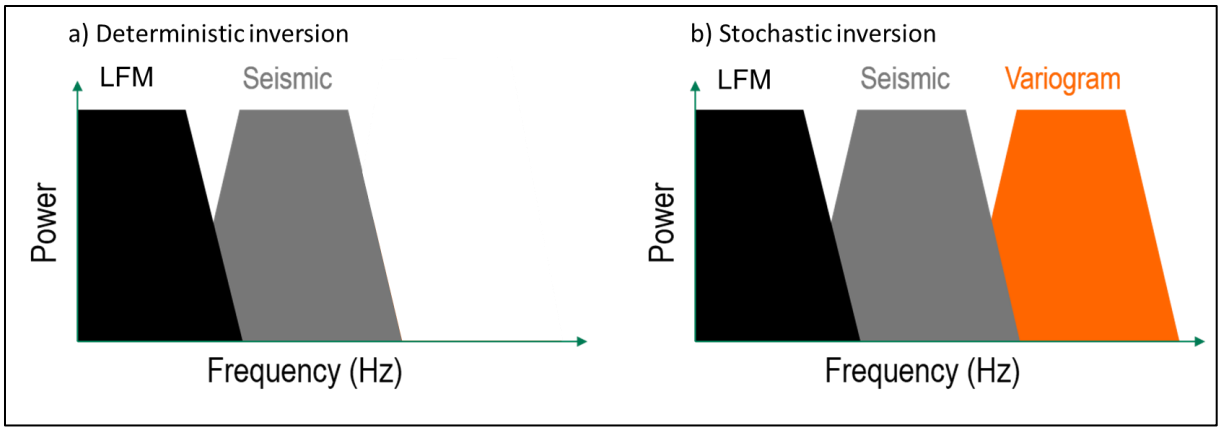

Figure 3-7. Frequency spectra and data sources for a) deterministic seismic inversion and b) stochastic (geostatistical) seismic inversion. Low-frequency model (LFM) constructed by interpolation of filtered well logs controls the low frequencies, seismic controls the intermediate frequencies within seismic bandwidth, and vertical variogram controls the high frequencies (Doyen, 2007; Schlumberger, 2015b)

The geostatistical AVO inversion is commonly done within a 3D geomodel grid in a trace-by-trace approach, which can be summarized by the following workflow (Azevedo et al., 2018; Russel, 2016; Schlumberger, 2015b; Simm and Bacon, 2014):

1) Upscale well logs of Vp, Vs, and density into the geomodel cells
2) Populate geomodel cells with low-frequency models of Vp, Vs, and density
3) Select a random path through all seismic trace locations (each location will have e.g. near, mid, and far trace). For each location perform a local optimization:
    a. Remove the trend from the upscaled log data through subtraction of the low frequency models to work with the residuals of Vp, Vs, density (part of sequential Gaussian simulation)
    b. Interpolate the residuals of Vp, Vs, density using sequential Gaussian simulation and add the low-frequency models to obtain the absolute value
    c. Convert Vp, Vs, and density into an angle-dependent reflectivity and convolve it with a wavelet from each angle stack to derive the synthetic trace for each angle stack
    d. Compare synthetic traces (near, mid, and far) with seismic traces (near, mid, and far) and iteratively update the model until the misfit is minimized and retain this model of Vp, Vs, density
    e. Go to the next trace and treat the already simulated trace location as an input (upscaled) data
4) Select a different random path through trace locations to obtain next realization of the stochastic AVO inversion

The seed value controls the random path through the traces and the sequential Gaussian simulation. Figure 3-8 summarizes the parameters controlling the stochastic AVO inversion algorithm. It can be observed that with an increasing number of iterations, the correlation coefficient between the "truth" and fitted trace increases.

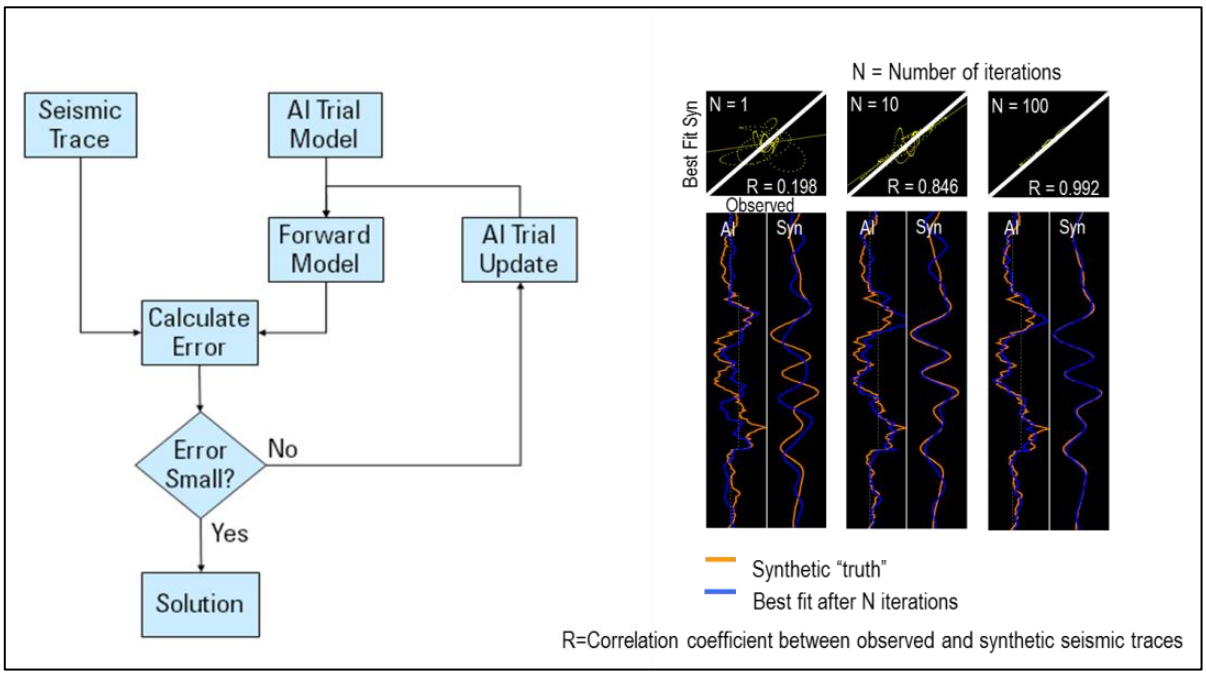

Figure 3-8. The principle of the stochastic seismic inversion algorithm showcased on one seismic trace inversion for acoustic impedance (Schlumberger, 2015b)

3.4. Simulation

3.4.1. Sequential Gaussian simulation

Sequential Gaussian simulation (SGS) is a stochastic simulation algorithm used for sparse, continuous data, e.g. modeling the porosity in the geomodel using well data and spatial continuity information – the variogram. It requires that the input data have a standard normal score distribution (the mean is zero and the standard deviation is one). It also assumes stationarity so the mean of the data does not change laterally and spatial statistics do not depend on location (Schlumberger, 2015b).

The variogram 2γ expresses the spatial variation of the input parameter. The experimental variogram is calculated as a squared difference between the pairs of data that are separated by a given distance. For convenience, the semivariogram function γ is used in practice, and often the name variogram refers to semivariogram. The experimental semivariogram γ of a variable

$Z(x)$ is expressed as $\gamma = \frac{1}{2N}\sum[Z(x+h) - Z(x)]^2$, where N is the number of all data pairs separated by a lag distance h. Generally, γ is a measure of spatial dissimilarity and increases with distance because points that are closer to each other are more likely to have similar values. Fitting an analytical trend line through the experimental variogram points produces a variogram model function that can be used as an input to geostatistical algorithms such as kriging. The conceptual experimental and model variogram is shown in Figure 3-9. A variogram model has three defining features: the sill – a constant which approximates the variance of a dataset; the range – a distance at which the sill is reached; and the nugget – the extrapolated value at zero separation. The nugget informs about a sudden jump in dissimilarity between points or in other words, small-scale variation. It often arises due to measurement error or lack of data for small separation distances. It is assumed that the input log data is reliable and therefore the nugget should be set to zero when modeling the variogram for inversion or reservoir properties. The key measure for reservoir modeling is the range – it informs about the distance at which the pairs of data have no relationship to each other, that is they are not correlated. The influence of the variogram range on the simulation is shown in Figure 3-10. A large range means that data points remain correlated over large distances and areas. Variogram models for perpendicular horizontal directions can be established to capture a possible anisotropy. Variogram models can be expressed with various mathematical functions. Some of the popular variogram models are: spherical – which is a good general model; exponential – which produces the noisiest result; and Gaussian – which produces the smoothest result (Schlumberger, 2015b; Ringrose and Bentley, 2014).

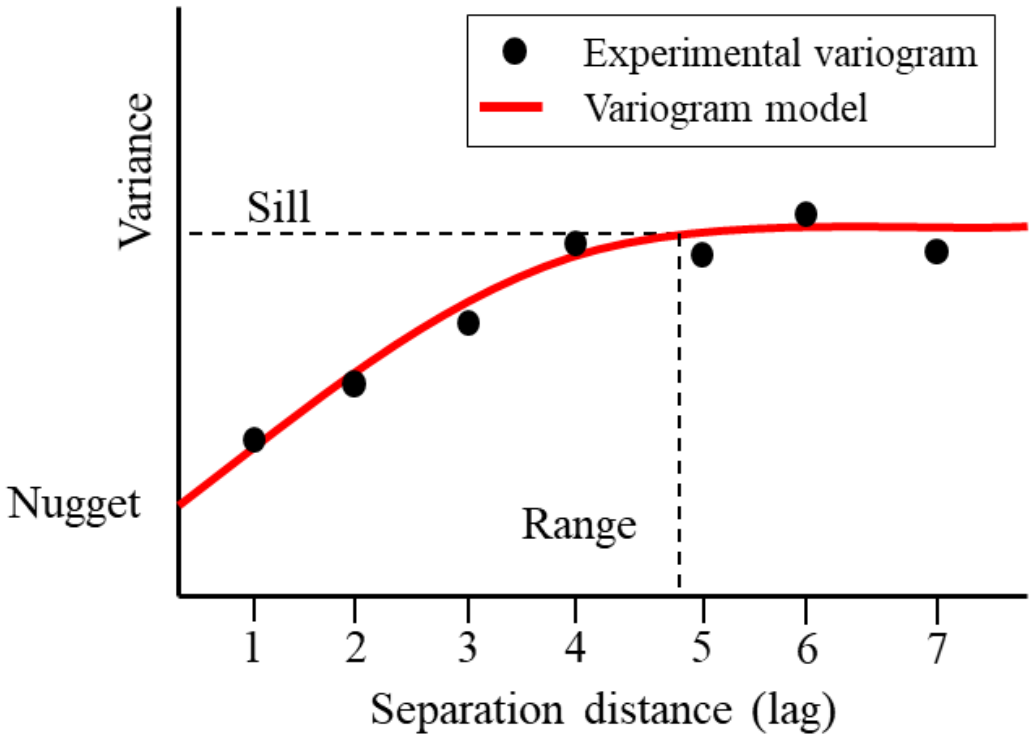

Figure 3-9. Visualization of the semivariogram. In practice, the semivariogram is often called the variogram. The experimental variogram calculates the variance between data pairs in the dataset separated by a specific distance (lag). The variogram model is fitted to experimental points and is used by geostatistical algorithms (kriging, SGS, SIS, etc.). Modified from Schlumberger (2015b)

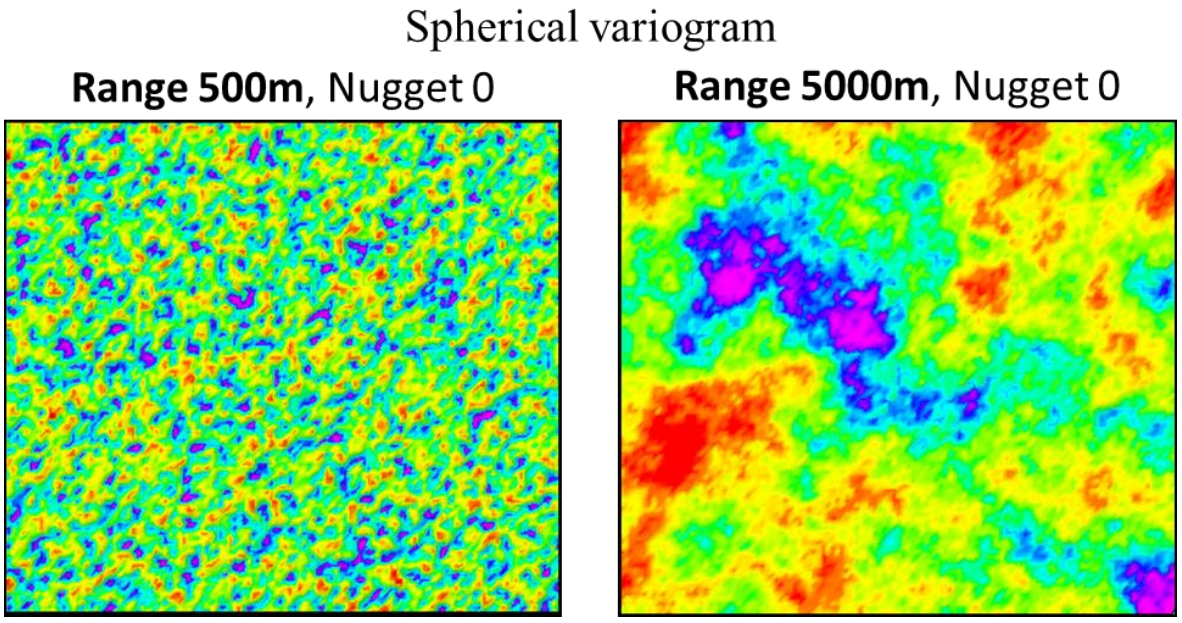

Figure 3-10. The influence of a variogram range on one realization of a sequential Gaussian simulation. Higher range results in larger patches of high and low values. Modified from Schlumberger (2015b)

Kriging aims to estimate a spatial property Z^* at the unmeasured location based on known values of Z_i at locations x_i. It is a weighted sum of the known values expressed as $Z^* =$

$\sum_{i=1}^{n} \omega_i Z_i$, where ω_i are the weights that minimize the expected variance. The weights are calculated using the variogram model and depend on the spatial configuration of the data points. Kriging uses data points that are located within the range of the variogram, i.e. according to the geological knowledge, they are correlated with the estimated cell. If there are no data points within the variogram range, the mean value given by all data points will be assigned to the cell. Kriging delivers a kriged value and variance for each estimated point (Schlumberger 2015b; Ringrose and Bentley, 2014).

The simulation principle is shown in Figure 3-11. After obtaining variograms and a normal score transformation of the input data, SGS uses kriging to calculate the estimated kriging value and the kriging variance at each grid point. The conditional cumulative distribution function (CCDF) is derived from the kriging variance and its inflection point moved over the kriged value as shown in Figure 3-11. Then a random number is drawn between zero and one and applied to the CCDF. This delivers the simulated value which is assigned to the grid cell. An important part of Gaussian simulation is that it utilizes already simulated cells in the kriging process (it treats them as new datapoints). Equiprobable realizations are obtained by the selection of a semi-random path through the model grid and providing different random numbers for each simulation. A specific parameter (called seed) controls the random path and the random number. This ensures that any simulation is reproducible as it is linked to a specific seed number (Schlumberger, 2015b).

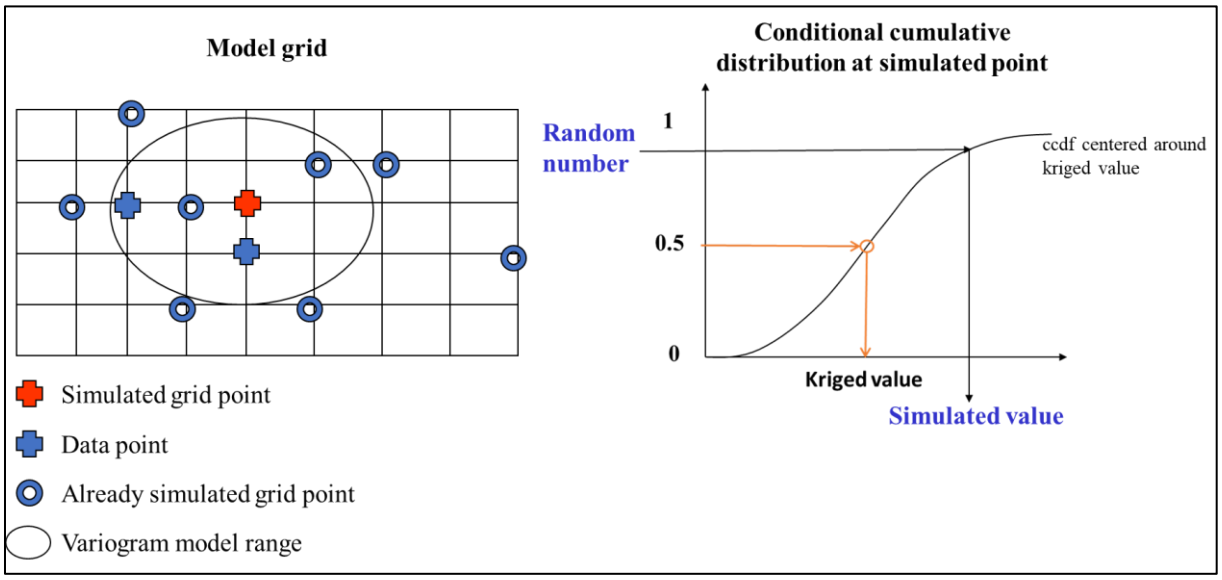

Figure 3-11. Simulation based on the SGS algorithm for one cell in a model. Kriging is used to calculate kriging value and variance at a simulated grid point using all data points and previously simulated grid points within the variogram range. Kriging deliver a kriged value and a distribution of its uncertainty, represented by the CCDF

(Conditional Cumulate Distribution Function). The CCDF is randomly sampled to deliver the simulated value. In the case of SGS, which is used for the geostatistical AVO inversion, the simulated parameters will be often P-impedance, S-impedance, and density in the cells along the seismic trace. Modified from Schlumberger (2015b)

3.4.2. Sequential indicator simulation for facies modeling

Sequential indicator simulation (SIS) is a pixel-based simulation method used for a sparse, discrete property such as facies. SIS can be easily integrated with probability trends derived from seismic volumes. SIS is a generalization of the SGS algorithm and uses indicator kriging as a tool to derive the probability of facies occurrence at a given point, taking into account data points inside the variogram range (Schlumberger, 2016).

The principle of SIS is given in Figure 3-12. The algorithm similarly to SGS uses variogram models, kriging and seed values which are used to generate pseudo-random paths over the grid. At each grid cell the probability of encountering specific facies is calculated using kriging. This is done in the following way: Let us assume that the probability of sand at a grid cell shall be calculated. Then all data points that show sand get the value 1 and the remaining data points get the value 0 – the probability of encountering sand at these points. Also, the grid points that already got a calculated sand probability will be taken into account. These probability values are interpolated and deliver the sand probability for the grid cell under consideration. This procedure is done for all facies of the model. These probability values are used to calculate the conditional cumulative distribution function (CCDF) for the grid cell. Then, the cumulative distribution is sampled using one random number controlled by the seed number to obtain the facies and the algorithm moves to the next random cell. The global fraction or the global distribution is an overall presumed percentage of facies constituting the reservoir and can be obtained using well data. If there are no data points within the range of the variograms, the global facies fraction given by the well data will be used to create the cumulative distribution function. The chosen variogram range will have an impact on how influential the global fraction is. Small ranges will increase the influence of the global fraction, whereas large ranges will diminish its influence (Schlumberger, 2016).

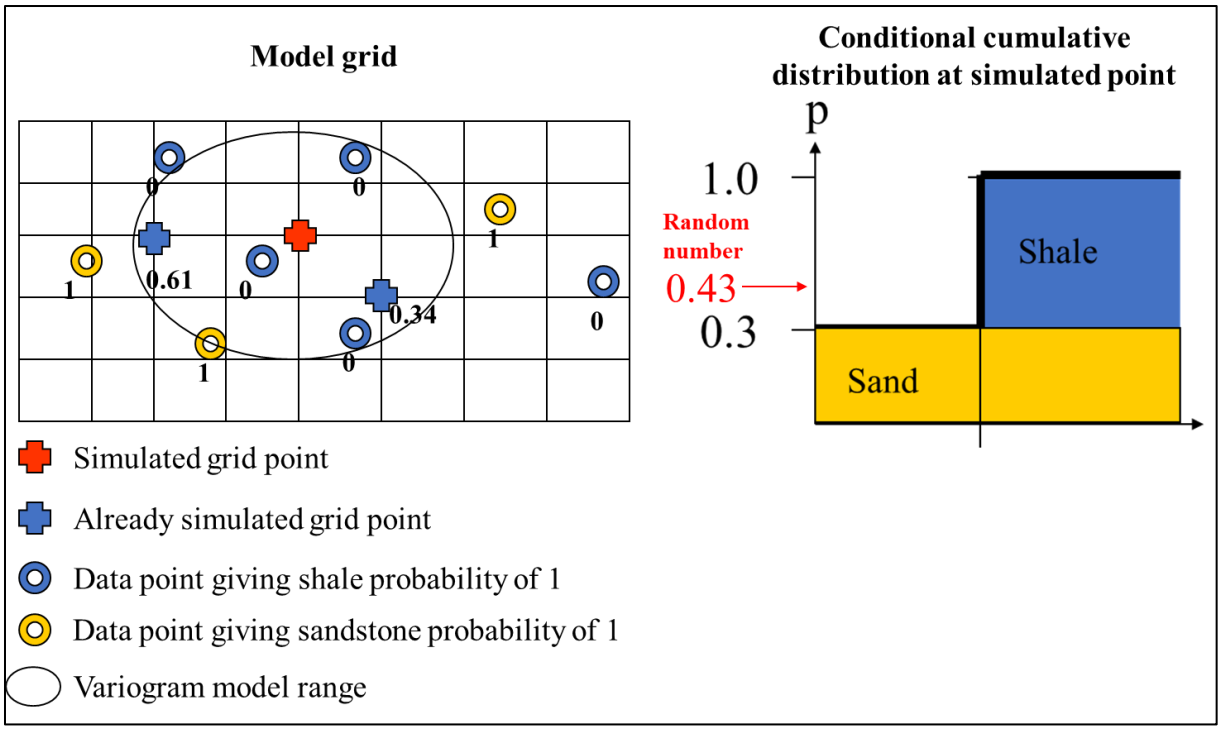

Figure 3-12. Facies simulation with sequential indicator simulation. The probability distribution of simulated facies is calculated using indicator kriging and randomly sampled to obtain the simulation outcome. Modified from Schlumberger (2016)

4. Data

The dataset consists of seismic angle stacks, key horizon surfaces, and well log data. The 3D seismic survey ST0823D14 is an ocean bottom cable survey acquired over the J-structure in the Oseberg Sør field for Equinor ASA in 2008. In this thesis, P-wave angle stacks in time domain were used, near stack (0-15°), mid stack (15-30°), and far stack (30-45°). The seismic was processed to zero-phase data with normal polarity, so a positive amplitude reflects an increase in acoustic impedance. A positive seismic amplitude is indicated by red color throughout this thesis. The sampling interval is 4 ms. The power spectrum of seismic data in the reservoir zone (-1800 to -2800 ms) is shown in Figure 4-1. The approximate seismic frequency range at -10 dB is 4-40 Hz.

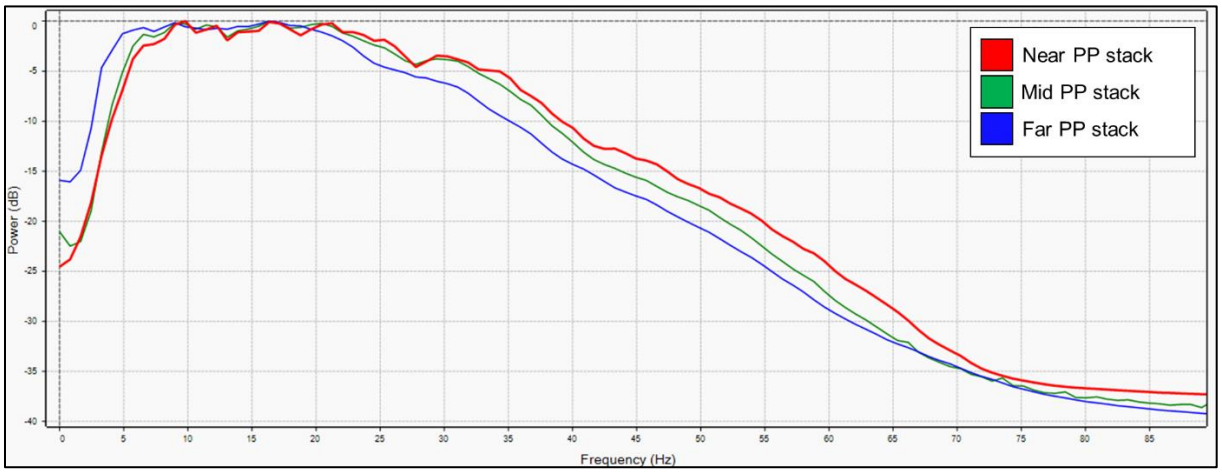

Figure 4-1. Power spectrum of angle stacks. Approximate seismic bandwidth at -10 dB is 4-40 Hz

Twelve wells with well log data and tops are available. Table 4-1 summarizes the most important well logging data available and Figure 4-2 shows their locations. A shear sonic log is available for the majority of the wells. Additionally, in all wells Vp/Vs ratio data are present. One of the limitations of the dataset is that only four wells have a facies log.

Table 4-1. A summary of the most important well logging data available in the area

	Checkshots	P-sonic	S-sonic	Vp/Vs	Density	Facies log
30/9-5S	X	X	X	X	X	X
30/9-6	X	X	X	X	X	
30/9-9	X	X	X	X	X	X
30/9-11	X	X	X	X	X	

30/9-11A	X	X		X	X	
30/9-15	X	X		X	X	X
30/9-18		X	X	X	X	
30/9-20S	X	X	X	X	X	
30/9-25		X	X	X	X	
30/9-J-12		X	X	X	X	
30/9-J-13	X	X	X	X	X	X
30/9-J-16		X	X	X	X	

The interpreted key surfaces for the thesis include the top Shetland Gp., top Brent Gp., top Drake Fm. and top Cook Fm. Other interpreted surfaces are also available. The horst structure is visible on the map of the top Brent Gp. in Figure 4-2. A near stack seismic section along the horst is shown in Figure 4-3.

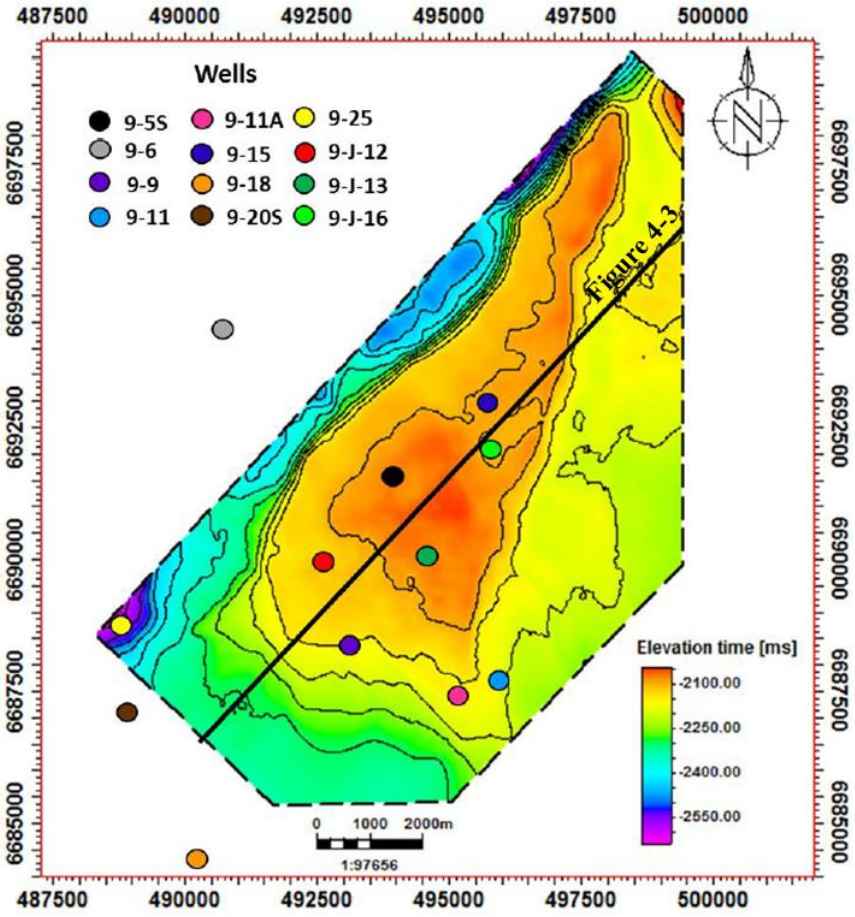

Figure 4-2. Interpretation of top Brent Group provided by Equinor ASA and location of the available wells. The contour interval is 50 ms. SW-NS seismic section is shown in Figure 4-3. Modified from Rotar (2019)

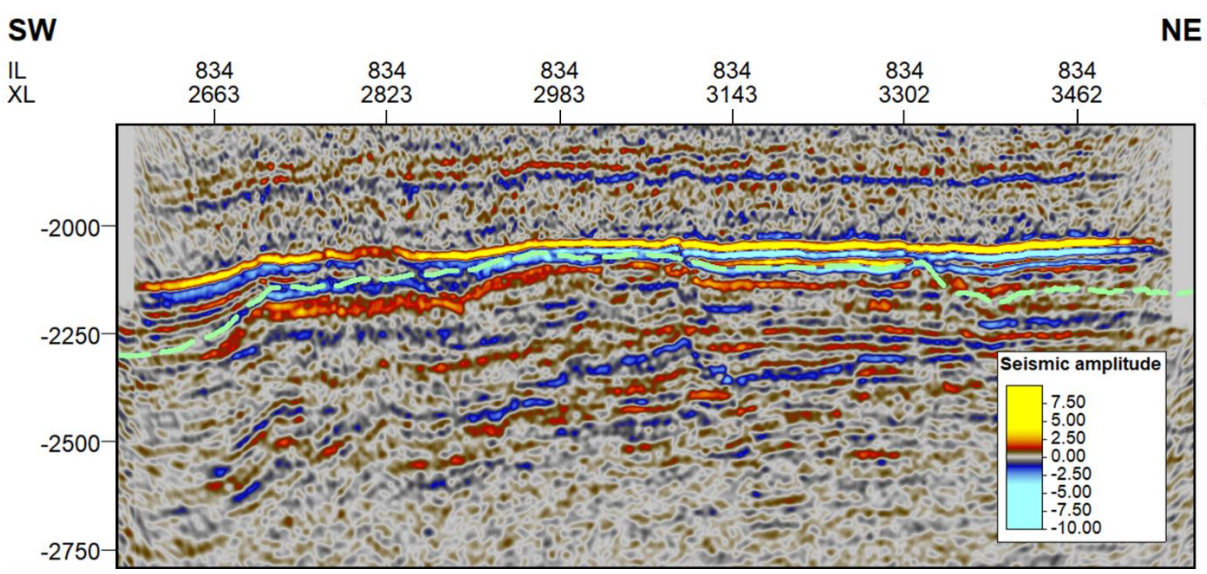

Figure 4-3. Seismic section showing the interpretation of the top Brent Group (dashed green) on the near angle stack. See Figure 4-2 for location. High amplitude seismic reflectors (yellow and light blue) are most likely related to carbonates

5. Methodology

Obtaining facies models using the deterministic or the stochastic AVO inversion is presented below as two separate workflows. Before the execution of the workflows, the seismic-well ties were established and the geomodel was built to further populate it with facies. The details about each step are given in the following subsections.

The general workflow for deriving facies models using the deterministic AVO inversion is shown in Figure 5-1. The starting point of facies modeling guided by the deterministic inversion is a rock physics study using the well data. Based on the rock-physics study, a litho-predictor is constructed in the form of probability density functions (PDFs) for each facies. It assigns the probability of encountering facies to the combination of acoustic impedance and Vp/Vs ratio. This litho-predictor is applied to the acoustic impedance and Vp/Vs ratio volumes obtained from the deterministic AVO inversion, which results in three new volumes: the sandstone, shale and carbonate probabilities. These volumes are resampled into the geomodel cells and used to guide the sequential indicator simulation (SIS), which delivers multiple, equiprobable realizations of facies distribution. Finally, in each model the volume of each facies is calculated to allow comparison with the stochastic AVO inversion.

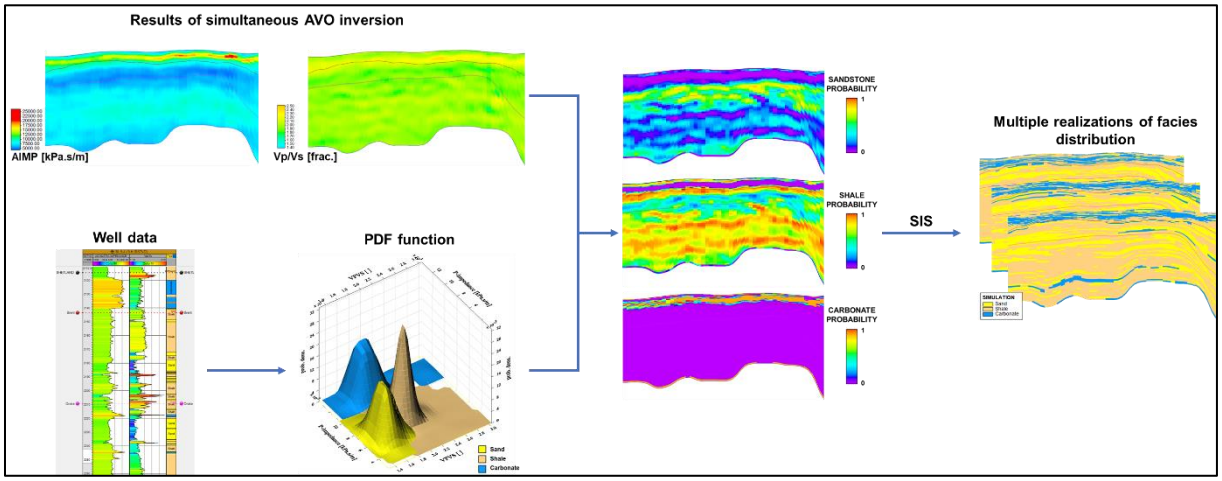

Figure 5-1. The workflow to obtain facies models using the deterministic AVO inversion. The well section includes the acoustic impedance log, the Vp/Vs ratio log, and the facies log. Well data are used to create probability density functions (PDFs) that can be applied to acoustic impedance and Vp/Vs ratio volumes from the deterministic AVO inversion to derive facies probabilities. The probabilities are then used to guide a sequential indicator simulation that delivers multiple, equiprobable realizations of facies distributions

The facies modeling workflow utilizing the stochastic AVO inversion is shown in Figure 5-2. PDFs are derived in the same way as described above and they are directly applied to multiple realizations of the acoustic impedance and Vp/Vs ratio from the stochastic AVO inversion. This

results in multiple, equiprobable facies models. The volume of each facies for each model is calculated for comparison.

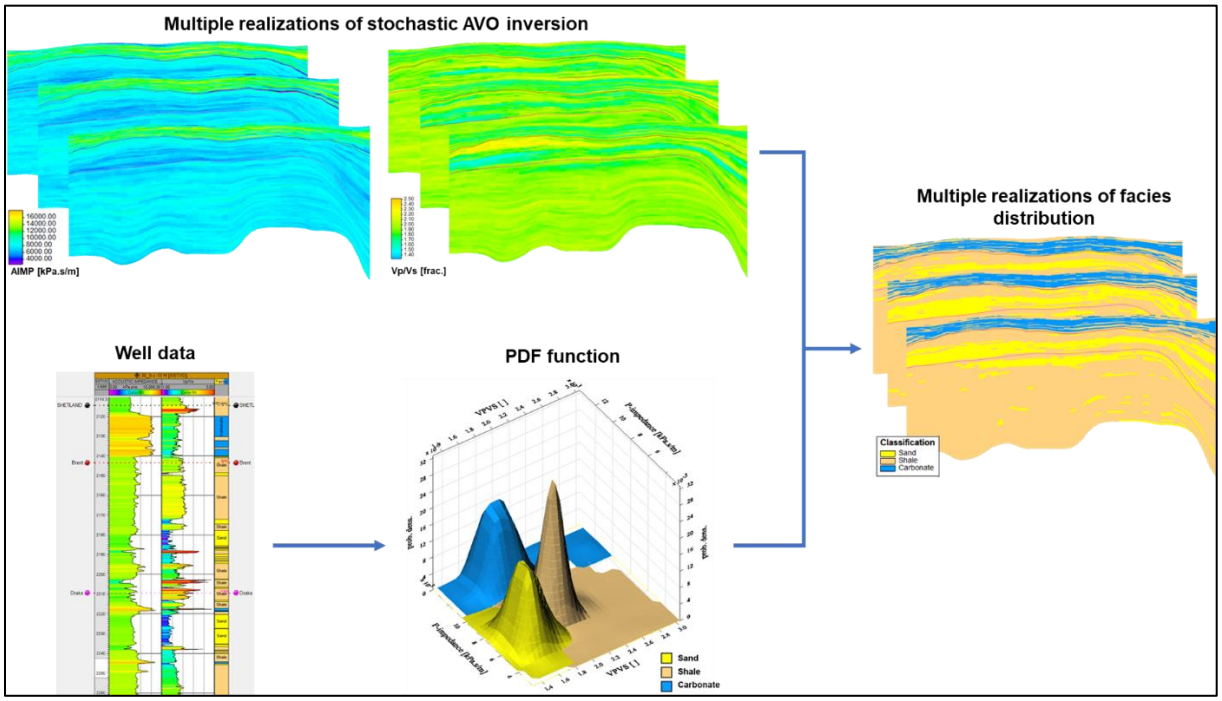

Figure 5-2. The workflow to obtain multiple equiprobable facies models using the stochastic AVO inversion. The well section includes the acoustic impedance log, the Vp/Vs ratio log, and the facies log. Well data are used to create probability density functions (PDFs) that can be applied to multiple realizations of acoustic impedance and Vp/Vs ratio volumes from the stochastic AVO inversion. This results in multiple, equiprobable facies models

5.1. Seismic-well ties

Time-depth relationships between wells and seismic were established using checkshots and ISIS frequency wavelets. The important seismic reflectors were identified and the interpretation of the key surfaces provided by Equinor ASA were visually quality controlled to check if the surfaces follow the seismic reflectors. Figure 5-3 presents an example of a seismic-well tie for well 30/9-5S. The top Shetland Gp. surface was identified as a high-amplitude positive reflector (hard-kick), easy to correlate across the study area. The top Brent Gp. and top Drake Fm. were also identified as positive reflectors with a much smaller amplitude. The top Cook Fm. was identified as a negative reflector. The established time-depth relationship shows a good match of synthetic seismic to real seismic, however, due to large relative differences in the reflector amplitudes, the residual trace shows relatively large misfit between the top Shetland and top Drake horizons.

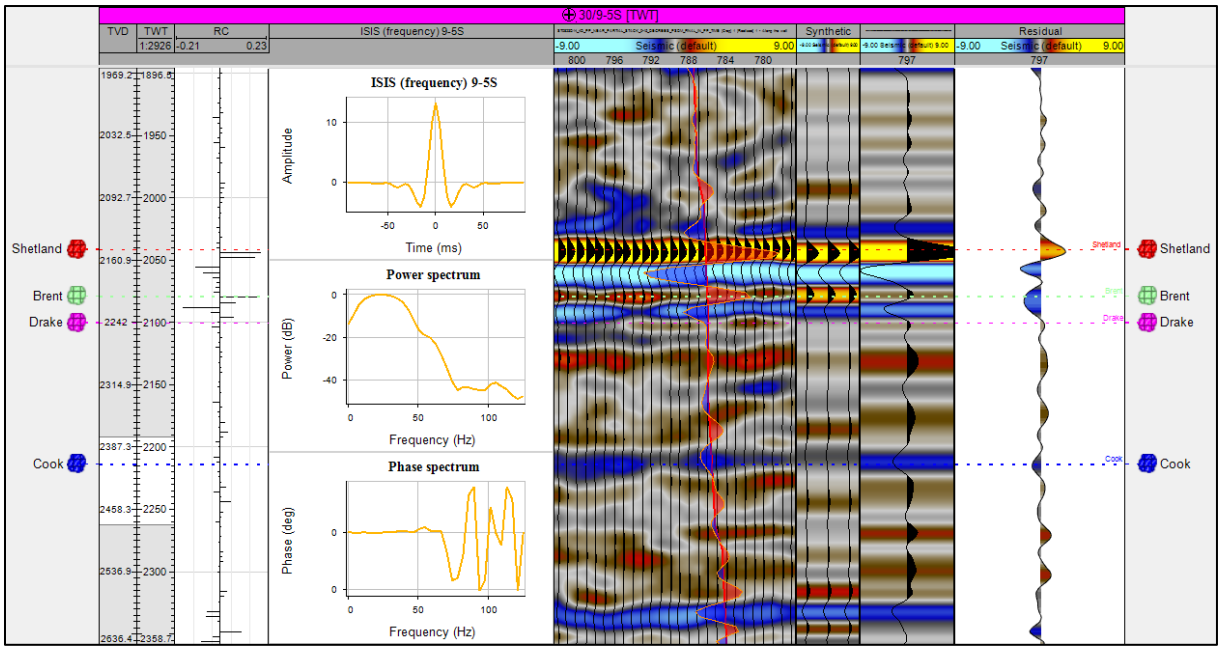

Figure 5-3. Seismic-well tie for well 30/9-5S

5.2. Geomodel building

The geomodel is needed to compare the results of the two approaches. In addition, it provides geostatistical tools essential for the workflows described above. The model was constructed using surfaces from the top Shetland Gp, top Brent Gp, top Drake Fm, and top Cook Fm, limited to the area of the horst structure, as shown in Figure 5-4. A 3D grid with a cell size of 50 m x 50 m was set up. The model consists of three zones (Fig. 5-5). The layering in the zones is based on a proportional zone division. The model parameters are summarized in Table 5-1.

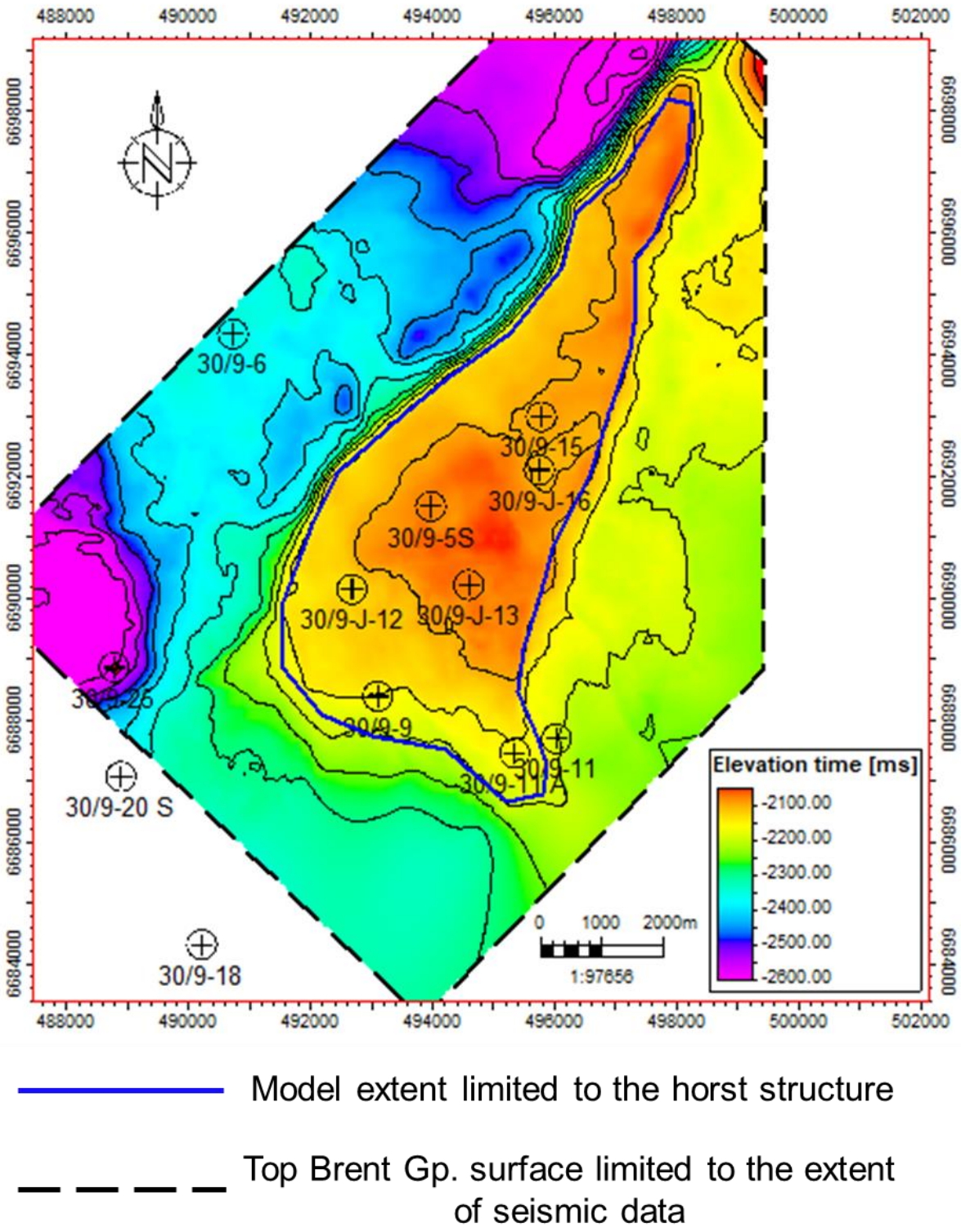

Figure 5-4. The extent of the model imposed on the map of the top Brent Gp. The model extent was limited to the horst structure

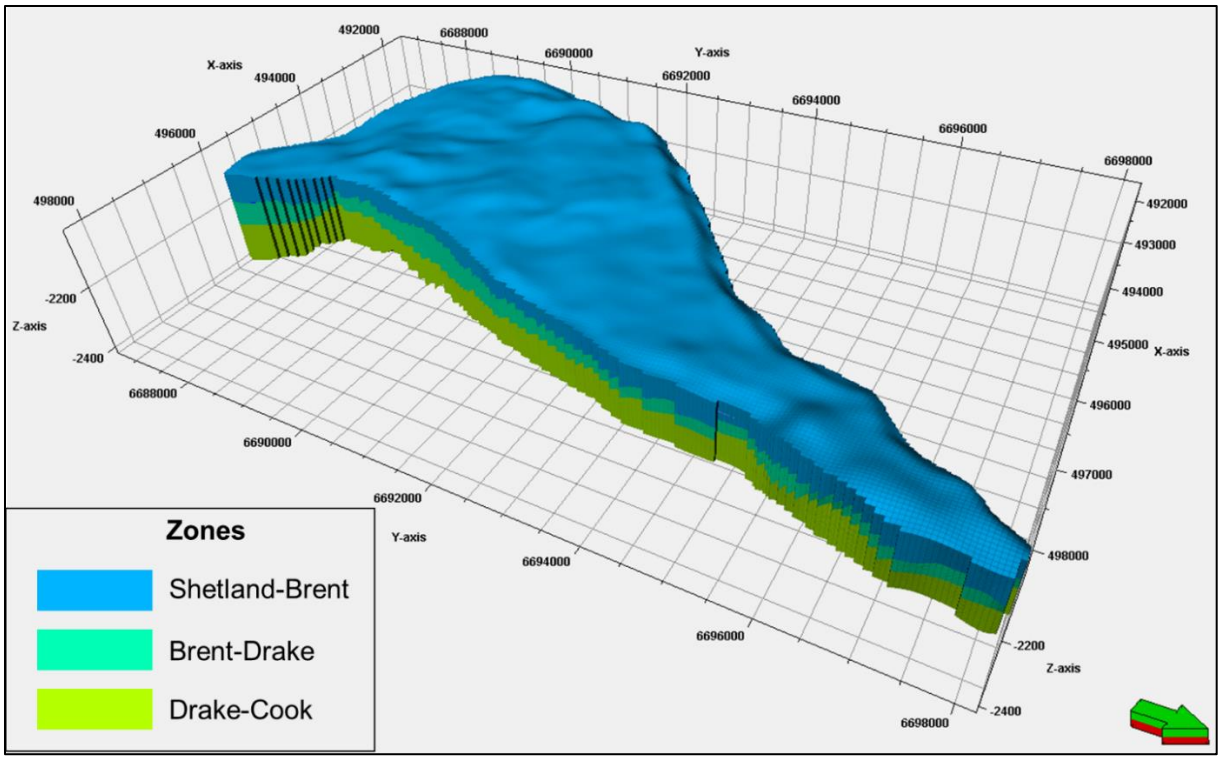

Figure 5-5. 3D geomodel of the J-structure of the Oseberg Sør field. The model is limited to the extent of the horst structure. The middle zone Brent-Drake is a reservoir zone

Table 5-1. The statistics of the geomodel used in the thesis

	Number of cells	Volume of cells [$*10^6$ m^3]	Number of layers	Avg. layer thickness [m]
Shetland-Brent	1 247 400	2149	40	1.73
Brent-Drake	623 700	1520	20	2.44
Drake-Cook	1 247 400	4989	40	4.00
In total:	3 118 500	8658	100	

5.3. Rock physics study and litho-classification

The rock physics study on wells drilled through the modeled interval shows that cross-plotting Vp/Vs ratio vs acoustic impedance allows the separation of facies clusters with some overlapping (Fig. 5-6). Facies logs were available only for wells 30/9-5S, 30/9-9, 30/9-J-13, and 30/9-15. Three facies from the facies logs were identified on the crossplot: sandstones, shales, and carbonates. The facies statistics are summarized in Table 5-2. Sandstones and shales show similar ranges of P-impedance but different ranges of Vp/Vs ratio which is best visualized when comparing P10 and P90 values from Table 5-2. 90% of sandstones have Vp/Vs ratio lower than 1.81, and 90% of shales have Vp/Vs ratio higher than 1.89. However, the crossplot

in Figure 5-6 shows the overlapping of sandstones and shales in the P-impedance domain. Carbonates are characterized by high P-impedance values, above about 11 470 kPa s/m, which allows separating them from siliciclastic. The overlapping between siliciclastic and carbonates is less severe than between sandstones and shales. The main facies identified by wells in the modeled interval is shale, with about 85% contribution to the total facies distribution (based on the number of points in Table 5-2).

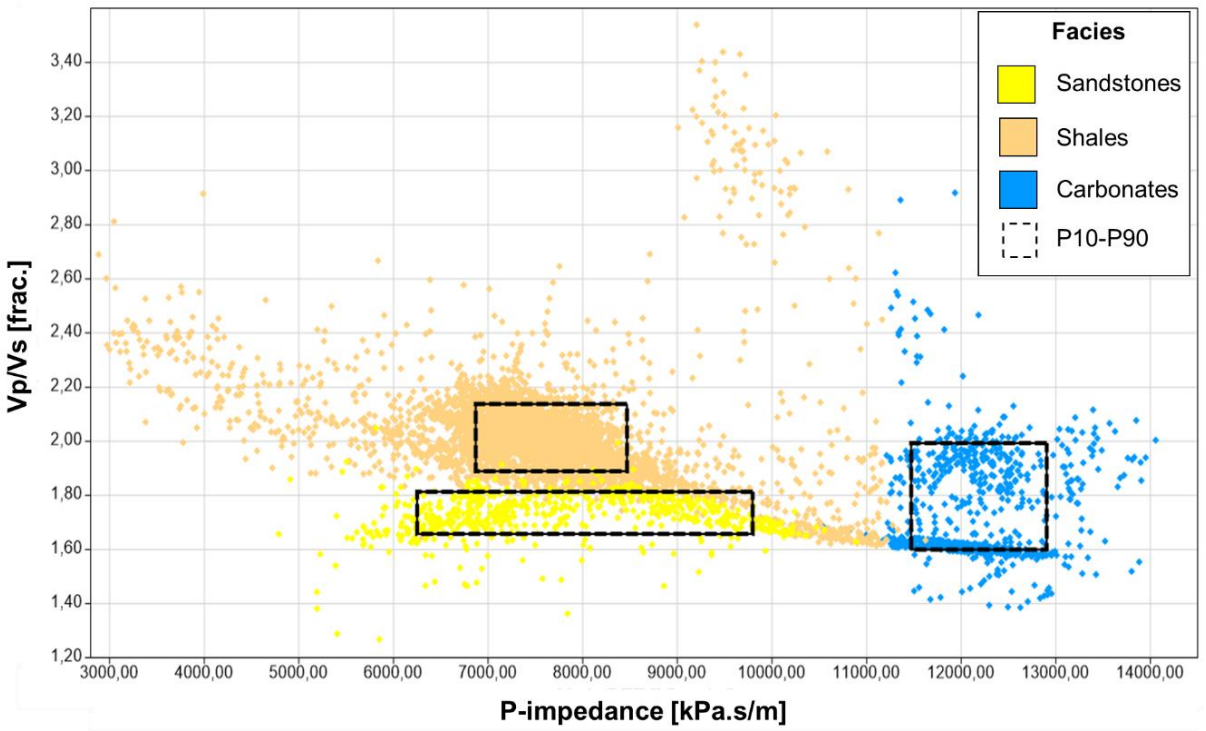

Figure 5-6. Crossplot of Vp/Vs ratio vs P-impedance color-coded by facies constructed using well log data from the top Shetland Gp. – top Cook Fm. interval. The data come from wells with the facies logs available: 30/9-5S, 30/9-9, 30/9-J-13, 30/9-15. The P10-P90 percentiles identified for each facies are consistent with values in Table 5-2

Table 5-2. Facies statistics derived from the rock physics analysis. P10, P50, and P90 are 10th, 50th, and 90th percentiles respectively

Sandstones				
	P10	P50	P90	No. of points
P-impedance [kPa.s/m]	6 239	7 607	9 795	668
Vp/Vs ratio [frac.]	1.65	1.73	1.81	
Shales				
	P10	P50	P90	No. of points
P-impedance [kPa.s/m]	6 851	7 620	8 456	7 864
Vp/Vs ratio [frac.]	1.89	2.00	2.13	

Carbonates				
	P10	P50	P90	No. of points
P-impedance [kPa.s/m]	11 470	12 112	12 902	805
Vp/Vs ratio [frac.]	1.59	1.64	1.99	

The cluster analysis of the log data was used to construct the model that classifies the lithofacies based on P-impedance and Vp/Vs ratio. The frequency distributions of the samples in each cluster were used to create probability density functions (PDFs). The PDF represents the probability of facies occurring for a given combination of P-impedance and Vp/Vs ratio as shown in Figure 5-7.

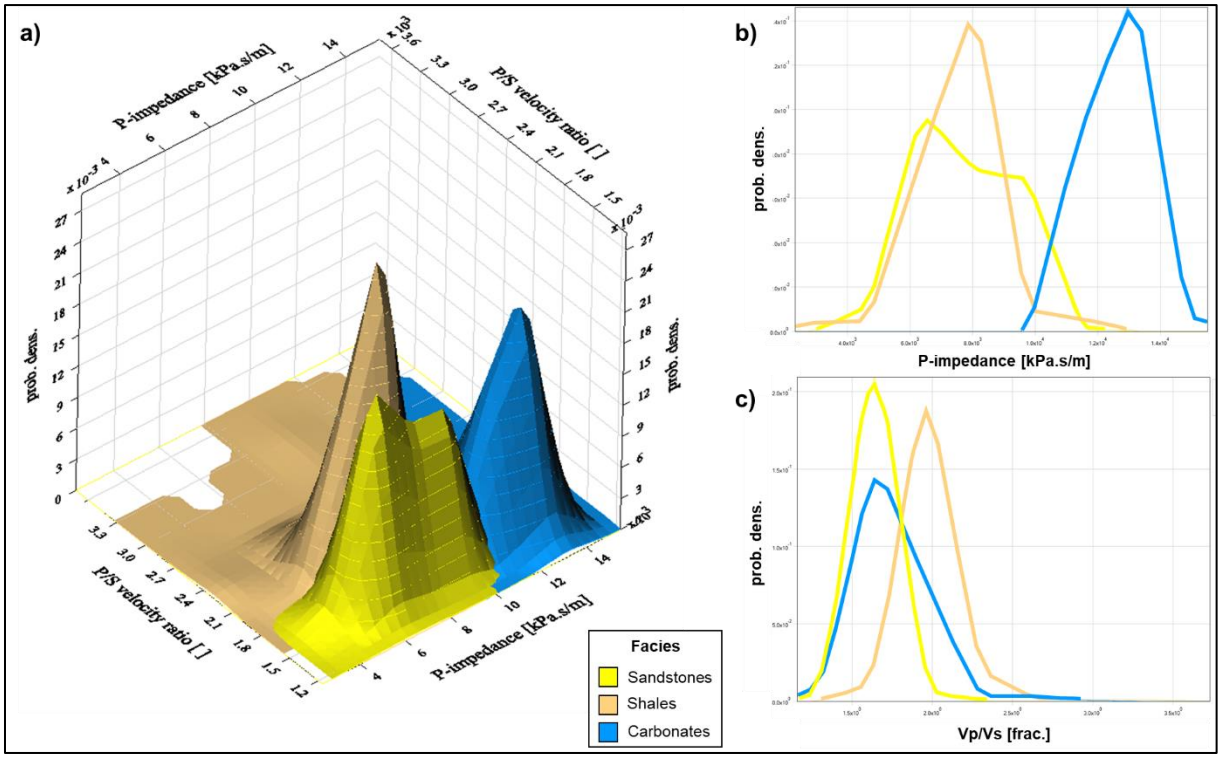

Figure 5-7. The lithofacies classification model derived from well log data. A) Probability density functions (PDFs) for each facies in P-impedance vs Vp/Vs ratio domain, b) PDFs as a function of P-impedance, severe overlapping of sandstones and shales is visible, carbonates can be identified by high impedance values, c) PDFs as a function of Vp/Vs ratio, overlapping of sandstones and shales is reduced, severe overlapping of siliciclastic and carbonates is visible

The lithofacies classification model is derived using the Bayesian classification algorithm (Schlumberger, 2019). This is a supervised learning algorithm, that divides the training data (in this case the well log data) into the specified number of clusters (in this case three lithofacies). The prior information of facies probabilities has to be specified. In the creation of the lithofacies prediction model from Figure 5-7, equal prior probabilities were assigned to each facies. Prior

probabilities are updated according to the Bayes rule, resulting in PDFs which represent the conditional probabilities. In other words, for each combination of P-impedance and Vp/Vs-ratio the probability of each facies is derived. In general, PDFs may overlap as shown in Figure 5-7b and c. In case of overlap, when applying the classification model to new data (e.g. to the results of seismic inversion), the algorithm will assign the facies with the higher conditional probability (PDF) to this set of P-impedance and Vp/Vs ratio values. Such an approach will not always result in a true classification for overlapping PDFs. Even though the algorithm assigns facies with a higher probability to a set of AI and Vp/Vs ratio values, there is still a probability that it can be the other overlapping facies (Avseth et al., 2005). To evaluate the quality of the classification algorithm, we can analyze the confusion matrices in Table 5-3. The confusion matrices can be derived using for example the bootstrapping method (Avseth et al., 2005). Using the upper part of the table, the probability of predicting a sandstone if it is truly a sandstone (according to the facies log) is 83%. However, the algorithm can also predict a shale with a probability of 13% and carbonate with a probability of 4%. Using the bottom part of the table, the probability that a sample is a shale if predicted as shale is 87%, however, if the algorithm predicts a sandstone it is possible that it is shale with a probability of 12%, or if a carbonate was predicted there is 1% of chance that it is a shale. A high-quality classification model should have confusion matrices with diagonal values close to 1.0 (Schlumberger, 2019). The classification model used in the thesis is of good quality since all diagonal values of the confusion matrix are greater than 0.8 (Table 5-3).

Table 5-3. Confusion matrices for lithofacies classification model used in the thesis

P (Prediction | True)			
Facies	Sandstone	Shale	Carbonate
Sandstone	0.83	0.13	0.03
Shale	0.13	0.84	0.01
Carbonate	0.04	0.03	0.96
P (True | Prediction)			
Facies	Sandstone	Shale	Carbonate
Sandstone	0.83	0.12	0.04
Shale	0.14	0.87	0.03
Carbonate	0.03	0.01	0.93

Applying the litho-classification model to the volumes of P-impedance and Vp/Vs ratio from the AVO inversion results in probability cubes for each facies and the most probable lithofacies classification. The probability cubes were used as a guide for the SIS algorithm in the workflow based on the deterministic AVO inversion. In the workflow based on the stochastic AVO inversion, the lithofacies classifications were directly used to obtain facies distributions.

5.4. Deterministic AVO inversion

The deterministic AVO inversion workflow consists of the following phases: extraction of a wavelet, seismic angle stacks traces alignment, low-frequency model building, seismic inversion itself, and QC of the inversion.

5.4.1. Wavelet selection

The results of the seismic inversion using different deterministic wavelet extraction methods (extended white, signal/noise, ISIS time, ISIS frequency) were obtained and checked using the QC methods described in section 5.4.4. The best results were obtained using the average wavelet calculated from the ISIS frequency wavelets extracted from all wells inside the study area, as described in Chapter 6.

5.4.2. Seismic trace alignment

The alignment of the seismic traces in the near, mid, and far angle stack was done to properly represent the AVO effect in the data. Trace alignment is a key step in data preparation, and it was performed using the non-rigid matching (NRM) algorithm. This algorithm matches the individual traces across the angle stacks by vertical stretching within a gliding time window (Schlumberger, 2015a). The near-angle stack was defined as a reference volume, to which the mid-stack was adjusted. The resultant displacement cube is automatically stored. Then the far-stack was adjusted to the mid-stack and the result adjusted to the near-stack using the displacement cube of the mid-stack adjustment. The correlation between near and mid traces and near and far traces are derived for a time window around a user-defined surface and can be used to QC the results. These correlation maps are shown in Figure 5-8. The NRM algorithm increases the correlation between the traces in the angle stacks, making them more suitable for AVO inversion.

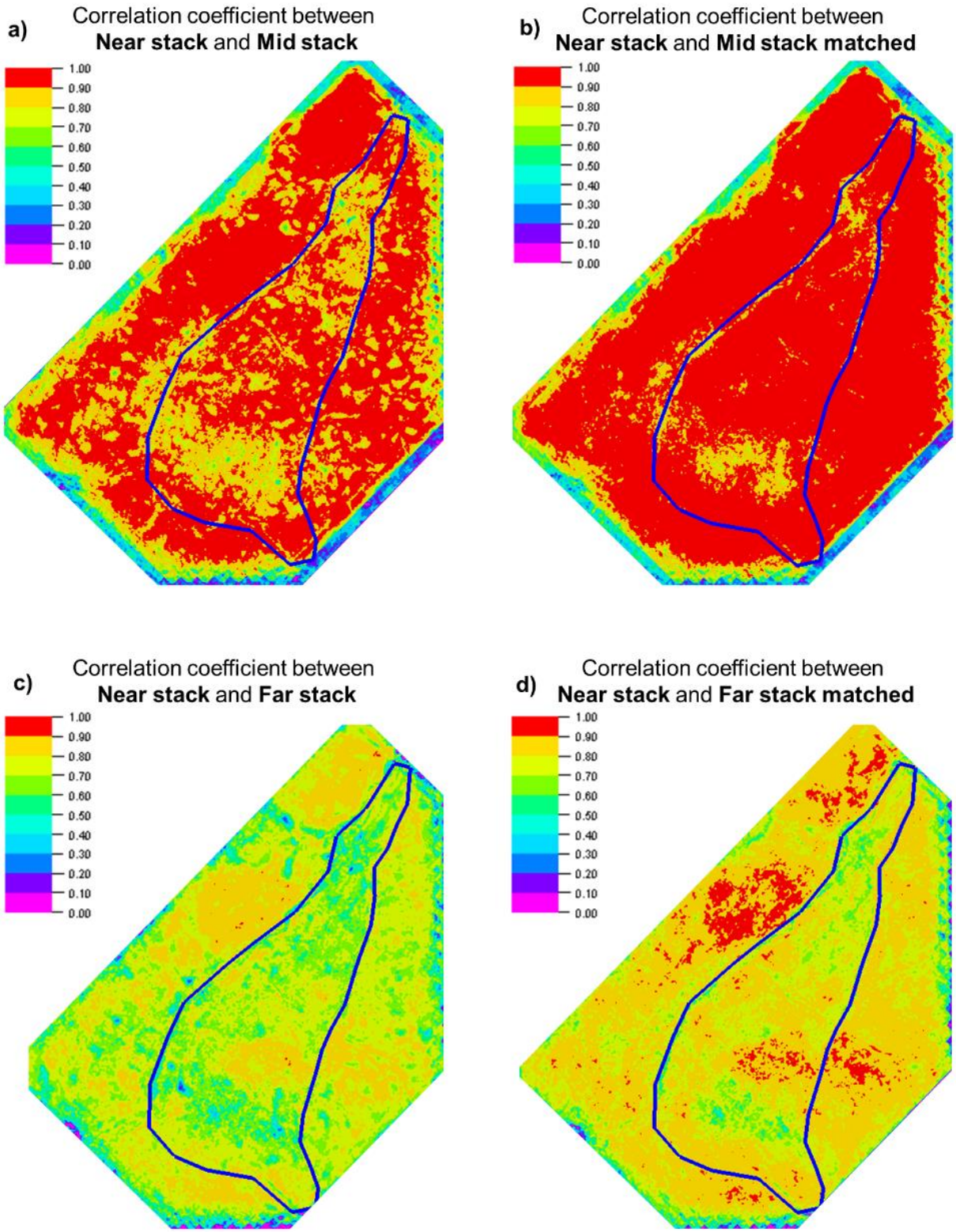

Figure 5-8. Correlation surfaces from the seismic trace alignment algorithm. The maps show the correlation coefficients between the traces before the alignment (a and c) and after the alignment (b and d). The algorithm results in higher correlation coefficients making the matched angle stacks appropriate for AVO inversion. The blue line indicates the extent of the geomodel

5.4.3. Low-frequency model (LFM) building

The low-frequency model was constructed to introduce the missing low frequencies in the seismic spectrum. Three low-frequency models were set up, one for each parameter obtained from the seismic AVO inversion: P-impedance, Vp/Vs ratio, and density. The well logs for each property were low-pass filtered to 8 Hz and interpolated between the wells using the same surfaces that were used to create the geomodel (tops Shetland, Brent, Drake, and Cook). The following wells were used: 30/9-5S, 30/9-9, 30/9-11A, 30/9-15, 30/9-J-12, 30/9-J-13, and 30/9-J-16 (Figure 5-4). A structural smoothing filter was applied to the resulting LFMs to remove minor artifacts.

5.4.4. Seismic inversion and QC

The deterministic AVO inversion is obtained by minimizing the cost function, which measures various quantities. The cost (or objective) function terms and their interpretation is given in Table 5-4. The inversion is based on finding the global minimum of the cost function. The algorithm defines how well the final model should fit the seismic data (controlled by the Signal to Noise Ratio - SNR), the degree of lateral variations (horizontal continuity parameter - Rα), and the allowed differences between the inversion result and the LFM (controlled by the tie to the LFM parameter - Rσ). Finally, it influences the number of significant reflectors above a user-defined threshold level R1 (Schlumberger, 2015a).

Table 5-4. The components of the cost function for deterministic AVO inversion and their interpretation (Schlumberger, 2015a)

Term	Interpretation
$E = f(SNR) \times \Sigma(Si - di)^2$	Penalty for not fitting the seismic
$+ f(1/R\alpha) \times \Sigma C_i (P_i - P_{i\pm1})^2$	Penalty for horizontal variation
$+ f(1/R\sigma) \times \Sigma (P_i - P_{lfm})^2$	Penalty for deviations from the low frequency mode
$+ R1$ (# significant reflectors)	Penalty for number of reflectors that exceed threshold

The AVO inversion results need to be transformed to a synthetic angle reflectivity that allow deriving synthetic angle-stacks. Theoretically this can be done using the Zoeppritz equation.

However, these equations are complex and therefore CPU-demanding. To increase performance two Zoeppritz equations approximations can be selected (Fatti and Aki&Richards). The algorithm can invert for acoustic impedance, Vp/Vs ratio, shear impedance, and density.

The results of the seismic inversion were checked using two methods: examining the inversion using logs at a well location and examining the residual seismic volume (Figure 5-9).

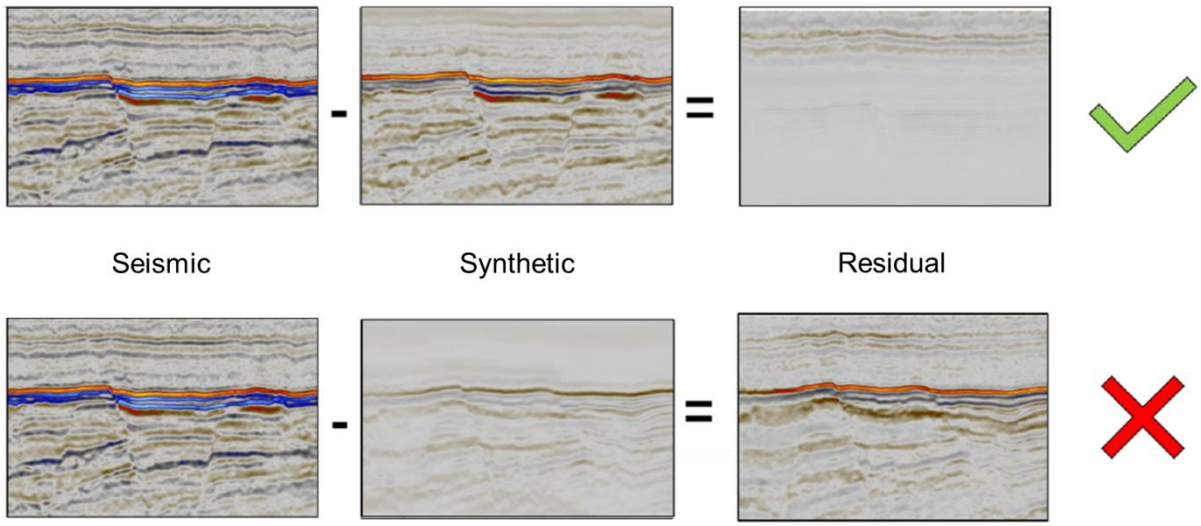

Figure 5-9. Example of quality checking of the seismic inversion result. The residual seismic is the difference between the measured seismic and the synthetic seismic from the inversion. The synthetic should be as similar as possible to the original seismic, therefore the residual values should be small. Modified from Rotar (2019)

Many trials with different inversion parameters, wavelets, inversion methods, and versions of the low-frequency models were performed on a limited volume of seismic stacks to ensure the best output of the deterministic inversion. The best results were obtained using AVO inversion based on the Aki and Richards approximation and the average of ISIS frequency wavelets extracted from all wells inside the geomodel. This is described in Chapter 6.

5.5. Stochastic AVO inversion

The stochastic AVO inversion has some steps in common with the deterministic AVO inversion. These are the seismic trace alignment, wavelet extraction, and the low-frequency model building. The stochastic AVO inversion results are stored in the cells of the geomodel. This was performed in the following steps: upscaling the well logs into the geomodel, resampling the low-frequency models into the geomodel, variogram analysis, stochastic inversion itself, and quality control.

5.5.1. Well logs upscaling and LFMs resampling

The well logs of P-impedance, Vp/Vs ratio, and density were upscaled into the geomodel cells. The stochastic simulation honors the upscaled values (it will not change them in the iterative updating of the model), which are needed for the SGS algorithm embedded into the inversion. The same low-frequency models used for the deterministic AVO inversion were resampled into the geomodel.

5.5.2. Variogram analysis

Vertical variograms are an essential part of the stochastic inversion since they control the high-frequency content of the seismic spectrum. In the stochastic AVO inversion, three variograms for each zone were specified: vertical, horizontal in major direction, and horizontal in minor direction. The vertical variograms were derived using logs of P-impedance from the wells inside the geomodel. The parameters of the experimental variogram calculation such as the number of lags, lags distance, and lag tolerance, i.e. the percentage of overlapping of neighboring lags, were tested to obtain the most representative plot. The visualization of these parameters is shown in Figure 5-10. Figure 5-11 shows an example of a vertical variogram model in the Shetland-Brent zone. A spherical variogram model with zero nugget and the range of 10 m was fitted to the experimental variogram. The nugget is a measure of the uncertainty of the data and the data are not accurately honored when the nugget is larger than zero. The variogram models the well log data which are regarded to have only small error. Therefore, throughout this thesis, the variograms are modeled with zero nugget.

The lateral variogram ranges were derived from the deterministic AVO inversion results. The P-impedance volume was resampled into the geomodel to allow a variogram analysis. The same variogram ranges, both vertical and lateral, were used in the facies simulation based on the deterministic AVO inversion workflow described in section 5.6.

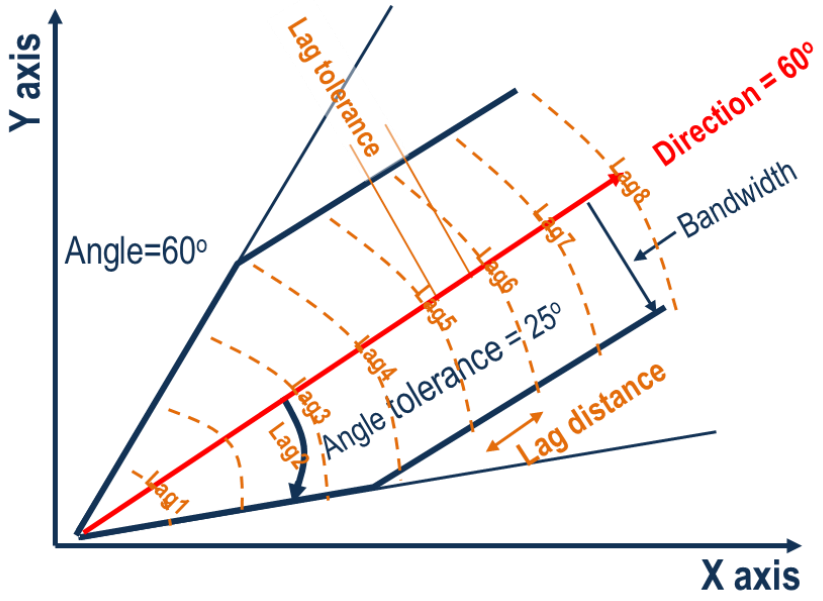

Figure 5-10. Visualization of search cone parameters for calculating the experimental variograms

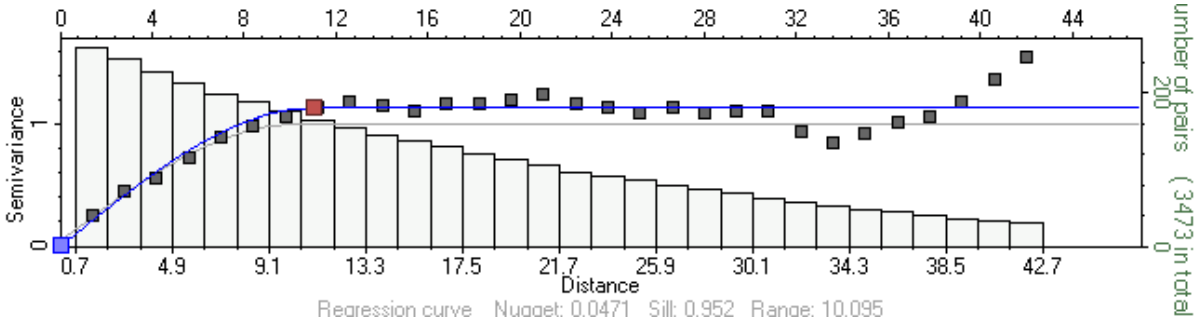

Figure 5-11. Example of vertical variogram modeling in the Shetland-Brent zone. Grey dots indicate the experimental variogram, the blue line is the spherical variogram model fitted to the experimental variogram, the histogram shows the number of pairs used to calculate the experimental variogram for each lag distance

5.5.3. Stochastic AVO inversion and QC

The stochastic AVO inversion was performed to obtain many equiprobable realizations of P-impedance, Vp/Vs ratio, and density. The input to the algorithm, as described above, are upscaled well logs for each elastic property, aligned seismic stacks, wavelets for each stack, the low-frequency model for each elastic property, and variogram models for each zone. Furthermore in each zone, the standard deviation for each elastic property and the correlation coefficients between elastic properties must be specified. They were estimated from the input upscaled well logs. The correlation matrix contains information about correlation coefficients between P-impedance, Vp/Vs ratio, and density. Usually, the elastic parameters are correlated to some degree and specifying the correlation matrix ensures that the algorithm does not change the elastic properties in a completely random way (Schlumberger, 2015b).

The cost function in the stochastic AVO inversion is defined as a correlation coefficient between observed seismic angle stacks and synthetic seismic angle stacks. The optimization stops when the value of the cost function exceeds the convergence criterion (Schlumberger, 2019). The convergence criterion was set to 0.8, meaning that a minimum of 80% of the measured seismic traces must be explained by the inversion. The maximum number of iterations perturbing the initial model was set to one hundred to limit the computation time, in case the inversion would struggle to converge to the measured seismic trace. The number of realizations needed to capture the uncertainty in the seismic inversion and facies modeling are discussed in subsection 5.6.

The methods to QC the stochastic AVO inversion include evaluating the diagnostic data output and the blind well test. The most important diagnostics are the cost function, the number of iterations and the convergence as visualized in Figure 5-12. The cost function informs about the value of the cost function after all iterations are performed. In Figure 5-12 the cost function in most nodes has a high value, above the convergence criterium, indicating a successful inversion. In these nodes, the other two diagnostics indicate a small number of iterations and positive (true) convergence. In the nodes where there is a high number of iterations and a small value of the normalized cost function (below the convergence criterium), the inversion did not converge to the seismic trace within the expected error. In the example of Figure 5-12, the areas where the inversion failed are related to fault zones and seismic anomalies induced by shallow gas (Schlumberger, 2015b).

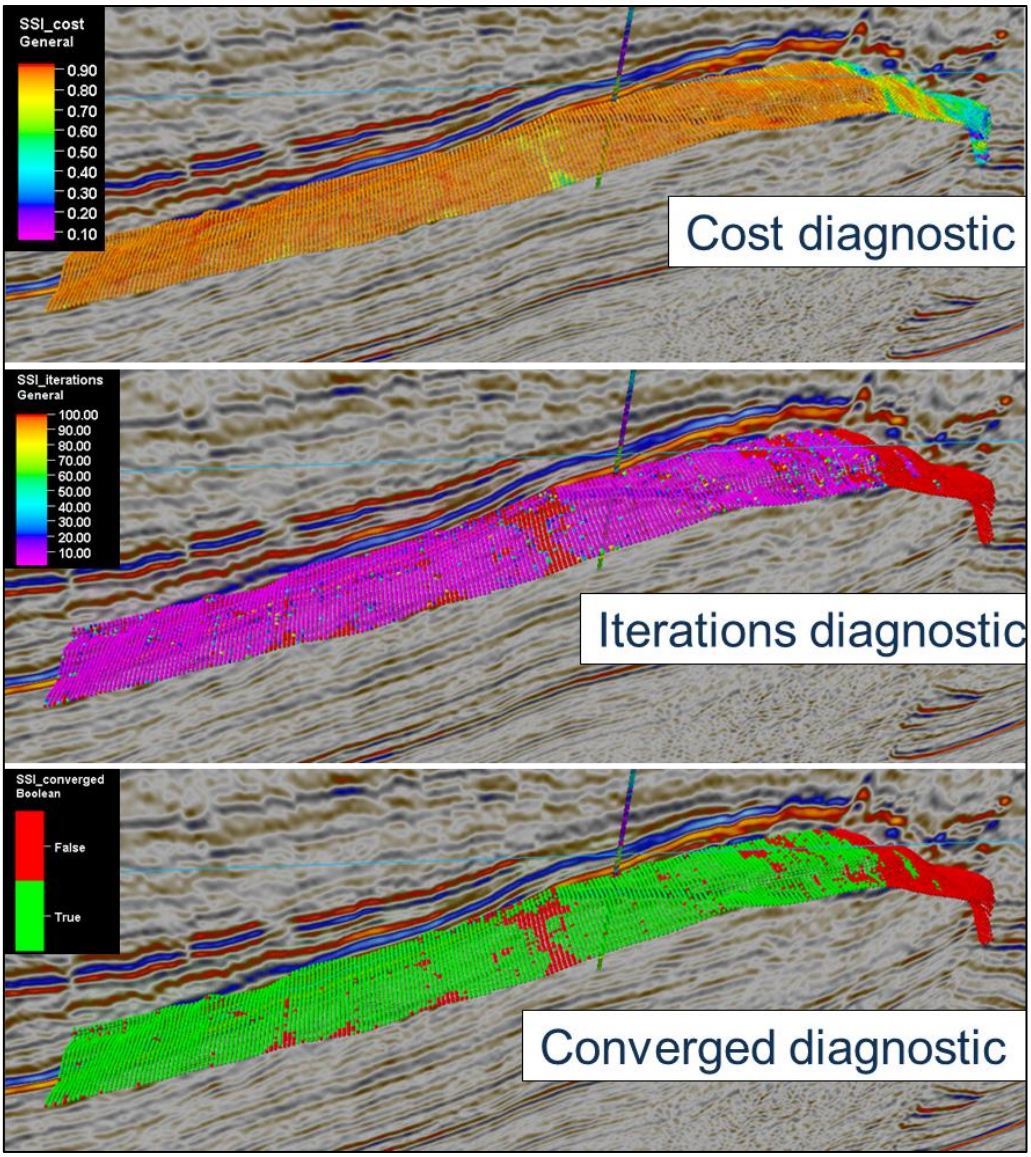

Figure 5-12. Diagnostic output from seismic stochastic inversion (Schlumberger, 2015b)

The blind well test allows to check the inversion at the well locations where logs were not upscaled and used in the inversion. In all other wells where well logs were upscaled and used in the inversion, the result of the stochastic AVO inversion will always be the same as the upscaled log.

5.6. Facies simulation and volume calculation

The litho-classification model from Figure 5-7 was applied to the 3D volumes of the P-impedance and the Vp/Vs ratio from the deterministic AVO inversion. As a result, three probability volumes for sandstone, shale, and carbonate were generated. These probabilities were sampled into the geomodel to guide the SIS algorithm. The SIS algorithm calculates the conditional probability of facies occurrence based on the upscaled and simulated cells,

variogram models, and the probability volumes from the litho-classification. Then SIS samples the conditional probability in a stochastic way (Monte Carlo sampling). This means that even if facies has a small conditional probability of occurrence, they can be simulated by the SIS algorithm.

Each realization of the stochastic AVO inversion was classified using the same litho-classification model from Figure 5-7. The litho-classification model checks for each combination of P-impedance and Vp/Vs, the PDF functions of the three facies and assigns the facies with the highest PDF value. In this sense, the litho-classification is a deterministic process, that refers directly to the elastic properties. The litho-classification was run on each realization of the stochastic AVO inversion. It is important to note that all facies models are supported by the seismic data.

The results from both the deterministic and stochastic workflows were depth-converted using the P-wave migration velocity volume from seismic processing. The facies volumes from these two methods were calculated and compared (Chapter 6).

Another concern is the number of realizations of the facies models that allow fully capturing the uncertainty embedded into the workflows, and especially in the AVO inversion. Simm and Bacon (2014) indicate that the minimum number of realizations for the stochastic inversion should be one hundred, which is the number I used in each workflow. The results are shown in Chapter 6.

6. Results

6.1. Deterministic AVO inversion

The wavelets for near, mid, and far angle stacks were extracted using the reflectivity from all wells inside the study zone (inside the geomodel) and averaged (Figure 6-1). The following wells were used: 30/9-5S, 30/9-9, 30/9-11A, 30/9-15, 30/9-J-12, 30/9-J-13, 30/9-J-16 (Figure 5-4). The deterministic extraction method using ISIS frequency wavelets with linear phase estimation was used.

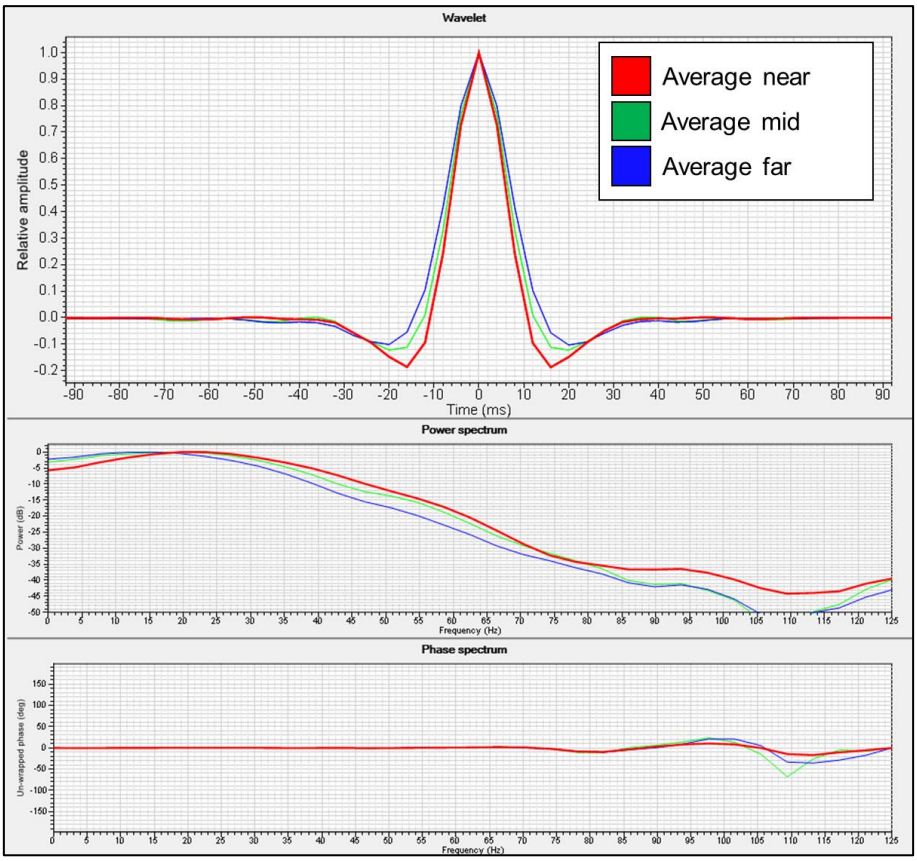

Figure 6-1. Average wavelets computed from ISIS frequency wavelets extracted from all wells inside the study area

The low-frequency models (LFMs) were derived by interpolation of the well logs low-pass filtered by 8 Hz. The interpolation was guided by the horizons top Shetland Gp., top Brent Gp., top Drake Fm., and top Cook Fm., which were also used to create the geomodel. The 3D volumes of P-impedance, Vp/Vs ratio, and density were obtained using simultaneous AVO inversion of the aligned angle stacks (see section 3.3 and 5.4 for details). The results are presented in Figures 6-2 to 6-5.

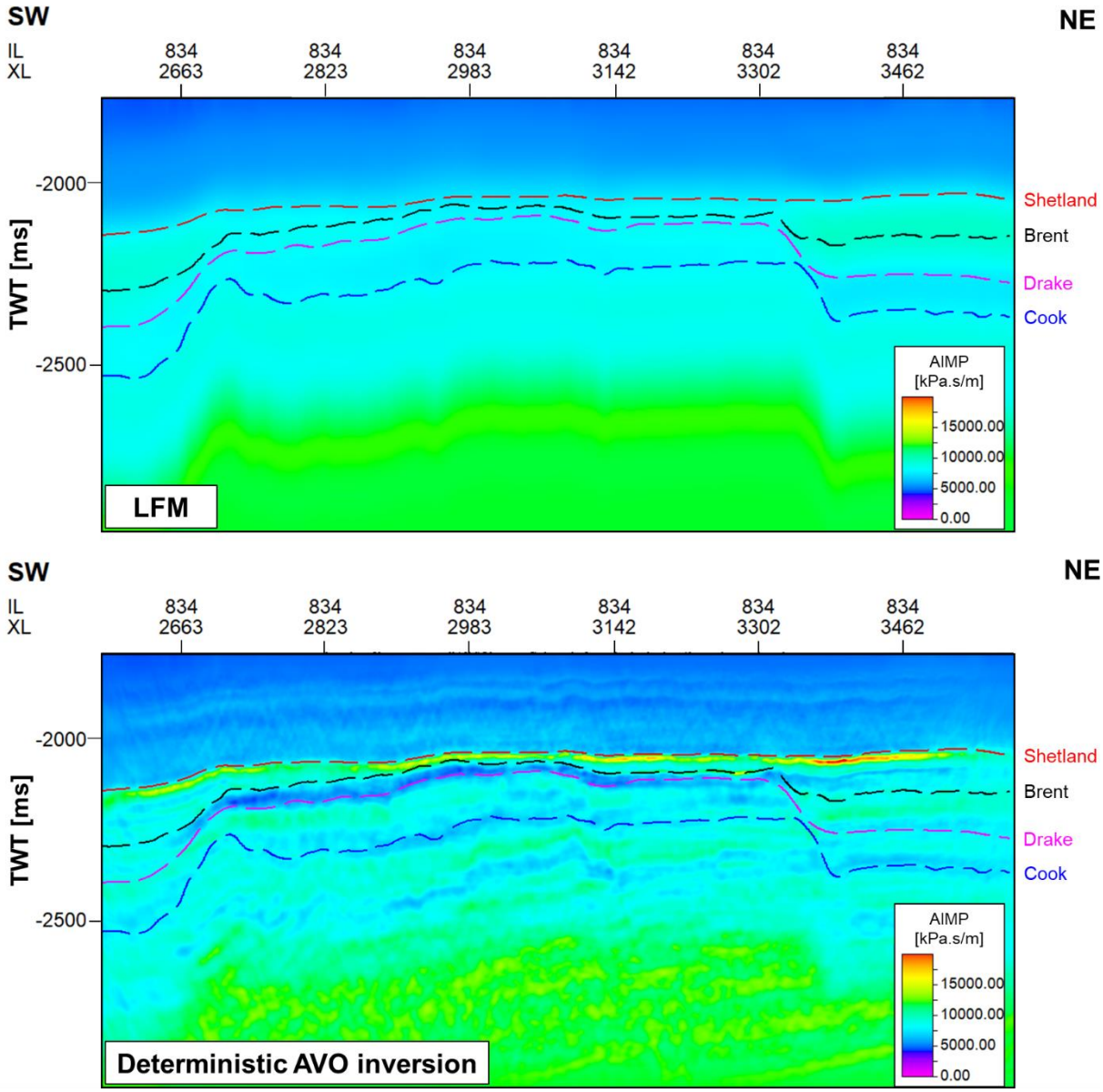

Figure 6-2. Upper picture: the low-frequency model of P-impedance, bottom picture: the P-impedance resulting from the deterministic AVO inversion. See Figure 4-2 for the location of the section.

The P-impedance section in Figure 6-2 shows strong amplitude anomalies at the top of the Shetland-Brent zone which is attributed to carbonate. The LFMs does not indicate these amplitude anomalies. The Brent-Drake zone shows very low P-impedance in comparison with the Shetland-Brent and the Drake-Cook zones. Low P-impedance values are attributed to sand and shale.

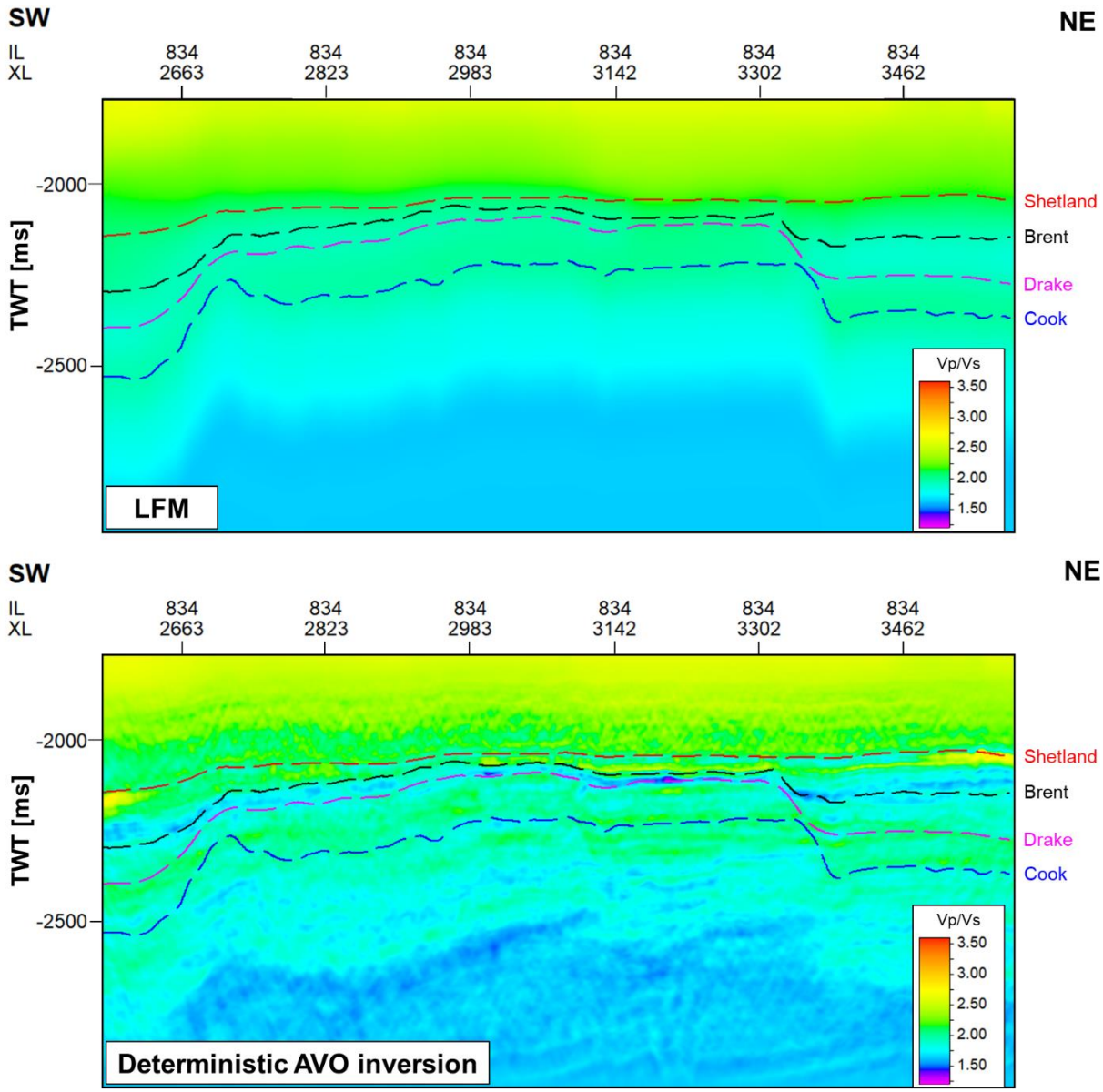

Figure 6-3. Upper picture: the low-frequency model of Vp/Vs ratio, bottom picture: the Vp/Vs ratio resulting from the deterministic AVO inversion. See Figure 4-2 for the location of the section.

The Brent-Drake zone in Figure 6-3 shows lower values of Vp/Vs ratio in comparison with the Shetland-Brent and Drake-Cook zones. Lower Vp/Vs ratio values combined with relative low P-impedance values discussed above, are attributed to higher sandstone content than in the two other zones. Higher Vp/Vs ratio values combined with relative low P-impedance such as in the Drake-Cook zone are attributed to shale.

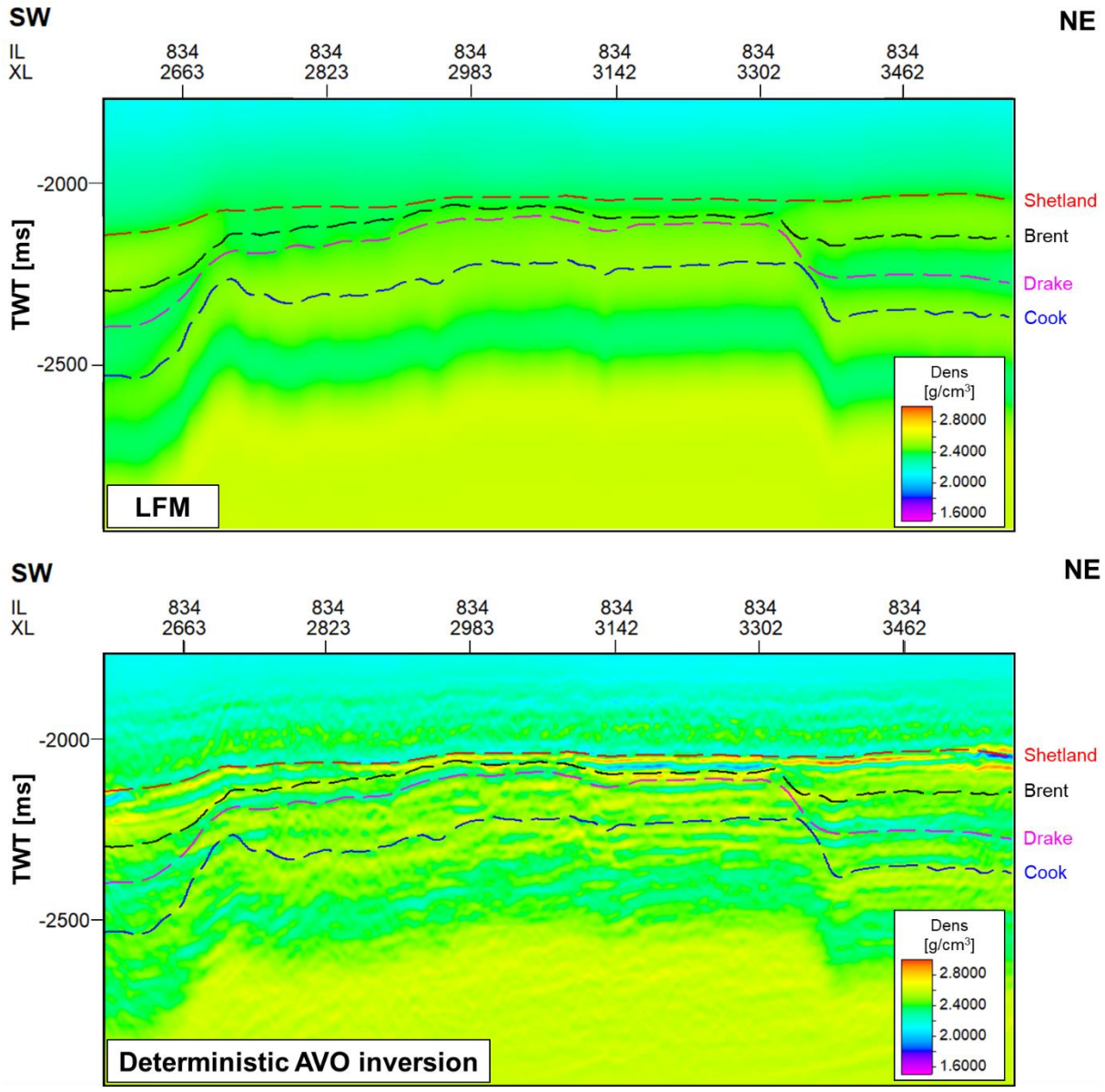

Figure 6-4. Upper picture: the low-frequency model of the density, bottom picture: the density resulting from the deterministic AVO inversion. See Figure 4-2 for the location of the section.

The Shetland-Brent zone in Figure 6-4 shows high density anomalies, which are not visible on the LFM. High density anomalies are attributed to carbonates. The Brent-Drake zone shows lower values of density which are attributed to sandstone. The Drake-Cook zone shows higher density values than the Brent-Drake zone, however they are lower than the anomalies in the Shetland-Brent zone. Consequently, they are attributed to shales.

The inversion results were quality controlled using a seismic inversion QC plot (Figure 6-5) and by investigating the synthetic and residual angle stacks (Figures 6-6 to 6-8).

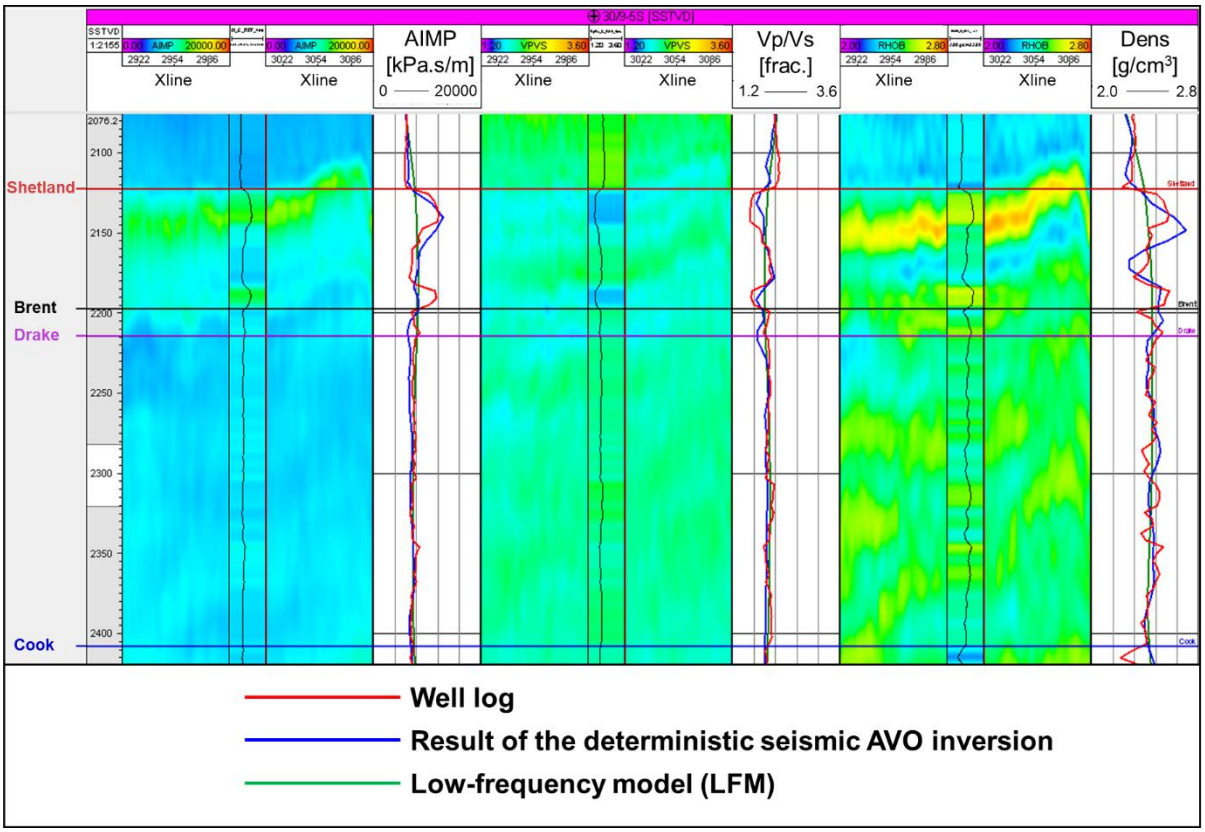

Figure 6-5. Seismic inversion QC plot for well 30/9-5S. The plot shows for each elastic property derived from the deterministic AVO inversion (P-impedance, Vp/Vs ratio, and density) an inline section with the well log trace inside and the viewport with the well log (red), the elastic parameter from the AVO inversion (blue), and the LFM (green).

Figure 6-5 shows for each parameter resulting from the deterministic AVO inversion an inline section of the elastic property with the corresponding log trace of well 30/9-5S. Next to it, a viewport with the well log (red), the result of the inversion (blue), and the LFM transformed into a log form along the wellbore (green). The seismic inversion QC plot allows checking on the inline section if the inversion results are consistent with the elastic property value from the well log. The well log tracks allow to easily compare the log data with the inversion result. The P-impedance from the deterministic AVO inversion closely mimics the well log but it is unable to reproduce the acoustic impedance anomaly in the lower part of the Shetland-Brent zone. The P-impedance in the Brent-Drake zone is slightly underestimated in the bottom part. The Vp/Vs ratio from the deterministic AVO inversion follows the shape of the Vp/Vs ratio from the well log, however, in some intervals the correlation between the inversion result and the Vp/Vs log is low. The density from the AVO inversion is the least reliable property as it does not show a good correlation with the well log in the Shetland-Brent and Brent-Drake zones. In the Drake-Cook zone, the well logs show no major anomalies in all elastic parameters and therefore no

significant changes in the seismic amplitudes. In such case, the inversion reflects mainly the low-frequency model.

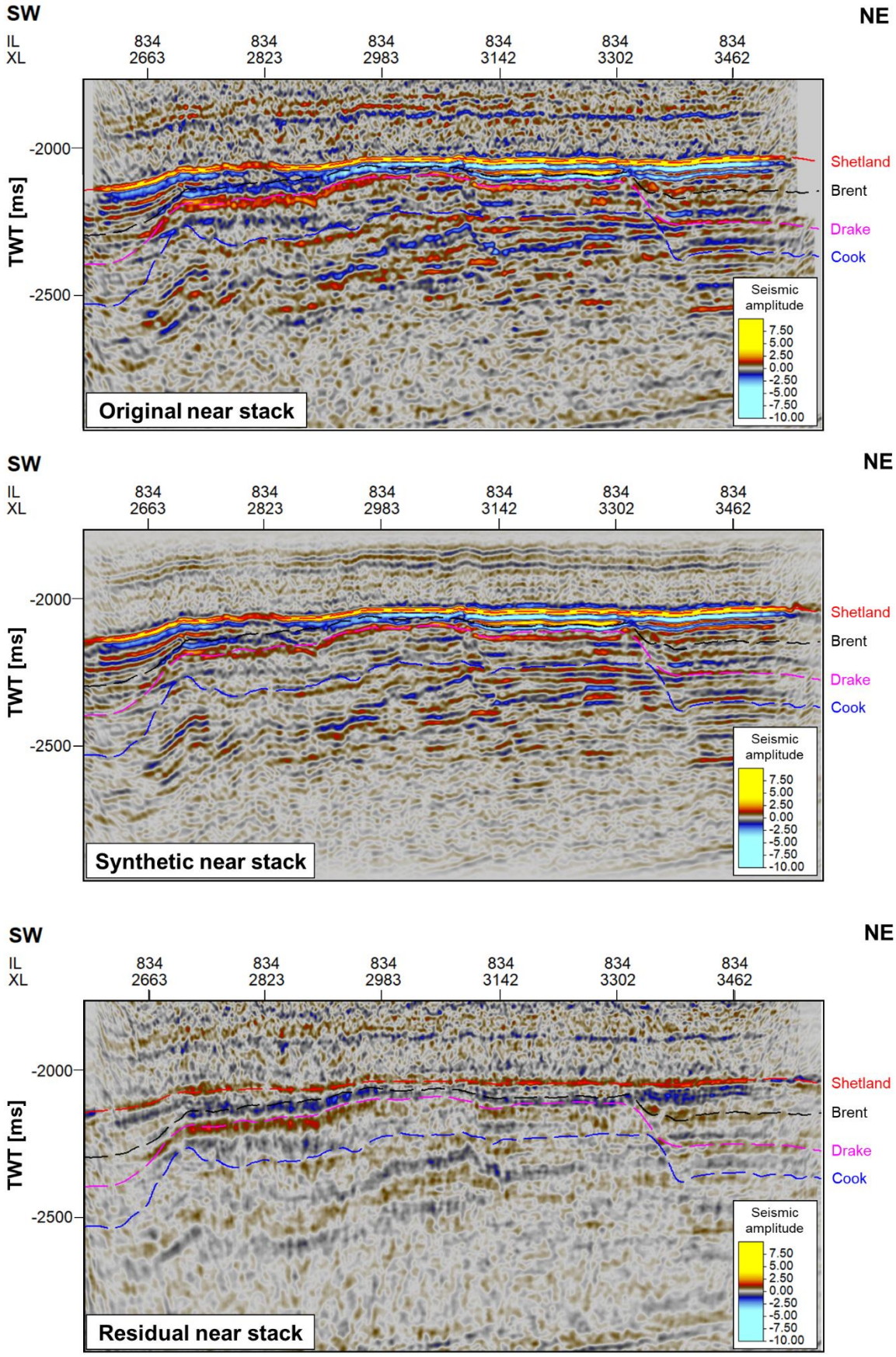

Figure 6-6. Upper picture: original near angle stack. Middle picture: synthetic near angle stack resulting from the deterministic AVO inversion. Bottom picture: residual near angle stack (the difference between original and synthetic stacks). See Figure 4-2 for the location of the section.

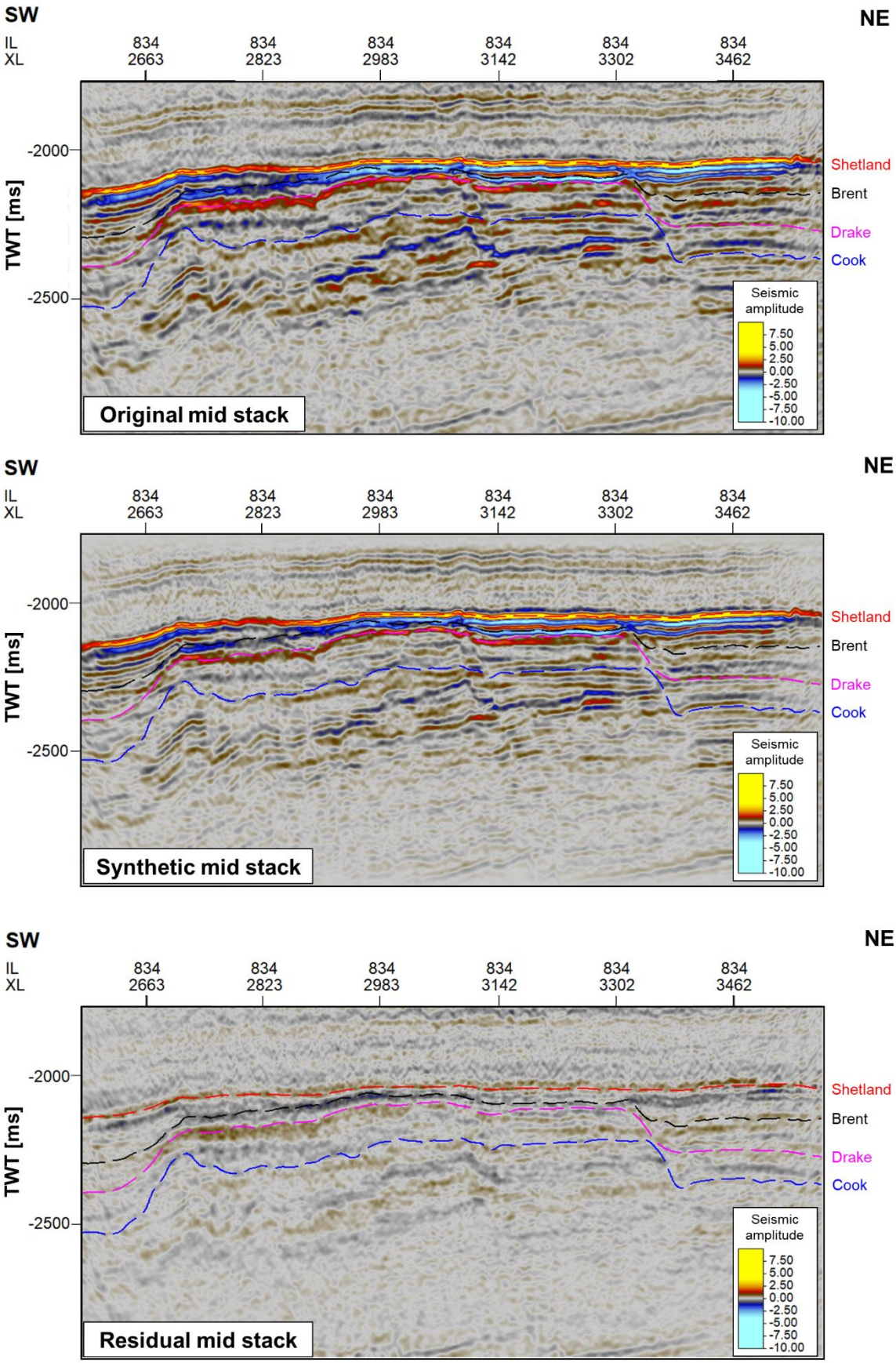

Figure 6-7. Upper picture: original mid angle stack. Middle picture: synthetic mid angle stack resulting from the deterministic AVO inversion. Bottom picture: residual mid angle stack (the difference between original and synthetic stacks). See Figure 4-2 for the location of the section.

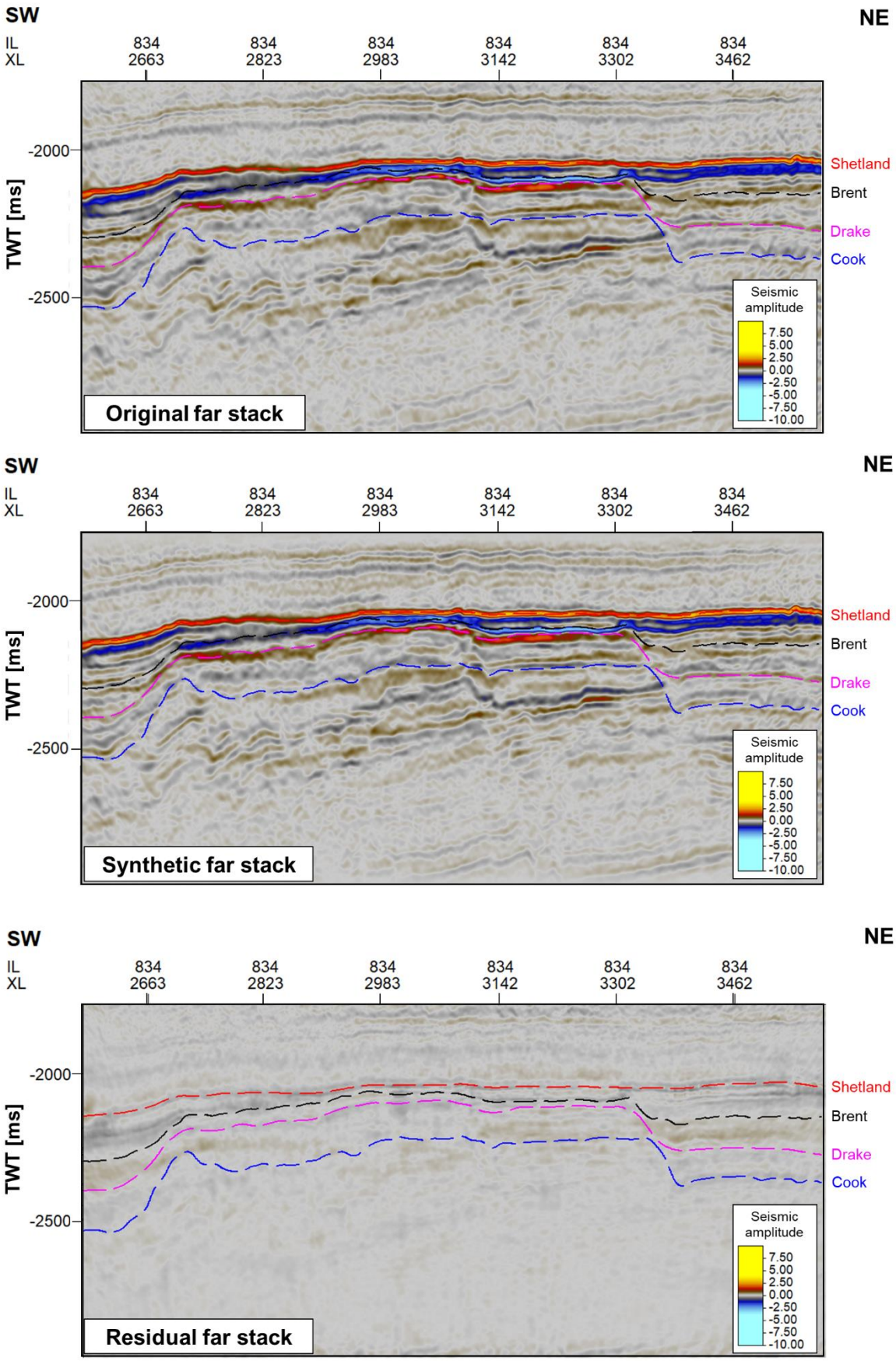

Figure 6-8. Upper picture: original far angle stack. Middle picture: synthetic far angle stack resulting from the deterministic AVO inversion. Bottom picture: residual far angle stack (the difference between original and synthetic stacks). See Figure 4-2 for the location of the section.

The synthetic angle stacks in Figures 6-6 to 6-8 deliver a good match with the original seismic. The best result was obtained for the far angle stack, as documented by the residual stack. The residuals for near and mid angle stacks show higher amplitudes, meaning that the AVO inversion was not able to fully recover the original seismic amplitudes. All residual stacks show a coherent signal, that mimics the reflectors in the original seismic. Therefore, the amplitudes of the residuals represent not only noise but also a seismic signal.

The original and synthetic stacks show a high similarity, and the P-impedance and Vp/Vs ratio cubes resulting from the deterministic AVO inversion correlate with the well logs. Therefore, these results can be regarded as sufficiently reliable for guiding the facies modeling. Due to the poor correlation between the calculated density in the vicinity of the wells and the well log density this inversion cube was not used as a facies guide.

6.2. Stochastic AVO inversion

The P-impedance cube from the deterministic AVO inversion was resampled into the geomodel to perform the horizontal variogram analysis. The vertical variogram modeling was performed on the upscaled P-impedance logs (see section 5.5.2). The results of the variogram modeling for the reservoir zone Brent-Drake are shown in Figure 6-9. The parameters of the experimental variogram were adjusted in a way that the ranges of the variogram model could be determined reliably. The spatial continuity in the Brent-Drake zone was modeled with a 10 m range vertical variogram, and a 2800 m range, laterally isotropic (the range in major direction is equal to the range in minor direction) variogram (Fig. 6-9). The same variogram models were used for the other two zones because of their good fit with the experimental variograms. All sample variograms were approximated by a spherical model with no nugget effect (blue line, Fig. 6-9). The vertical variogram range is based on the well data and is regarded as having small uncertainty. The influence of the lateral variogram range on the stochastic AVO inversion is discussed later in the thesis.

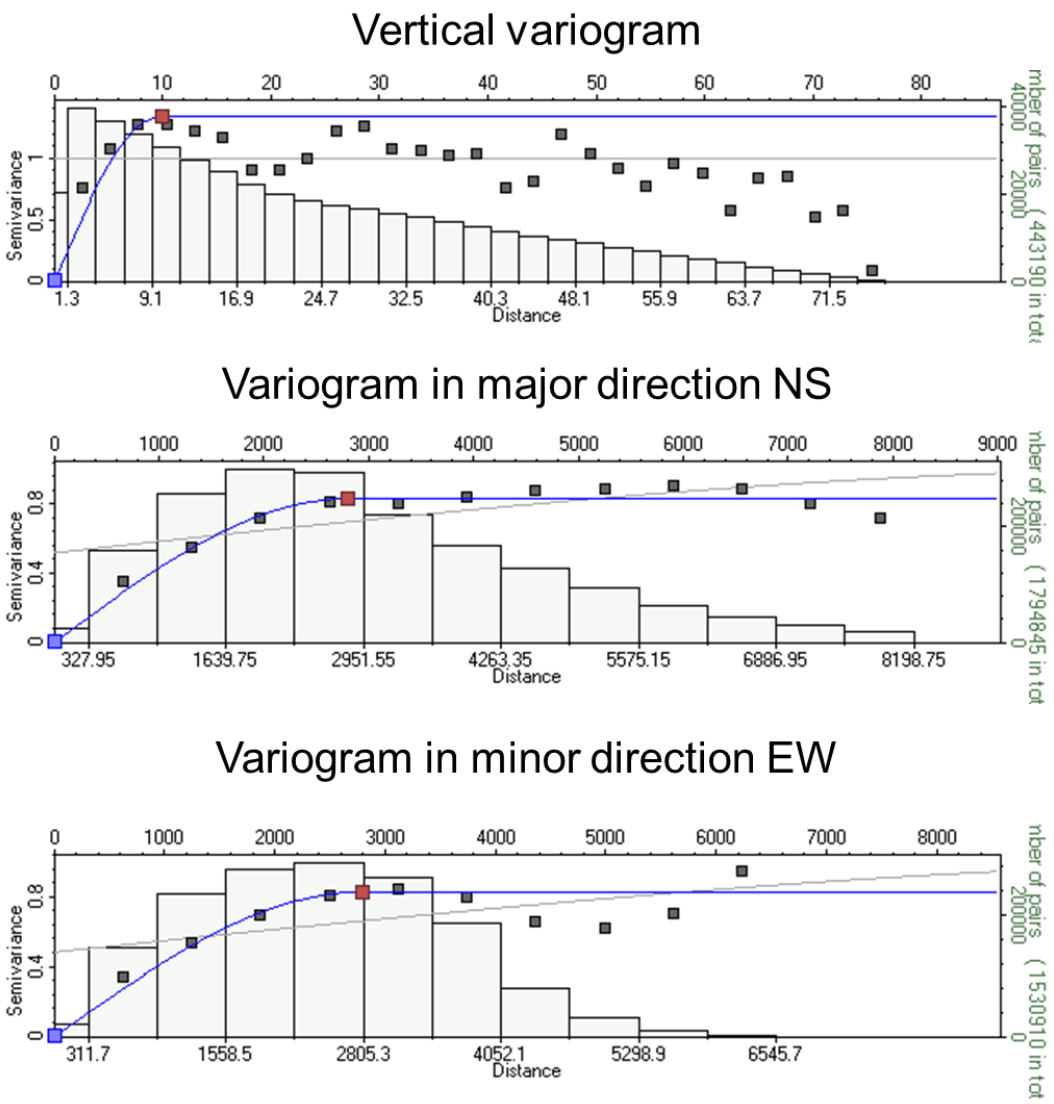

Figure 6-9. The results of the variogram analysis for the Brent-Drake zone of the geomodel. Grey dots indicate the experimental variogram, the blue line is the spherical variogram model fitted to the experimental variogram, and the histogram shows the number of pairs used to calculate the experimental variogram for each lag distance. The experimental variogram was fitted with a spherical variogram model with a vertical range of 10 m, and horizontal range of 2800 m in all lateral directions

The low-frequency models used in the deterministic AVO inversion were resampled into the geomodel cells. The stochastic AVO inversion was performed using the same LFMs, aligned seismic angle stacks, and wavelets as in the deterministic AVO inversion. The correlation matrix and the standard deviation for each elastic parameter were estimated from the upscaled well logs. The blind well test was performed on the well 30/9-J-13 (Fig. 5-4) as discussed at the end of this subsection. The results of one realization of the stochastic AVO inversion are shown in Figure 6-10. The realization is embedded into the solution of the deterministic AVO inversion presented in subsection 6.1.

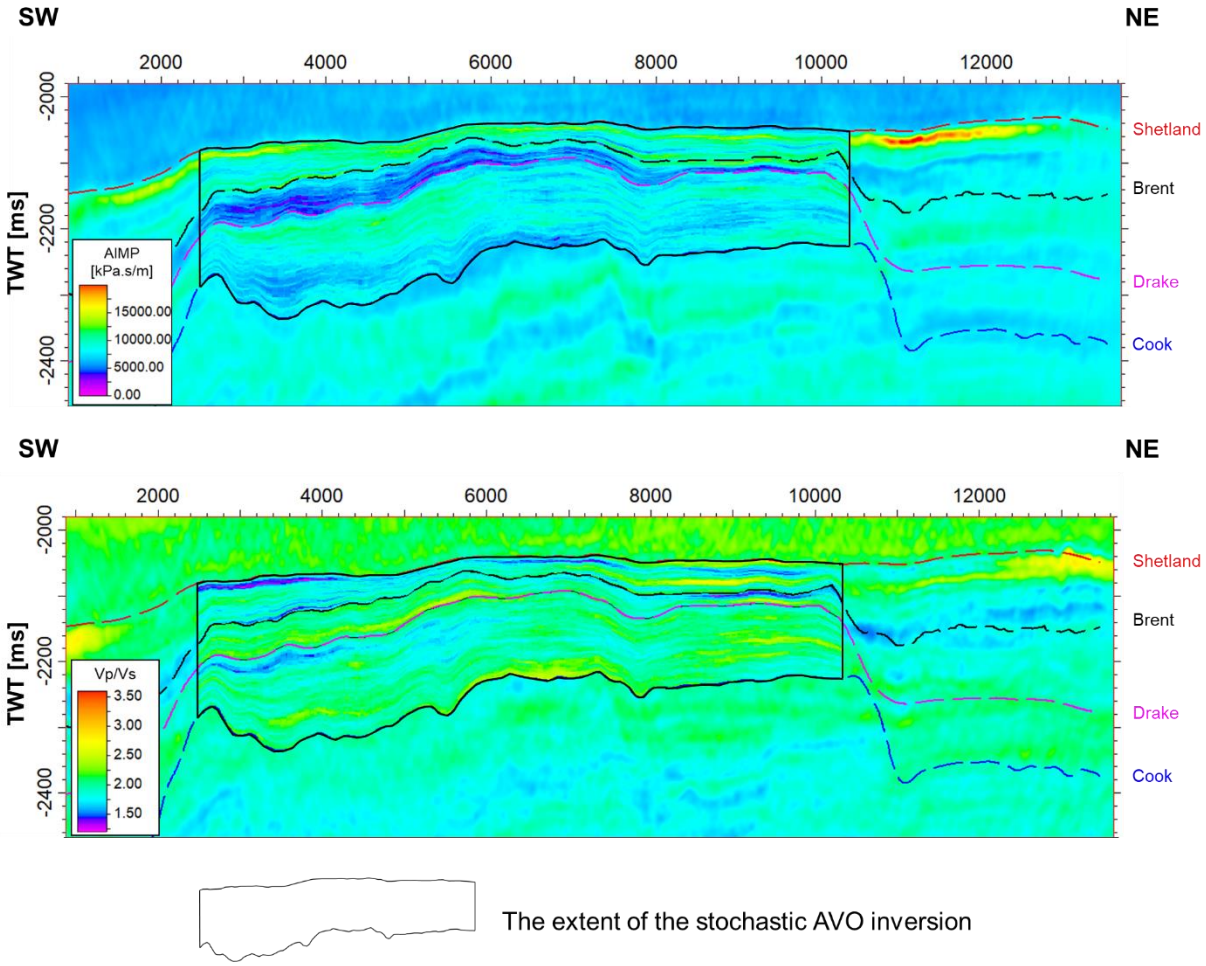

Figure 6-10. Section showing the results of one realization of the stochastic AVO inversion, embedded into the background of the deterministic AVO inversion. The extent of the stochastic AVO inversion is limited by the extent of the geomodel. The stochastic AVO inversion shows high-frequency vertical variability introduced by the vertical variogram model. See Figure 4-2 for the location of the section.

The main difference between the stochastic and the deterministic AVO inversion lies in the increased variability of the stochastic inversion, which is controlled by the variogram model. The smoother result of the deterministic AVO inversion is controlled by the bandwidth of the seismic data.

The stochastic AVO inversion results were quality checked by investigating the diagnostics of the inversion (Figure 6-11) and the blind well test (Figure 6-12).

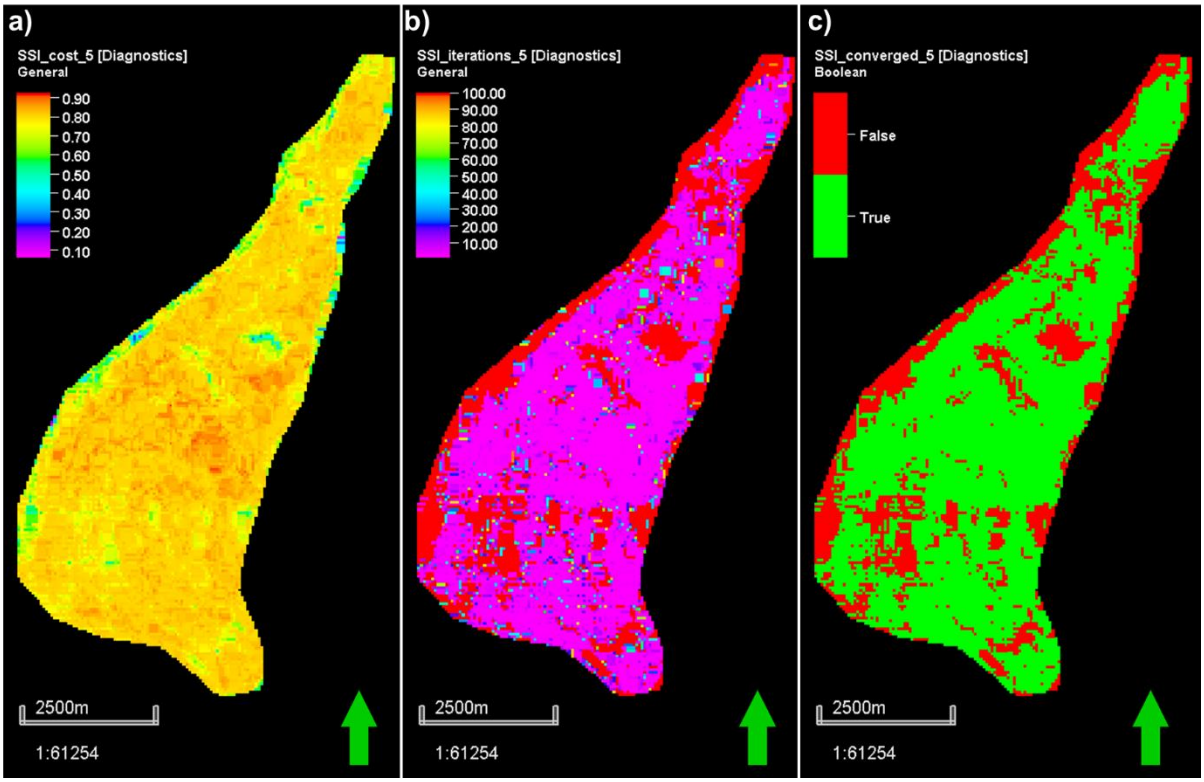

Figure 6-11. The diagnostics for one realization of the stochastic AVO inversion, a) the cost function, b) the number of iterations, c) the convergence to the seismic trace

Figure 6-11a shows that the cost function for most of the inverted traces is equal to or higher than the convergence criterion of 0.8. Consequently, for those traces, we can observe a low number of iterations (6-11b) and positive convergence to the seismic trace (6-11c). There are some zones, especially in the Northwestern part of the geomodel, where the stochastic AVO inversion failed. This is a zone of poor seismic imaging where the geomodel partially overlaps the Brage fault.

The well 30/9-J-13 (Fig. 5-4) was used to perform the blind well test and compare the results of the stochastic and the deterministic AVO inversions (Figure 6-12). As described in section 3.2, the stochastic AVO inversion should average the deterministic AVO inversion. This is best observed in the Drake-Cook zone (only the uppermost part of the zone is shown in Figure 6-12). In the Shetland-Brent and Brent-Drake zones there are differences between the deterministic AVO inversion and the average of the stochastic AVO inversion realizations. These differences may arise from the uncertainty in the variogram model or a non-ideal parametrization of the deterministic AVO inversion. Despite these differences, the average of the stochastic AVO inversion mimics the result of the deterministic AVO inversion and the upscaled well log. Ten realizations of the stochastic AVO inversion roughly show the

uncertainty ranges embedded into the seismic AVO inversion. The upscaled well log in almost every layer lies within these uncertainty ranges.

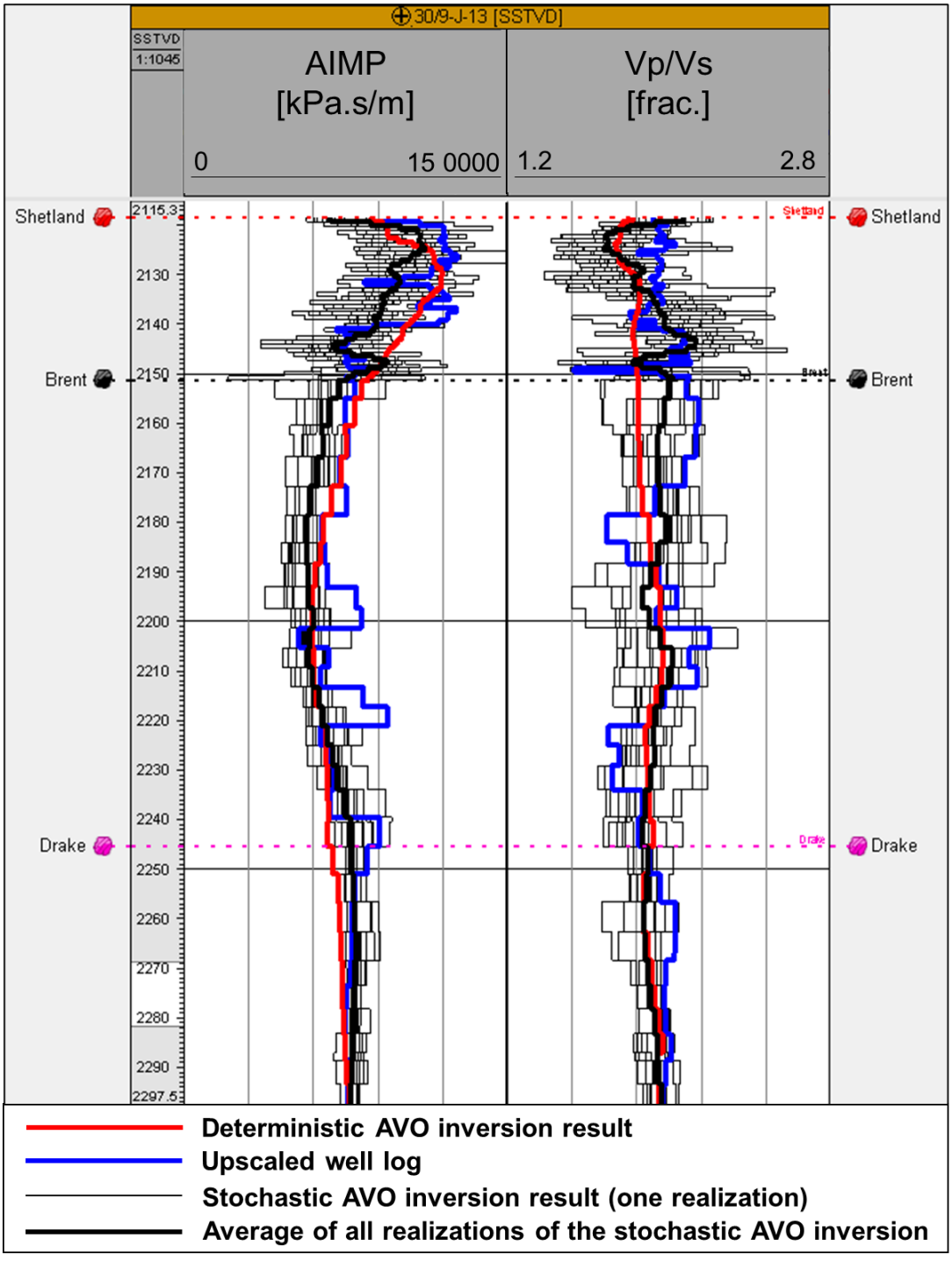

Figure 6-12. The blind well test of the stochastic AVO inversion using well 30/9-J-13 (Fig. 5-4). The thin black curves show ten realizations of the stochastic AVO inversion. The thick black curve shows the average of one hundred realizations of the stochastic AVO inversion. The deterministic AVO inversion result (red) and the upscaled well log (blue) are also plotted for comparison

After the analysis of the diagnostics maps and the blind well test, the stochastic AVO inversion was assessed as being of sufficient quality to guide the facies modeling.

6.3. Facies modeling

The results of the deterministic and the stochastic AVO inversion were used to guide the facies modeling as described in section 5.6. The results of facies modeling using these two approaches are shown in Figures 6-13 to 6-17.

The sandstone probability from the deterministic AVO inversion (Figure 6-13a) is limited to the seismic bandwidth. It shows a lower vertical variability than the sandstone probability from the stochastic AVO inversion (Figure 6-13b). In the reservoir Brent-Drake zone, the probability of sandstone resulting from the deterministic AVO inversion is high along the entire cross-section, whereas the stochastic AVO inversion shows lower sandstone continuity and thin layering. The extent of the layers is controlled by the horizontal variogram range. In Figure 6-13c, there is much more sandstone in the Brent-Drake zone from the deterministic AVO inversion than from the stochastic AVO inversion (Figure 6-13d). In the bottom part of the Drake-Cook zone, the probability of sandstone from the deterministic AVO inversion (6-13a) is low but not zero. Therefore, the SIS algorithm simulates some sandstone there (6-13c). The probability of sandstone from the stochastic AVO inversion in some parts of the Drake-Cook zone has quite high values even approaching 0.5 (6-13b), but there is almost no sandstone predicted in that zone by this realization (6-13d). The facies distribution is different in each realization as shown in Figure 6-14.

Figure 6-14 presents the comparison of facies predicted by the two workflows in the blind well 30/9-J-13 (Fig. 5-4). The sandstone probability from the deterministic AVO inversion shows a smooth character reflecting the limitation of seismic resolution. The sandstone probability from the stochastic AVO inversion shows high-frequency variability resulting from the vertical sample variogram derived from the well logs. Different realizations of the stochastic AVO inversion give different sandstone probabilities which result in different facies distributions.

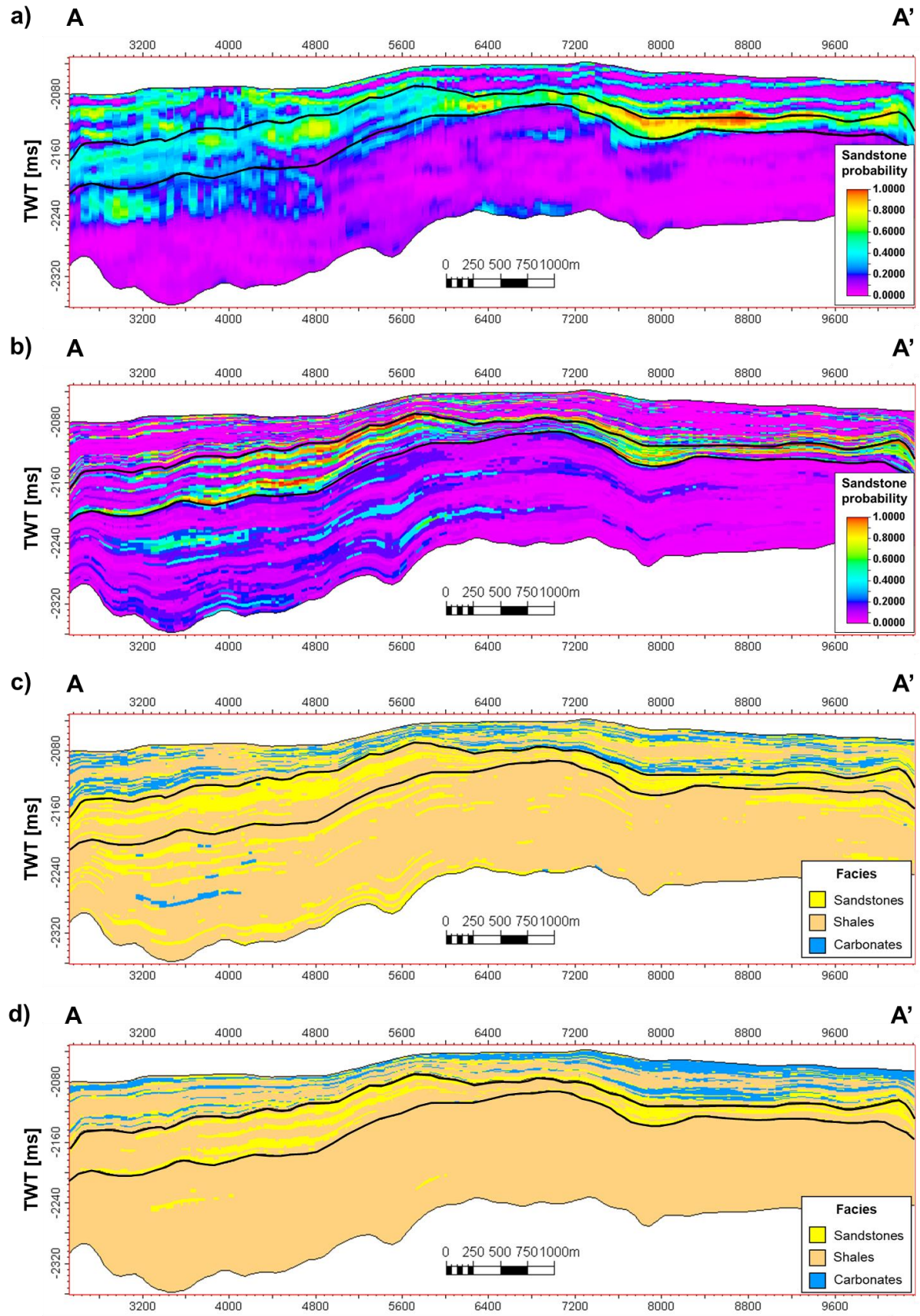

Figure 6-13. The cross-sections through the geomodel showing a) sandstone probability from the deterministic AVO inversion, b) sandstone probability from the stochastic AVO inversion (one realization), c) facies model guided by the deterministic AVO inversion (one realization), d) facies model guided by the stochastic AVO inversion (one realization). The reservoir Brent-Drake zone is highlighted by the thick black horizons. See Figure 6-15 for the location of the cross-section.

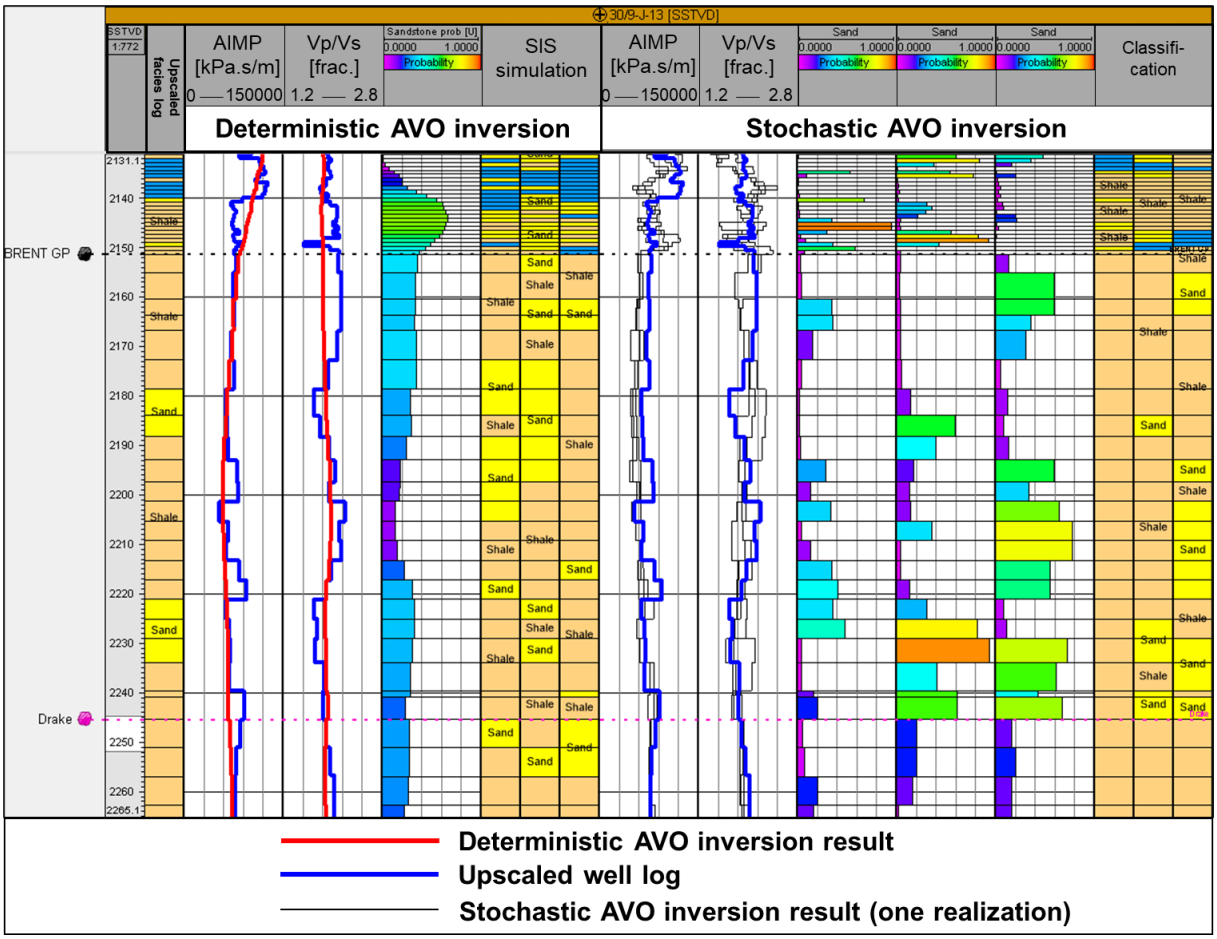

Figure 6-14. A comparison between the facies models predicted by the two inversion workflows in the blind well 30-9-J-13 (Fig. 5-4). Three facies models are compared along with the sandstone probabilities and the elastic parameters from the deterministic and the stochastic AVO inversions.

Figure 6-15 shows the map view of the top of the Brent-Drake zone in the geomodel. The results were obtained using a lateral variogram range of 2800 m, based on the analysis of the P-impedance volume from the deterministic AVO inversion. The same lateral variogram range was incorporated into the SIS simulation and the stochastic AVO inversion. However, the spatial distribution of the facies is different between the two methods (Fig. 6-15c and d). The SIS simulation guided by the deterministic AVO inversion results in a more irregular facies distribution. However, as mentioned earlier, the range of the lateral variogram is uncertain. The lateral variogram for the stochastic AVO inversion can be adjusted in a way, that the facies distribution mimics the deterministic AVO inversion (Figure 6-16). The facies model in Figure 6-16b was guided by the stochastic AVO inversion with a lateral variogram range of 600 m.

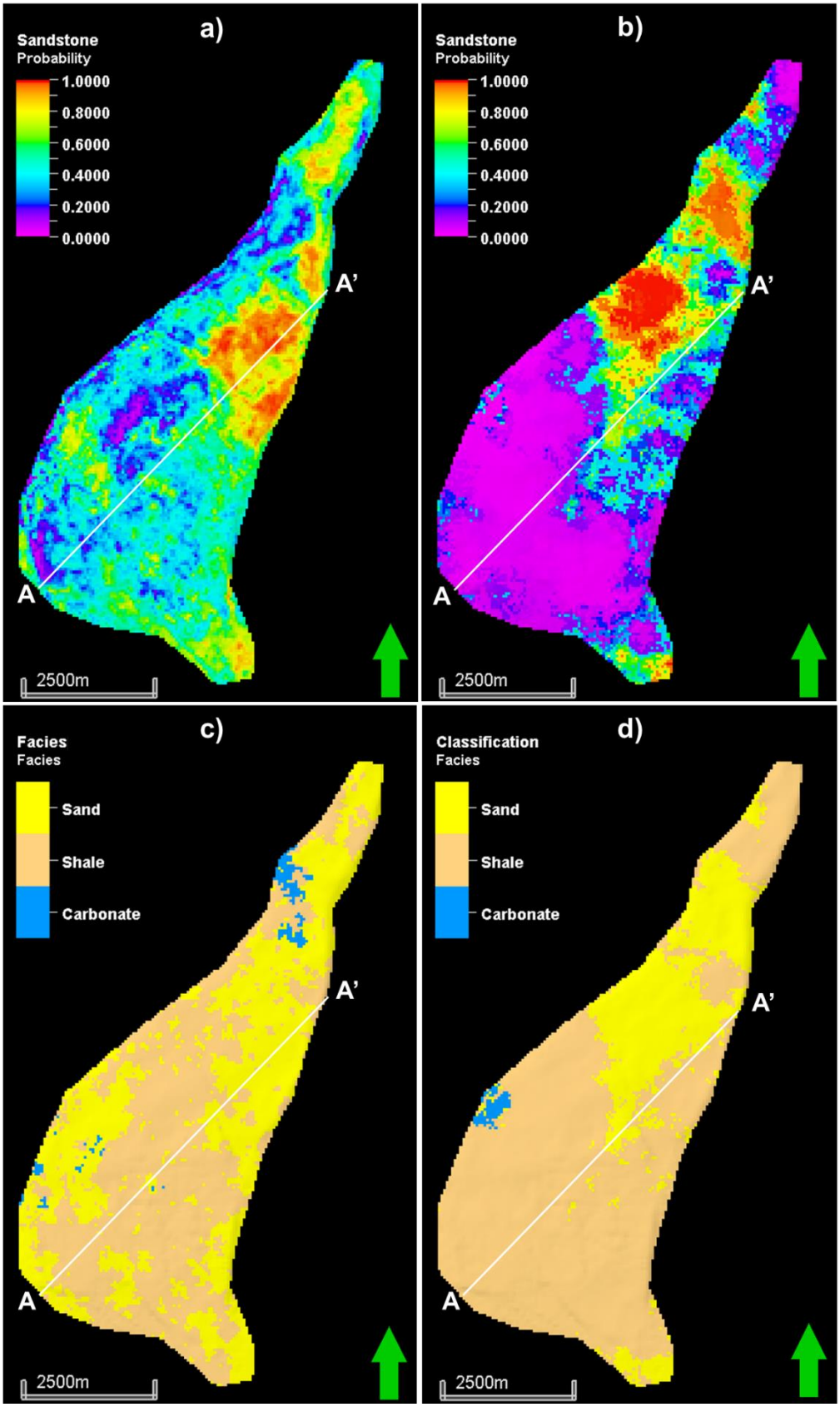

Figure 6-15. The map view of the top of the Brent-Drake zone in the geomodel. a) The sandstone probability from the deterministic AVO inversion, b) the sandstone probability from the stochastic AVO inversion (one realization), c) the facies model guided by the deterministic AVO inversion (one realization of SIS with a horizontal variogram range of 2800 m), d) the facies model guided by the stochastic AVO inversion with the same horizontal variogram range of 2800 m (one realization)

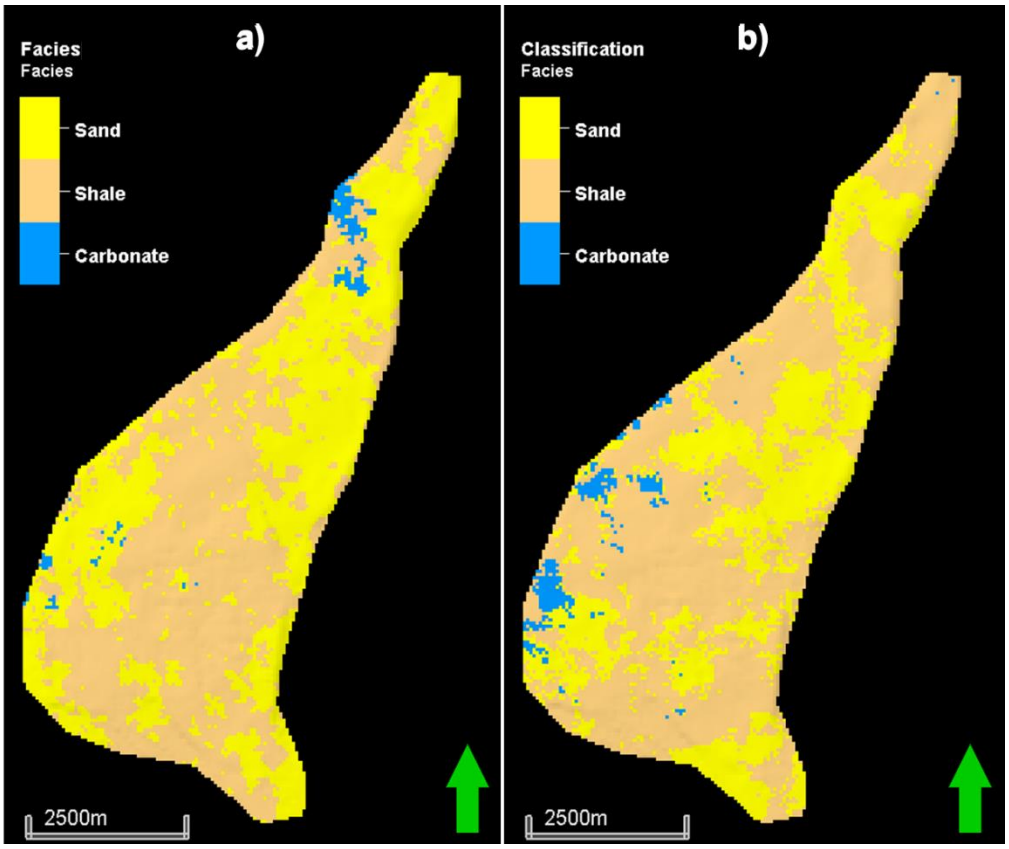

Figure 6-16. The map view of the top of the Brent-Drake zone in the geomodel. a) the facies model guided by the deterministic AVO inversion (one realization of SIS with a horizontal variogram range of 2800 m), b) the facies model guided by the stochastic AVO inversion with a lower horizontal variogram range of 600 m (one realization).

One hundred facies models were generated for the following four workflows: the deterministic AVO inversion followed by SIS with a lateral variogram range of 2800 m and 600 m, the stochastic AVO inversion with a lateral variogram range of 2800 m and 600 m, followed by the litho-classification. The sandstone volume in the Brent-Drake zone obtained from these workflows is shown in Figure 6-17. The P10, P50, and P90 volumes of sandstone, shale and carbonate are given in Table 6-1.

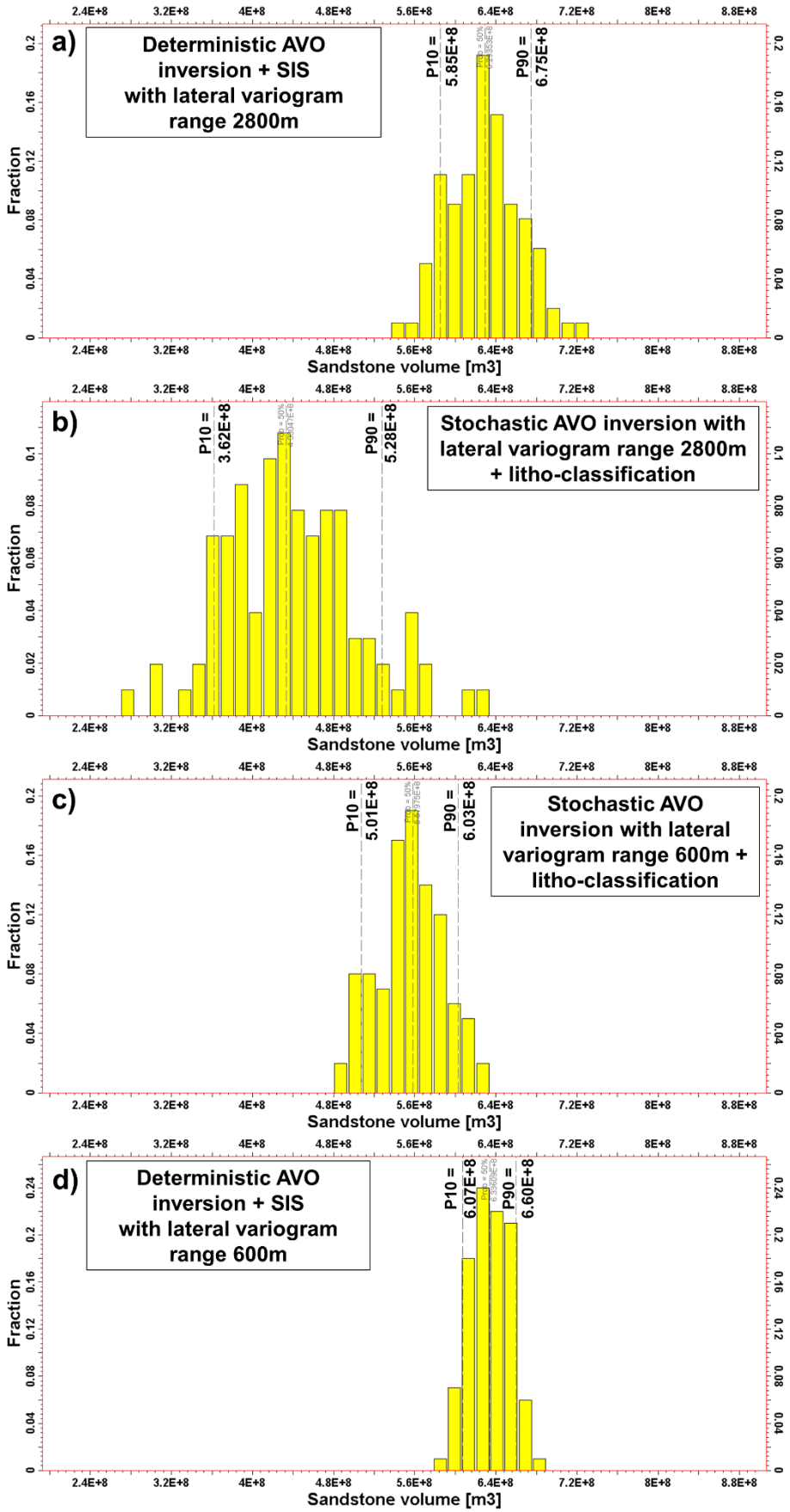

Figure 6-17. Sandstone volume in the Brent-Drake zone obtained from one hundred facies models guided by the deterministic (a and d) and stochastic (b and c) AVO inversions, with two different lateral variogram ranges of 2800 m and 600 m.

Table 6-1. Comparison of facies volumes in the Brent-Drake zone from the workflows shown in Fig. 6-17

Sandstone volume [$m^3 * 10^8$]			
	P10	P50	P90
Deterministic AVO inversion + SIS with lateral variogram range 2800m	5.85	6.29	6.75
Stochastic AVO inversion with lateral variogram range 2800m + litho-classification	3.62	4,33	5.28
Stochastic AVO inversion with lateral variogram range 600m + litho-classification	5.01	5.58	6.03
Deterministic AVO inversion + SIS with lateral variogram range 600m	6.07	6.33	6.60
Shale volume [$m^3 * 10^8$]			
	P10	P50	P90
Deterministic AVO inversion + SIS with lateral variogram range 2800m	15.40	15.65	15.75
Stochastic AVO inversion with lateral variogram range 2800m + litho-classification	15.73	15.75	15.77
Stochastic AVO inversion with lateral variogram range 600m + litho-classification	15.67	15.70	15.71
Deterministic AVO inversion + SIS with lateral variogram range 600m	15.63	15.71	15.76
Carbonate volume [$m^3 * 10^8$]			
	P10	P50	P90
Deterministic AVO inversion + SIS with lateral variogram range 2800m	6.03	6.44	6.88
Stochastic AVO inversion with lateral variogram range 2800m + litho-classification	3.64	4.37	5.30
Stochastic AVO inversion with lateral variogram range 600m + litho-classification	5.17	5.66	6.15
Deterministic AVO inversion + SIS with lateral variogram range 600m	6.15	6.42	6.71

7. Discussion

The blind well test in Figure 6-12 shows that the stochastic AVO inversion allows capturing to a large extent the uncertainty of the elastic parameters estimation. These parameters approximately average to the result of the deterministic AVO inversion. In this sense, the stochastic AVO inversion is superior to the deterministic AVO inversion as it allows obtaining additional information from the same input seismic data. However it needs a variogram model which is an additional uncertain input in comparison with the deterministic AVO inversion. The vertical variogram model is obtained from the well logs and is regarded as having a small uncertainty, but the lateral variogram range cannot be obtained reliably from a few wells that are usually available, and consequently is subject to a large uncertainty.

The sandstone probabilities are controlled by the Vp/Vs ratio and therefore they inherit the properties of the inversion methods. The sandstone probability from the deterministic AVO inversion has a smooth character as results of the limited seismic bandwidth (Fig. 6-13a, 6-14), while the sandstone probabilities from the stochastic AVO inversion show high-frequency variability (Fig. 6-13b, 6-14) as result of the vertical variogram model supported by the well logs. The two workflows utilize the sandstone probability in different ways. The deterministic AVO inversion workflow uses the stochastic SIS simulation for soft conditioning of the reservoir model (Chapter 1). Even if the sandstone probability is low (e.g. in Fig. 6-13a), the SIS will still simulate sandstone (Fig. 6-13c) in a number of realizations proportional to the sandstone probability since it uses a Monte Carlo (stochastic) sampling of the CDF of the facies fractions. The stochastic AVO inversion workflow on the other hand, incorporates the stochastic part of the facies modeling into the inversion itself and the litho-classification is a deterministic procedure. For an individual stochastic inversion the sandstone probability must be dominant over the other facies to classify the cell of the geomodel as a sandstone. Therefore, the litho-classification results in less noisy facies distribution as it discriminates low facies probabilities (Fig. 6-13 – 6-15).

Figure 6-14 shows that none of the two methods predict the existence of the two sandstone layers inside the Brent-Drake zone that are below seismic resolution. Thus, the methods have no predictive power for facies layers below seismic resolution, yet they can be used for estimating the uncertainty in volumetric calculations.

As shown in Figures 6-15d and 6-16b, the lateral variogram range has a large influence on the facies distributions from the stochastic AVO inversion. The large lateral variogram range (2800 m, Fig. 6-15d) is based on the analysis of the deterministic AVO inversion of the bandlimited seismic. Therefore, this variogram range might be too large because of the limited lateral seismic resolution. The small lateral variogram range (600 m, Fig. 6-16b) is visually guided by the deterministic AVO inversion followed by the SIS, which is a common approach to condition the facies distribution. However, this small lateral variogram range is not supported by the variogram analysis. Probably, the true lateral variogram range lies within the values defined by these two cases.

The workflow based on the stochastic AVO inversion results in much less sandstone and carbonate (Fig. 6-17b, Tab. 6-1) in the reservoir Brent-Drake zone than the workflow based on the deterministic AVO inversion (Fig. 6-17a, Tab. 6-1). However, the stochastic AVO inversion workflow with a small lateral variogram range of 600 m (Fig. 6-17c, Tab. 6-1) shifts the sandstone and carbonate volume towards the results of the deterministic AVO inversion workflow. A lower lateral variogram range introduces a larger variability in the sandstone probability which delivers a similar effect to SIS. Consequently, the lateral variogram range is of critical importance for facies modeling using stochastic AVO inversion (Fig. 6-17b-c), though it has a small impact on the P50 volume obtained from the deterministic AVO inversion (Fig. 6-17a and d, Tab. 6-1). The sandstone volume from the stochastic AVO inversion has a broader spread than the volume from the deterministic AVO inversion. A decrease of the variogram range decreases the spread of the volume distribution for both types of inversions and facies modeling (Fig. 6-17c-d as opposed to a-b). These results are somewhat surprising, and perhaps negatively surprising for the validity of the stochastic AVO inversion, which is heavily dependent on an often uncertain lateral variogram range.

8. Conclusions

Facies modeling using the stochastic AVO inversion obviously needs more workload, is more CPU-demanding and it needs the results of the deterministic AVO inversion to approximate the lateral variogram range. The AVO stochastic inversion captures the uncertainty in the elastic parameters controlling the facies probabilities. The deterministic AVO inversion results in facies probabilities that are uncertain because of the non-uniqueness of the inverse problem and are smooth due to the limited seismic bandwidth, though it requires less work and is faster. Both inversion methods have no predictive power for thin layers below seismic resolution.

The stochastic AVO inversion followed by the litho-classification can lead to substantial differences in the estimated sandstone volume in comparison with the deterministic AVO inversion followed by SIS. The variogram model largely impacts the facies distributions from the stochastic AVO inversion. The vertical variogram model is obtained from the well logs and its uncertainty is small. The lateral variogram range is highly uncertain as usually there are not enough wells in the study area to perform a reliable variogram analysis. A lower lateral variogram range in the stochastic AVO inversion shifts the sandstone volume towards the results of the deterministic AVO inversion. Consequently, the lateral variogram range is of critical importance for facies modeling using the stochastic AVO inversion, though it has a small impact on the P50 volume obtained from the deterministic AVO inversion. The sandstone volume from the stochastic AVO inversion has a broader spread than the volume from the deterministic AVO inversion. A decrease of the variogram range decreases the spread of the volume distribution for both types of facies modeling. Since both workflows can be parametrized (or adjusted) to deliver similar results by changing a highly uncertain parameter, the value of the stochastic AVO inversion for facies modeling is not yet fully understood and requires further research.

The question which method leads to more realistic facies volumes spread is open. The stochastic AVO inversion gives a broader range of volume uncertainty and all volumes are supported by seismic, therefore could be regarded as more realistic. However, the volume spread from the stochastic inversion depends on the variogram range which is uncertain. Consequently the reliability of the volume spread, depends on the reliability of the horizontal variogram range.

Due to the large influence of the lateral variogram range on the facies models from the stochastic AVO inversion the reservoir conditioning using stochastic AVO inversion is probably more suited for mature oil and gas fields, where the lateral variogram range might be obtained directly from a large number of wells.

9. Recommendations for future work

The stochastic AVO inversion can lead to substantial differences in the estimated sandstone volume, yet its value for facies modeling remains open. It is advisable to continue research on the best methods for utilizing the multiple facies probabilities from the stochastic AVO inversion. One possible alternative could be to incorporate the facies probabilities from each realization of the stochastic AVO inversion into the sequential indicator simulation.

Because the lateral variogram range has a large impact on the facies distributions from the stochastic AVO inversion and this value is often highly uncertain, it is advisable to examine the reliability of the lateral variogram range obtained from the deterministic AVO inversion. Such investigation could be possible on a synthetic reservoir model populated with known elastic properties.

10. References

Aki, K., Richards, P.G., 1980. Quantitative seismology: theory and methods, A Series of books in geology. W. H. Freeman, San Francisco.

Avseth, P., Mukerji, T., Mavko, G., 2005. Quantitative Seismic Interpretation: Applying Rock Physics Tools to Reduce Interpretation Risk. Cambridge University Press, New York, UNITED STATES.

Azevedo, L., Nunes, R., Soares, A., Neto, G.S., Martins, T.S., 2018. Geostatistical seismic Amplitude-versus-angle inversion. Geophysical Prospecting 66, 116–131. https://doi.org/10.1111/1365-2478.12589

Bjorlykke, K., 2010. Petroleum Geoscience. Springer Berlin Heidelberg, Berlin, Heidelberg. https://doi.org/10.1007/978-3-642-02332-3

Buland, A., 2019. Seismic Amplitude Analysis and Inversion Compendium Version for GEO670-H19.

Buland, A., Omre, H., 2003. Bayesian linearized AVO inversion. GEOPHYSICS 68, 185–198. https://doi.org/10.1190/1.1543206

Doyen, P., 2007. Seismic reservoir characterization an Earth modelling perspective. EAGE publications, Houten, The Netherlands.

Dubrule, O., Society of Exploration Geophysicists, European Association of Geoscientists and Engineers (Eds.), 2003. Geostatistics for seismic data integration in earth models: 2003 Distinguished Instructor Short Course, Distinguished instructor series. Presented at the Distinguished Instructor Short Course, Society of Exploration Geophysicists, Tulsa, OK.

Ellis, D.V., Singer, J.M. (Eds.), 2007. Well Logging for Earth Scientists. Springer Netherlands, Dordrecht. https://doi.org/10.1007/978-1-4020-4602-5

Færseth, R.B., 1996. Interaction of Permo-Triassic and Jurassic extensional fault-blocks during the development of the northern North Sea. Journal of the Geological Society 153, 931–944. https://doi.org/10.1144/gsjgs.153.6.0931

Faerseth, R.B., Ravnås, R., 1998. Evolution of the Oseberg fault-block in context of the northern North Sea structural framework. Marine and Petroleum Geology 15, 467–490. https://doi.org/10.1016/S0264-8172(97)00046-9

Francis, A.M., 2006a. Understanding stochastic inversion: part 1. FB 24. https://doi.org/10.3997/1365-2397.2006026

Francis, A.M., 2006b. Understanding stochastic inversion: part 2. FB 24. https://doi.org/10.3997/1365-2397.2006028

Frette, L., 2018. Quantitative seismic interpretation using converted PS waves: A case study from the Oseberg South Field, North Sea. (Master thesis). The University of Stavanger.

Husmo, T., Hamar, G.P., Hoiland, O., Johannessen, E.P., Romuld, A., Spencer, A.M., Titterton, R., 2002. Lower and Middle Jurassic, in: The Millennium Atlas: Petroleum Geology of the Central and Northern North Sea. London.

Jarzyna, J., Bała, M., Zorski, T., 1999. [in polish] Metody geofizyki otworowej pomiary i interpretacja. Wydawnictwa, AGH, Kraków.

Johnsen, J.R., Rutledal, H., Nilsen, D.E., 1995. Jurassic reservoirs; field examples from the Oseberg and Troll fields: Horda Platform area, in: Norwegian Petroleum Society Special Publications. Elsevier, pp. 199–234. https://doi.org/10.1016/S0928-8937(06)80043-3

Jones, I.F., 2018. Velocities Imaging and Waveform Inversion - The Evolution of Characterizing the Earth's Subsurface. European Association of Geoscientists & Engineers (EAGE), Houten, The Netherlands.

Lervik, K.-S., n.d. Triassic lithostratigraphy of the Northern North Sea Basin. NORWEGIAN JOURNAL OF GEOLOGY 24.

Løseth, T.M., Ryseth, A.E., Young, M., 2009. Sedimentology and sequence stratigraphy of the middle Jurassic Tarbert Formation, Oseberg South area (northern North Sea). Basin Research 21, 597–619. https://doi.org/10.1111/j.1365-2117.2009.00421.x

NPD [WWW Document], 2020a. URL https://factpages.npd.no/en/strat/pageview/litho/groups/61 (accessed 4.1.20).

NPD [WWW Document], 2020b. URL https://factpages.npd.no/en/field/pageview/all/43645 (accessed 4.1.20).

NPD [WWW Document], 2020c. URL https://factpages.npd.no/en/strat/pageview/litho/groups/16 (accessed 4.1.20).

NPD [WWW Document], 2020d. URL https://factpages.npd.no/en/strat/pageview/litho/groups/143 (accessed 4.1.20).

Ravnås, R., Bondevik, K., 1997. Architecture and controls on Bathonian-Kimmeridgian shallow-marine synrift wedges of the Oseberg-Brage area, northern North Sea. Basin Research 9, 197–226. https://doi.org/10.1046/j.1365-2117.1997.00041.x

Rider, M.H., 2006. The geological interpretation of well logs, 2. ed., rev. reprinted. ed. Rider-French Consulting, Sutherland.

Ringrose, P., Bentley, M., 2015. Reservoir Model Design. Springer Netherlands, Dordrecht. https://doi.org/10.1007/978-94-007-5497-3

Rotar, V., 2019. Reservoir Modeling and Uncertainty Estimation: A Comparison Between Stochastic and Deterministic Inversion. (Master thesis). The University of Stavanger.

Russell, B., 2016. Stochastic vs Deterministic Pre-stack Inversion Methods.

Sams, M., Millar, I., Satriawan, W., Saussus, D., Bhattacharyya, S., 2011. Integration of geology and geophysics through geostatistical inversion: a case study. FB 29. https://doi.org/10.3997/1365-2397.2011023

Schlumberger, 2019. Petrel user assistance.

Schlumberger, 2016. Petrel 2016 Property Modeling Module 9: Sequential indicator simulation.

Schlumberger, 2015a. Petrel 2014 Quantitative Interpretation Module 4: Simultaneous Inversion.

Schlumberger, 2015b. Petrel 2014 Quantitative Interpretation Module 5: Stochastic inversion.

Serra, O., 1984. Fundamentals of well-log interpretation, Developments in petroleum science. Elsevier ; Elf Aquitaine, Amsterdam ; New York : Pau.

Shuey, R.T., 1985. A simplification of the Zoeppritz equations. GEOPHYSICS 50, 609–614. https://doi.org/10.1190/1.1441936

Simm, R., Bacon, M., 2014. Seismic amplitude: an interpreter's handbook. Cambridge University Press, Cambridge ; New York.

Tayyaba, K., 2018. Simultaneous AVO inversion and seismic lithology cube estimation by using PP and PS angle stack seismic data of the Oseberg Field, North Sea. (Master thesis). The University of Stavanger.